EX LIBRIS
UNIVERSITATIS
ALBERTENSIS

The Bruce Peel
Special Collections
Library

Digitized by the Internet Archive
in 2025 with funding from
University of Alberta Library

https://archive.org/details/0162017738046

University of Alberta

Library Release Form

Name of Author: Serguei Roupassov

Title of Thesis: Modeling of Laser Produced Plasmas Guiding in Curved Magnetic Field Ducts

Degree: Master of Science

Year This Degree Granted: 2003

Permission is hereby granted to the University of Alberta Library to reproduce single copies of this thesis and to lend or sell such copies for private, scholarly, or scientific research purposes only.

The author reserves all other publications and other rights in association with the copyright in the thesis, and except as hereinbefore provided, neither the thesis nor any substantial portion thereof may be printed or otherwise reproduced in any material form whatever without the author's prior written permission.

University of Alberta

Modeling of Laser Produced Plasmas Guiding in Curved Magnetic Field Ducts

by

Serguei Roupassov

A thesis submitted to the Faculty of Graduate Studies and Research in partial fulfillment of the requirements for the degree of Master of Science

Department of Electrical and Computer Engineering

Edmonton, Alberta

Fall 2003

University of Alberta

Faculty of Graduate Studies and Research

The undersigned certify that they have read, and recommend to the Faculty of Graduate Studies and Research for acceptance, a thesis entitled 'Modeling of Laser Produced Plasmas Guiding in Curved Magnetic Field Ducts' submitted by Serguei Roupassov in partial fulfillment of the requirement for the degree of Master of Science.

Abstract

Deposition of thin films using laser plasmas is a standard technique for depositing a variety of specialty materials. One of the complications is the inclusion of debris particles from the source material. The application of a curved magnetic field to guide the plasma while stopping the debris particles, which are not guided by the magnetic field, is currently under investigation.

A 3D one-fluid magnetohydrodynamic ADI code has been developed to characterize interaction of streaming plasma with curved magnetic fields. The results of the modeling suggest that $E \times B$ drifts arising from the charge separation caused by curvature drifts can lead to poor plasma guiding.

In an attempt to address experimentally observed increase in guiding efficiency at higher magnetic fields, an alternative particle drift model with self-consistent fields has been developed. Cross-field resistive currents, capable of shorting the charge separation, are introduced and characterized as a potential mechanism responsible for plasma guiding. Dependence of guiding efficiency on plasma parameters has been characterized.

Acknowledgements

I am grateful to my supervisors, Dr. Roberts Fedosejevs, Dr, Ying Tsui, Dr. Robert Rankin, and Dr. Clarence Capjack for their for their guidance and support during the course of this thesis. I was given a unique opportunity to work on a project that was interesting both from industrial and scientific perspectives. I would like to express my special gratitude to Dr. Robert Rankin for providing me with a Cartesian version of the ADI code.

I would like to extent my thanks to Dr. Andrei Smolyakov and Dr. Valery Bychenkov for valuable discussions and expertise in the field of theoretical plasma physics.

My friends and colleagues from the Laser Plasma Interaction Group made the time I spent at the University of Alberta both pleasant and productive. I am highly thankful for that to Alexei Brodnikovski, Geoff Redman, Matt Reid, Sean Kirkwood, James Gospodyn, Blair Harwood, Hideki Minami, and Michael Buhr.

I am also thankful to my former colleagues and friends from JDS Uniphase, and especially to Dr. Evgueni Ponomarev, Dmitri Lapanik, Dr. Dan Grobnic and Dr. Graham Ian Duck who provided me with a valuable example of scientific excellence and expertise.

Completion of this thesis would not be possible without the psychological support and understanding that I received from my wife, Cristina, and my parents, Tatiana and Alexander. I am especially grateful for that.

I acknowledge the University of Alberta for the financial support I received during the program.

Contents

1. Introduction **1**

1.1 Motivation 1

1.2 Physical Mechanisms of Plasma Guiding 6

1.2.1 Charged Particle Perspective 6

1.2.2 Fluid Approach: Magnetohydrodynamics 9

1.3 Overview of Plasma Guiding Modeling 14

1.4 Scope of Present Work and Thesis Structure 20

2. Single-Fluid Magnetohydrodynamics **21**

2.1 Single-Fluid MHD Model 21

2.2 Numerical technique: ADI 28

2.2.1 Curvilinear Coordinates 28

2.2.2 Time Discretization 29

2.2.3 Spatial Discretization 31

2.2.4 Newton-Raphson linearization 33

2.2.5 Boundary Conditions 37

2.2.6 Low density plasma background 39

2.2.7 Numerical diffusion 41

2.3 Results and Discussion 44

2.3.1 Initial Conditions and Run Parameters 44

2.3.2 Numerical Results 47

3. Charged particle in self-consistent fields **59**

3.1 Plasma cross-field dielectric constant 59

3.2 Cross B-field electric current 65

4. Conclusions **77**

Appendix: MHD equations in component form **80**

Bibliography **85**

List of Figures

Figure 1. *Glow-discharge sputtering deposition schematics.* 2

Figure 2. *Schematics of Ion Beam Sputtering deposition technique.* 2

Figure 3. *Schematics of Pulsed Laser Deposition technique.* 3

Figure 4. *Schematics of PLD with curved solenoid used to guide the plasma.* 4

Figure 5. *Microphotograph of a) DLC film contaminated with macroparticles produced by conventional PLD technique, b) DLC film deposited with a curved magnetic duct [13].* 5

Figure 6. *Plasma density cross-section at the exit of the curved solenoid. Plasma is offset towards the outer wall of the solenoid.* 6

Figure 7. *Trajectory of a charged particle (ion) in a curved magnetic field. The field is created by an electric current flowing on z-axis.* 8

Figure 8. *The* $\mathbf{j}\times\mathbf{B}$ *force of the diamagnetic current balances the pressure-gradient force [17, p. 177].* 11

Figure 9. *Diamagnetic and "inertial" currents in a plasma cross-section.* 13

Figure 10. *Trajectories of 50 ions launched through a curved magnetic filter calculated by direct integration of ion's equation of motion [21].* 15

Figure 11. *Corresponding particle patters at the entrance (a) and at the exit (b) of the solenoid [21].* 15

Figure 12. *Advance from time n to n + 1 is done by introducing two fictitious layers "*" and "**". Direction* x_3 *is not shown for clarity.* 30

Figure 13. *Computational cells and interfaces in ADI scheme.* 31

Figure 14. *Cell-centred spatial discretization.* 32

Figure 15. *Newton-Raphson iterations.* 34

Figure 16. *Outgoing disturbance at the left boundary.* 38

Figure 17. *Normalized Alfven velocity and attenuated Alfven velocity vs normalized plasma density. Normalized attenuation parameter* $\rho'_{crit} = 0.2$ 41

Figure 18. *Growth rate* ξ *(attenuation) for* $grad^2$ *(solid line) and* $grad^4$ *(dashed line) spatial filters* ($\alpha = 10^{-4}$, $\beta = 8\cdot10^{-3}$). *Note that* $grad^4$ *efficiently removes short-scale*

spatial components (higher k) while keeping the long scale features of the solution (low k). In contrast, grad^2 is less superior in suppressing high-k numerical instabilities and leads to wash out of features. ... 43

Figure 19. *Grad^2 and grad^4 accumulated amplification after 1000 timesteps. Shown are $\xi^{1000}_{grad\,2}$ ($\alpha = 10^{-4}$, solid line) and $\xi^{1000}_{grad\,4}$ ($\beta = 8 \cdot 10^{-3}$, dashed line).* ... 44

Figure 20*. Cylindrical coordinates are used to model curvilinear solenoid.* ... 45

Figure 21. *Plasma offset in the radial direction (from the minor axis of the solenoid)...* 47

Figure 22*. Propagation of plasma cloud in a curved solenoid. Half maximum density contours are shown at 0, 1, 2, and 3 μsec after the start of the simulation. Geometrical dimensions are in cm.* ... 48

Figure 23. *Plasma peak density evolution.* ... 48

Figure 24. *Total plasma mass evolution.* ... 49

Figure 25. *Evolution of the average magnetic field divergence (normalized).* ... 50

Figure 26. *Cross-field current density $\mathbf{j}_\perp$ (statamp/cm^2) in the cross-section of the solenoid after 1 μsec. Position of the cross-section corresponds to the centre of the plasmoid.* ... 51

Figure 27. *Divergence of the cross-field current $\mathbf{j}_\perp$ (10^6 statamp/cm^3) in the cross-section of the solenoid after 1 μsec. Position of the cross-section corresponds to the centre of the plasmoid.* ... 52

Figure 28. *Divergence of the cross-field current $\mathbf{j}_\perp$ (10^6 statamp/cm^3) in the cross-section of the solenoid (side view) after 1 μsec. Position of the cross-section corresponds to the centre of the plasmoid.* ... 52

Figure 29*. Field-aligned current density j|| (statamp/cm^2) in the cross-section of the solenoid (side view) after 1 μsec. Position of the cross-section corresponds to the centre of the plasmoid.* ... 53

Figure 30. *Schematic representation of the currents structure in the plasma. Side view.* 53

Figure 31. *Charge density (10^{-6} statcoulomb/cm^3) distribution in the cross-section of the solenoid after 1 μsec. Position of the cross-section corresponds to the centre of the plasmoid.* ... 55

Figure 32. *Trajectory of an ion (singly charged Carbon) launched in a curved (R = 75 cm) magnetic field (1 kG) with initial velocity $7 \cdot 10^6$ cm/sec. Top view.* 60

Figure 33. *Vertical displacement (curvature drift) z of an ion along the length of solenoid L.* 61

Figure 34. *Carbon ion trajectories in 1kG curved magnetic field with electric field of charge separation taken into account. Electric field corresponds to plasma densities of 10^4 cm^{-3} (ion stays within solenoid), 10^6 cm^{-3} (ion deviates from magnetic lines), and 10^{13} cm^{-3} (ion travels in a straight line).* 62

Figure 35. *Charge separation in 1kG curved magnetic field (R = 75 cm) as a function of plasma density.* 62

Figure 36. *Dielectric susceptibility of Carbon plasma. Curved magnetic field guiding is efficient if $\chi \ll 1$ (above the thick line). Squared area represents experimental plasma parameters of interest.* 64

Figure 37. *Shorting of curvature drifts $v_{\nabla B}$ with cross-B resistive currents j.* 66

Figure 38. *Dependence of plasma offset (cm) on χ and σ (sec^{-1}). Values of $L = r_0 = 70$ cm and $v_{||} = 7 \cdot 10^6$ cm/sec were used.* 67

Figure 39. *Dependence of plasma deviation from the solenoid axis vs guiding parameter γt_0.* 68

Figure 40. *Log_{10} of plasma cross-field conductivity (sec^{-1}) vs plasma density n (in cm^{-3}) and magnetic field flux B (in Gauss). Values of T = 5 eV were used. Square dotted region represents experimental plasma parameters.* 70

Figure 41. *Log_{10} of plasma guiding parameter γt_0 vs plasma density n (in cm^{-3}) and magnetic field flux B (in Gauss). Values of $t_0 = 10$ μsec and T = 5 eV were used. Region above the dashed line corresponds to $\chi \leq 1$. Square dotted region represents experimental plasma parameters.* 71

Figure 42. *Dependence of guiding parameter on plasma temperature ($n = 10^{13}$ cm^{-3}, B = 1 kG, 3 kG).* 72

Figure 43. *Plasma offset (cm) at the exit of the solenoid vs plasma density n (in cm^{-3}) and magnetic field flux B (in Gauss). Values of $t_0 = 10$ μsec and T = 5 eV were used. Square dotted region represents experimental plasma parameters.* 73

Figure 44. *Schematic representation of plasma guiding region in n-B parametric plane. $C_1 - C_2 - C_4 - C_5$ satisfies $\gamma t_0 = 1$ and separates the regions of guiding ("+") and non-guiding ("-").* *74*

Glossary of Symbols

m_i, m_e - ion mass, electron mass

ω_{ce}, ω_{ci} - electron/ion cyclotron frequency (gyrofrequency)

ω_{pe}, ω_{pi} - electron/ion plasma frequency (gyrofrequency)

c – speed of light

r_L - Larmor radius (gyroradius)

$v_\perp$, $v_\parallel$ - velocity perpendicular/parallel to magnetic field lines

σ – charge density, or electrical conductivity (depending on context)

σ_{Sp} – plasma Spitzer conductivity

ν_{ei}, ν_{ie} - electron-ion/ion-electron collision rate

η – plasma electrical resistivity

ρ – plasma mass density

B – magnetic induction

E – electric field

P – plasma pressure

β – plasma beta (ratio of thermal pressure to magnetic pressure)

j – electric current density

κ – dielectric constant

χ – plasma dielectric susceptibility

Z – ionization state

Note: Gaussian (cgs) system of units is used.

1. Introduction

1.1 Motivation

The production of thin films has become a widely used technique in modern industry. Its utilization ranges from wear and chemical resistant coatings [1] [2], optical films [3], to microelectronics [4] where semiconductor films are used in production of integrated circuits.

A great variety of techniques has been developed for thin film deposition. In *Chemical Vapour Deposition* [5] (CVD) a film forms on a substrate as a solid phase product of a surface chemical reaction. Chemical reactants are introduced in a gaseous form and the reaction can be activated either by means of glow-discharge plasma electrons, hot filament plasma or by exposure to ion beam. In most cases, the required temperatures of the substrate are high (>1000°C), however high deposition rates can typically be achieved (~1μm/hr). Contrary to that, in *Physical Vapour Deposition* (PVD) techniques, the film is formed as a result of direct exposure to the flux of the target particles (neutrals or ionized atoms/molecules). The required flux of target particles can be generated by a number of methods. It could be simply *evaporated* from the target with an electron beam, hot filament, or from a resistively heated boat. In *sputtering* methods, the ion (molecular) flux of target material is produced by bombarding a solid target with energetic particles. For example, in *glow discharge* sputtering applications [6], the discharge plasma ions (typically Argon plasma) collide with the negatively biased target to eject the target particles (Figure 1). Sputtering yield can be enhanced by creating a magnetic field (*magnetron*) parallel to the target to trap the plasma particles near its surface thus increasing the collision rate [7].

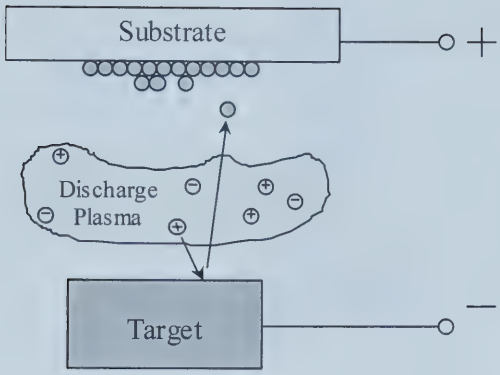

Figure 1. Glow-discharge sputtering deposition schematics.

In the *Ion Beam Deposition* technique, a hot filament ion source can be used to produce the required ions to deposit them directly onto the substrate (*Primary Ion Beam Deposition*), or it can be used to generate a secondary ion flux by bombarding a solid target (*Ion Beam Sputtering*) (Figure 2) [8].

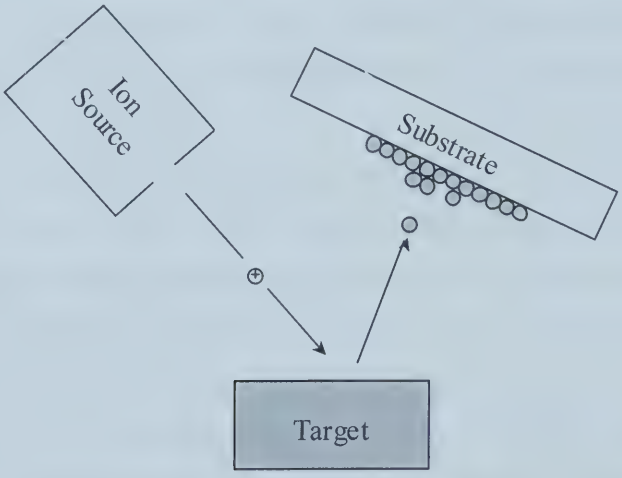

Figure 2. Schematics of Ion Beam Sputtering deposition technique.

Recently, a *Pulsed Laser Deposition* (PLD) (also called *laser sputtering*) technique has become popular. A laser beam focused onto a solid target evaporates its surface and produces an expanding plasma plume [9] consisting of target ions and electrons.

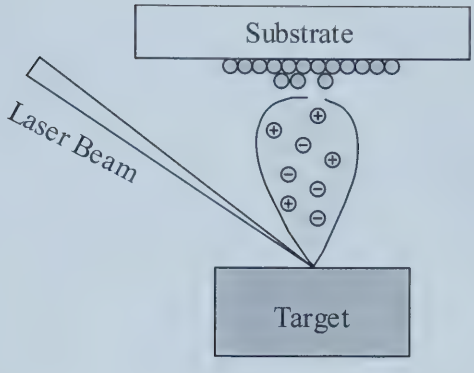

Figure 3. Schematics of Pulsed Laser Deposition technique.

The main advantage of laser sputtering is that the substrate can be kept at a relatively low temperature (<100°C) that allows film deposition onto temperature sensitive materials. The major problem of the PLD is contamination of the film with macroparticles of nanometre to micrometer size. These debris particles are ejected from the target after the hot plasma has expanded and arise from the unloading of a shock wave driven into the target by the pressure pulse from the high temperature plasma. This can significantly decrease the quality of the produced films. In addition, the coating flux falls off rapidly with distance from the target. Thus if high coating rates are desired, the substrate must be placed close to the plasma source. Typically, the plasma plume produced by a laser beam has an angular flux distribution of $cos^n(\theta)$ where the value of n varies from 4 to 8 depending on the energy, duration and wavelength of the laser pulse, and the size of the focal spot [10, 11].

A magnetic filter described in [12, 13] is designed to be free of these drawbacks. The key idea is to confine and guide the expanding plasma by the use of a curved magnetic field (Figure 4).

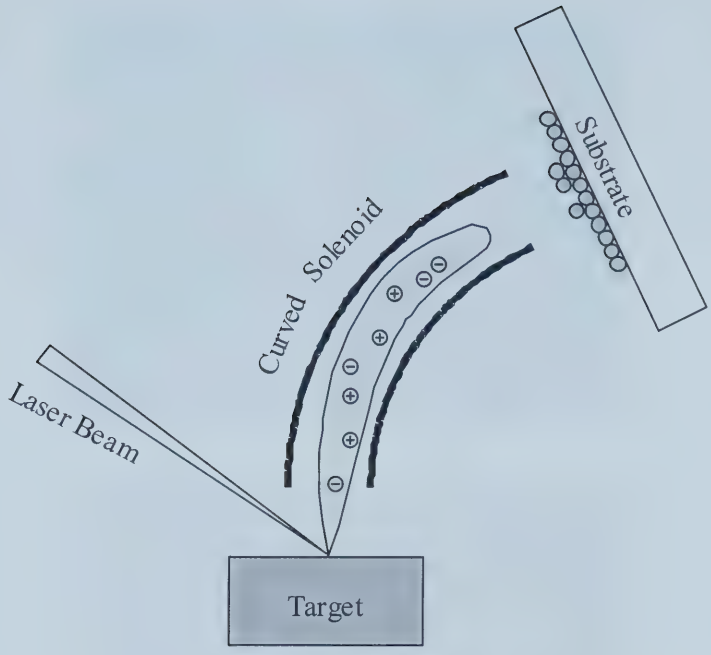

Figure 4. Schematics of PLD with curved solenoid used to guide the plasma.

Based on single-particle arguments, ions and electrons are expected to follow the curved magnetic field lines, whereas the debris macroparticles that have a small charge to mass ratio should not be diverted by the magnetic field, and will travel along the straight lines away from the target. Besides that, being confined, the plasma plume can be delivered over larger distances from the target without significant loss in deposition flux densities.

In the studies on diamond-like Carbon film (DLC) laser deposition conducted at the University of Alberta, the following experimental setup has been used. A Carbon target was irradiated with an intense 20 ns KrF laser pulse resulting in production of 5 eV plasma plume with the density of 10^{13} cm^{-3} and with an ion kinetic energy ~ 0.5 keV. A magnetic filter in a form of a curved solenoid with 75 cm radius of curvature capable of generating a 1 kG magnetic field was used to guide the plasma. Significant improvement of the film quality compared to the films produced with a straight solenoid has been demonstrated (Figure 5). However, substantial reduction in the ion flux density has also been reported. As opposed to the experiments with a straight solenoid where approximately 80% of the produced plasma was captured and transported, only a 20% fraction of the ejected ions were delivered to the substrate [14, 15, 16] using curved magnetic guide.

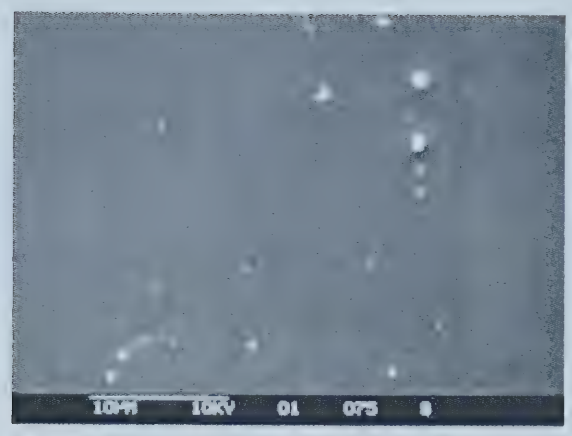

(a)

(b)

Figure 5. Microphotograph of a) DLC film contaminated with macroparticles produced by conventional PLD technique, b) DLC film deposited with a curved magnetic duct [13].

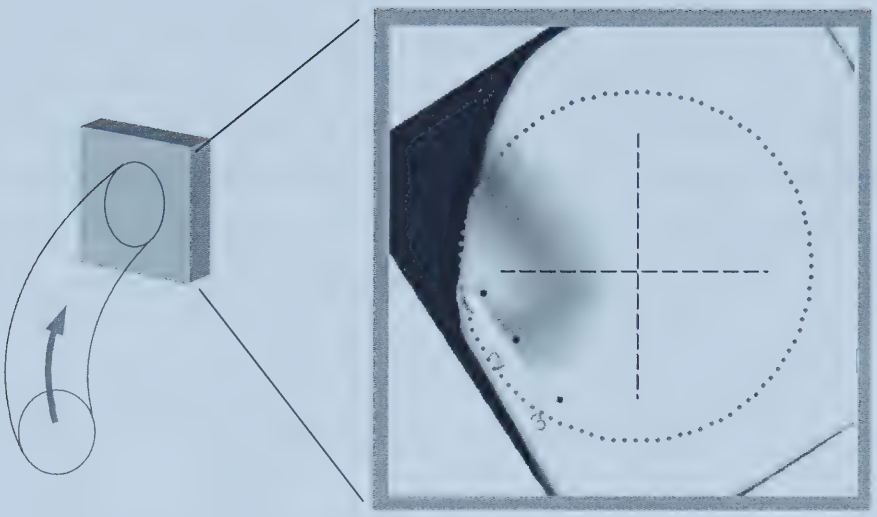

Figure 6. Plasma density cross-section at the exit of the curved solenoid. Plasma is offset towards the outer wall of the solenoid.

At the output of the curved solenoid, the plasma cloud is offset towards the outer wall of the solenoid (Figure 6). This suggests that poor plasma guiding can be attributed to the plasma loss on the wall of the solenoid.

It has also been reported [12, 13] that utilization of higher magnetic fields (up to 3 kG) can improve plasma guiding and minimize the plasma offset at the exit of the solenoid.

As expected, plasma plume confinement and guiding can be enhanced and, thus, higher deposition rates can be achieved by a proper choice of magnetic field strength and structure.

1.2 Physical Mechanisms of Plasma Guiding

1.2.1 Charged Particle Perspective

Since plasma is a collection of ions and electrons (and neutrals), and the dominant mechanism of interaction between charged particles in a plasma is via electromagnetic fields, it is usually a good starting point to understand a single charged particle dynamics in electric and magnetic fields. Particle dynamics are governed by the Lorentz equation of motion:

$$m\frac{\partial \mathbf{v}}{\partial t} = q\left(\mathbf{E} + \frac{\mathbf{v}\times\mathbf{B}}{c}\right) \tag{1.1}$$

A good introduction to the charged particle motions under various electromagnetic fields configurations is given by Chen [17]. The most fundamental type of motion is a *Larmor gyration* around a magnetic field line with an angular frequency ω_c called *cyclotron frequency* (or *gyrofrequency*) and a *Larmor radius* r_L:

$$\omega_c \equiv \frac{|q|B_G}{mc} = \begin{cases} 1.8\cdot 10^{10}\,\dfrac{\text{rad}}{\text{sec}}, & \text{electrons} \\ 8\cdot 10^{5}\,\dfrac{\text{rad}}{\text{sec}}, & \text{Carbon ions} \end{cases} \quad (\text{for } B = 1 \text{ kG}) \tag{1.2}$$

$$r_L = \frac{v_\perp}{\omega_c} = \begin{cases} 0.5 \text{ mm, electrons} \\ 0.8 \text{ cm, Carbon ions} \end{cases} \quad (T_e = T_i = 5 \text{ eV}, B = 1 \text{ kG}) \tag{1.3}$$

The above numerical values are calculated for the typical experimental conditions on plasma guiding. It is important to note that because of vastly different mass, electrons have much smaller Larmor radius than ions at the same temperature. It is also worth noting that electron cross-field velocity $v_\perp$ is by $\sqrt{m_i/m_e} = 148$ times higher than that of a Carbon ion at the same temperature. In a straight uniform B-field, a charged particle moves in helicoidal trajectory gyrating around the same field line. In the absence of collisions, only motion along the field lines is allowed and particles never moves across the magnetic field. Confining plasma with a magnetic field is possible because of this remarkable phenomenon.

If an electric field exists perpendicular to the **B**-field, a constant drift in the **E**×**B** direction will be superimposed over the helicoidal particle motion. This is known as the **E**×**B** drift and is given by:

$$\mathbf{v}_E = c\frac{\mathbf{E}\times\mathbf{B}}{B^2} \tag{1.4}$$

The **E**×**B** drift is the same for ions and electrons and thus does not lead to any charge separation acting on plasma as a solid body.

If magnetic field lines happen to be curved, a charged particle will experience other type of drifts known as *curvature* and *grad-B drift*. The first drift is caused by curved magnetic field lines, while the second happens because of the spatial variations of

the field magnitude (*i.e.* field magnitude gradient). Curved field will necessarily have a gradient of its magnitude, which follows from the requirement of zero divergence. Therefore, curvature and gradient drifts always occur together, and always add up. Both drifts are perpendicular to the magnetic field and to the radius of curvature (Figure 7) and are given by:

$$\mathbf{v}_{\perp B} = \mathbf{v}_R + \mathbf{v}_{\nabla B} = \frac{cm}{q}\frac{\mathbf{R}_c \times \mathbf{B}}{R_c^2 B^2}\left(v_\parallel^2 + \frac{1}{2}v_\perp^2\right) \tag{1.5}$$

where $v_\perp$ and $v_\parallel$ are particle's velocities in the directions perpendicular and parallel to field lines respectively. It is important that field line curvature does not lead to any radial drifts, i.e. the projection of the particles trajectory on *x*-*y* plane (Figure 7) precisely follow the field lines. This can make us think of the vertical curvature/grad *z*-drift as of a cause for $\mathbf{v}_{\perp B} \times \mathbf{B}$ Lorentz force necessary for particles to follow the curved field lines.

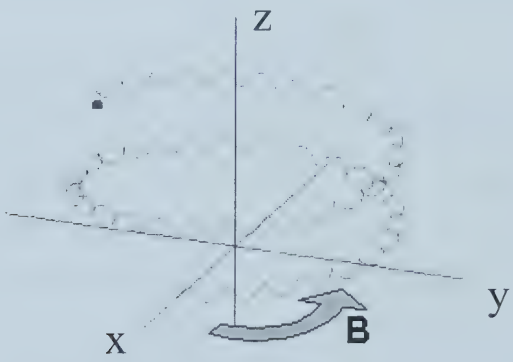

Figure 7. Trajectory of a charged particle (ion) in a curved magnetic field. The field is created by an electric current flowing on *z*-axis.

As evident from (1.5), in curved magnetic field electrons and ions drift in opposite directions, which is equivalent to an electric current flowing in the direction of ion drift. Since the drift velocity is proportional to particle's mass, it is substantially higher for ions than for electrons to the extent that electrons can be considered as frozen into the magnetic field. As one can see, curvature drifts for our experimental parameters are significant (1.6) and would result in a spatial separation between ions and electrons on the order of several centimetres as the plasma travels along the solenoid (~ 10 μsec).

$$v_{\nabla B} \sim \begin{cases} 6.7 \cdot 10^3 \text{cm/sec}, & \text{Carbon ions} \\ -6.7 \cdot 10^3 \text{cm/sec}, & \text{electrons} \end{cases}$$
$$v_R \sim \begin{cases} 8.1 \cdot 10^5 \text{ cm/sec}, & \text{Carbon ions} \\ -37 \text{ cm/sec}, & \text{electrons} \end{cases} \quad (1.6)$$

where B = 1kG, R = 75 cm, $v_{\|} = 7 \cdot 10^6$ cm/sec, and T = 5 eV. Of course, such charge separation would lead to an enormous electric field development. This field would immediately cause an $\mathbf{E} \times \mathbf{B}$ drift pointed in the radial direction, which would sweep the particle away from the field lines. However, in presence of a growing electric field, a charged particle will experience another type of drift motion known as the *polarization drift*. For ions it occurs in the direction of **E**-field change, and is opposite for electrons:

$$\mathbf{v}_p = \pm \frac{c}{\omega_c B} \frac{\partial \mathbf{E}}{\partial t} \text{ (‘+’ for ions, ‘-‘ for electrons)} \quad (1.7)$$

As the direction of this drift is charge dependent, it leads to a *polarization current*:

$$\mathbf{j}_p = ne\left(\mathbf{v}_{ip} - \mathbf{v}_{ep}\right) = \frac{\rho}{B^2} \frac{\partial \mathbf{E}}{\partial t} \quad (1.8)$$

where ρ is the plasma mass density. Note that the polarization current always tends to redistribute the electric charge in such a way as to diminish the growing electric field. In other words, plasma shields out alternating electric fields.

It was recognized a long time ago [18] that $\mathbf{E} \times \mathbf{B}$ drifts can be the main mechanism responsible for the poor plasma guiding in curved fields. However, it is not immediately straightforward which trajectory the particle will follow when in plasma. The developing electric field is not constant, and depends on the balance of particle’s drifts. In addition, the effect of particle collisions in plasma can be important and should be accounted for.

1.2.2 Fluid Approach: Magnetohydrodynamics

Another approach, called magnetohydrodynamics (MHD) treats the plasma as a conducting fluid. It is represented by a set of time-dependent partial differential equations consisting of the fluid equations (Navier-Stokes type) combined with Maxwell’s equations [19]. Depending on the physical assumptions that are made, certain terms can be included or neglected in the MHD equations. For example, single-fluid or two- and more fluids equations describing various plasma particles species can be used, which may

or may not include such aspects as particles collisions, Hall effect, viscosity, charge separation, electrical resistivity, thermal conductivity, gravity, etc. Formally, the magnetohydrodynamics model is derived from the plasma kinetic equations by taking their first few velocity moments. Despite the significant number of approximations made, the MHD model conserves mass, momentum, and energy, both locally and globally. This is one of the basic reasons for the reliability of this approach.

The governing fluid equation required to demonstrate the effect of plasma confinement by an externally applied magnetic field is the single-fluid equation of motion describing the mass flow [17, pp. 177-181]:

$$\rho \frac{d\mathbf{v}}{dt} = \frac{\mathbf{j} \times \mathbf{B}}{c} - \nabla P + \rho \mathbf{g} \tag{1.9}$$

where ρ - is the plasma mass density, $\mathbf{v}$ – is the fluid velocity, $\mathbf{j}$ – is electrical current density, $\mathbf{B}$ – is the magnetic flux, $\rho \mathbf{g}$ - is the gravitational (or inertial) force. Consider a plasma cloud in cylindrical coordinates with an external magnetic field directed along the axis. A thermal pressure gradient resulting from the density gradient will exist along the radial direction forcing plasma to expand. Ignoring the gravity, in the equilibrium state ($d/dt = 0$) equation (1.9) yields:

$$\frac{\mathbf{j} \times \mathbf{B}}{c} = \nabla P \tag{1.10}$$

To prevent the radial expansion of plasma the pressure-gradient force must be balanced by the Lorenz force, appearing as a result of an electric current in the azimuthal direction (Figure 8). The magnitude of this current can be found by taking the cross product of $\mathbf{B}$ with (1.10):

$$\mathbf{j}_{\perp} = c \frac{\mathbf{B} \times \nabla P}{B^2} \tag{1.11}$$

Currents like (1.11) are called *diamagnetic currents* and arise from the particles Larmor gyration velocities not averaging to zero in the presence of a pressure gradient. This diamagnetic current itself is a result of the pressure-gradient force acting across the magnetic field $\mathbf{B}$.

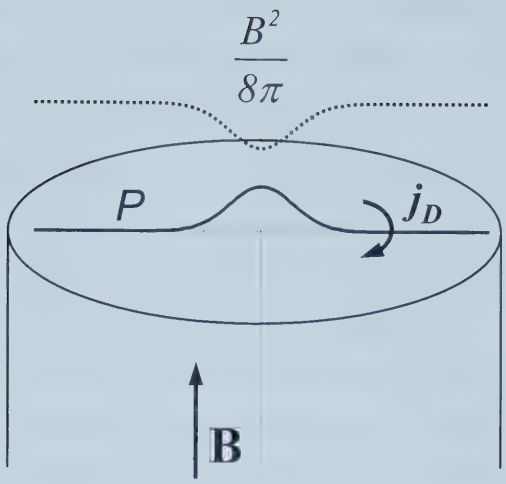

Figure 8. The **j**×**B** force of the diamagnetic current balances the pressure-gradient force [17, p. 177].

One should always take into account that **j** and **B** are both perpendicular to ∇P. The diamagnetic current in the plasma generates its own magnetic field that is superimposed over the external magnetic field. By its nature, diamagnetic currents are directed in such fashion as to reduce the external magnetic field. An equivalent equilibrium condition can be obtained after substituting $\nabla \times \mathbf{B} = \frac{4\pi}{c}\mathbf{j}$ into (1.10):

$$\nabla\left(P + \frac{B^2}{8\pi}\right) = 0 \tag{1.12}$$

This equation suggests that the sum of the plasma thermal pressure P and magnetic pressure $\frac{B^2}{8\pi}$ must be constant across the plasma in order for the force balance. This means that in a plasma with a density gradient, the magnetic field must be low where the density is high, and vice versa. A plasma is often said to be confined in a magnetic "well". The "depth" of this well can be characterized by the ratio of maximum thermal pressure to maximum magnetic pressure, usually denoted as β:

$$\beta \equiv \frac{P}{B^2/8\pi} = \frac{nkT}{B^2/8\pi} \tag{1.13}$$

If $\beta \ll 1$, the diamagnetic effect is very small, and magnetic field can be considered uniform. In case when $\beta = 1$, magnetic field reduces to zero inside the "well". For successful magnetic confinement, magnetic field has to be strong enough to provide $\beta < 1$. Our experimental plasma has $\beta \sim 10^{-2} - 10^{-4}$ when 1 kG magnetic field is used. From this, one would expect a very good plasma confinement in the solenoid. While this is indeed observed in the experiments with a straight magnetic guides, in curved solenoids the plasma does not exactly follow the solenoid axis but tends to drift towards the wall. The difference is that β characterizes plasma *thermal* expansion, but in the case of a curved solenoid, magnetic pressure gradient forces have to work against *inertial* (centrifugal) forces. Following the same logics as we did deriving (1.12) it is possible to show that now the magnetic pressure gradient force $\nabla \frac{B^2}{8\pi}$ has to balance the inertial force $\rho v^2 / R$, where R is the radius of the field curvature. Similarly to (1.13) we can introduce a concept of inertial beta as

$$\beta_{inertial} = \frac{\rho v^2 / R}{B^2 / 8\pi} \Delta r \qquad (1.14)$$

where Δr is the plasma dimension perpendicular to field lines (along the radius of curvature). Inertial forces arising in the experiments on plasma guiding in curved fields are quite substantial, and may well exceed the magnetic pressure forces. Thus, if a plasma with 3 cm cross-field dimension and density $n = 10^{13}$ cm^{-3} streams with velocity 10^7 cm/sec along a curved magnetic field (R = 70 cm), its inertial β would be $2 \cdot 10^{-2}$. Compared to thermal β of $2 \cdot 10^{-3}$, this suggests that plasma guiding in curved fields requires considerably stronger B-field than a simple confinement of plasma thermal expansion.

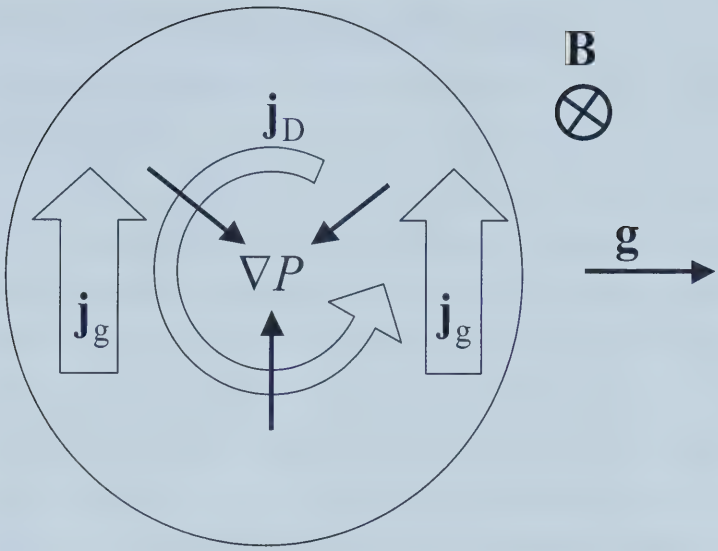

Figure 9. Diamagnetic and "inertial" currents in a plasma cross-section.

Equation (1.9) can be solved for the equilibrium case while keeping gravitational (or inertial) term. The required current will consist of two components (Figure 9): one is the familiar diamagnetic current $\mathbf{j}_D$ and the other is a current $\mathbf{j}_g$ required to balance the gravitational/inertial force:

$$\mathbf{j}_\perp = \mathbf{j}_D + \mathbf{j}_g = c\frac{\mathbf{B}\times\nabla P}{B^2} - \rho c\frac{\mathbf{B}\times\mathbf{g}}{B^2} \tag{1.15}$$

It is customary to replace centrifugal force in curved field geometries with gravity force to simplify the analysis. In the former case the "inertial" current $\mathbf{j}_g$ becomes:

$$\mathbf{j}_g \equiv \mathbf{j}_{curv} = \rho c\frac{\mathbf{R}_c\times\mathbf{B}}{R_c^2 B^2}v_{\|}^2 \tag{1.16}$$

It is easy to recognize (1.16) as the current resulting from curvature/gradient drifts (1.5).

We have identified the diamagnetic current as the mechanism for confinement of plasma thermal expansion, and the "inertial" current as the mean for inertial force balance. There is a significant difference between the two currents: the diamagnetic current is closed, or divergence-free, which means it does not lead to charge pile-up, while the "inertial current" is "open" and should lead to charge separation at the top and the bottom of the plasma cloud. This charge will create a vertical electric field, which in turn will push plasma in the direction of **g** (or along the radius of curvature).

1.3 Overview of Plasma Guiding Modeling

The most simplistic approach taken to study plasma guiding in magnetic fields is to examine single charged particle motion in the corresponding field geometries. This has been done analytically, as in [20] where particle trajectory in curved field is found from its Lagrangian, or numerically [21, 22, 23]. Typically, magnetic field of a realistic guiding solenoid is accurately calculated (from the solenoid electric currents distribution using Biot-Savart law), and a particle's trajectory is calculated by integrating its equation of motion ([24] describes a very accurate technique). Often, a Monte-Carlo-type analysis is employed, when a large number of trajectories corresponding to a certain initial energy distribution (e.g. Maxwellian) and initial launching angles distribution (e.g. $\cos^n$) is calculated (Figure 10, Figure 11). Statistics are collected, yielding the ratio of passed/stopped particles (sometime called the "filter efficiency"), particles' density distribution at the exit of the solenoid, etc. However, by considering the motion of individual charged particles, it would be fairly easy to design a magnetic filter that will perfectly confine and guide the plasma. One would only need to ensure that the field is strong enough for the Larmor orbits to be smaller than the solenoid inner diameter, that the magnetic field lines do not hit the tube walls, and to arrange the symmetry of the system in such a way that all the particle drifts are parallel to the walls. The problem is that once the collective interactions of the plasma particles are taken into account, it is not easy to determine whether the plasma will be confined in a magnetic field designed to contain individual particles. No matter how the external fields are arranged, plasma can generate its own internal electric and magnetic fields, which in turn affect its motion. Interaction between particles and fields manifests itself in such critical effects as external electric field shielding (Debye shielding), diamagnetic currents and magnetic pressure, plasma thermal pressure, charge separation, plasma-wall sheath formation, and effects associated with particle collisions. Nevertheless, a single particle tracing in an external B-field provides a useful low-density plasma approximation.

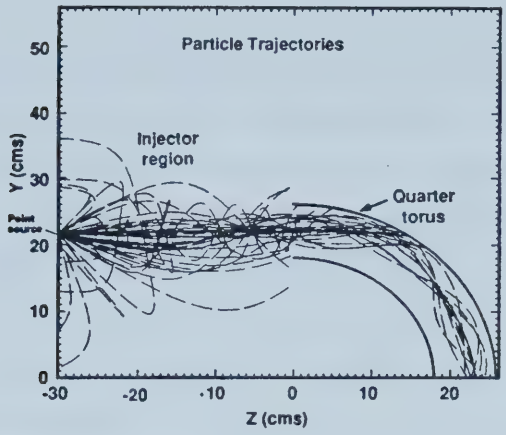

Figure 10. Trajectories of 50 ions launched through a curved magnetic filter calculated by direct integration of ion's equation of motion [21].

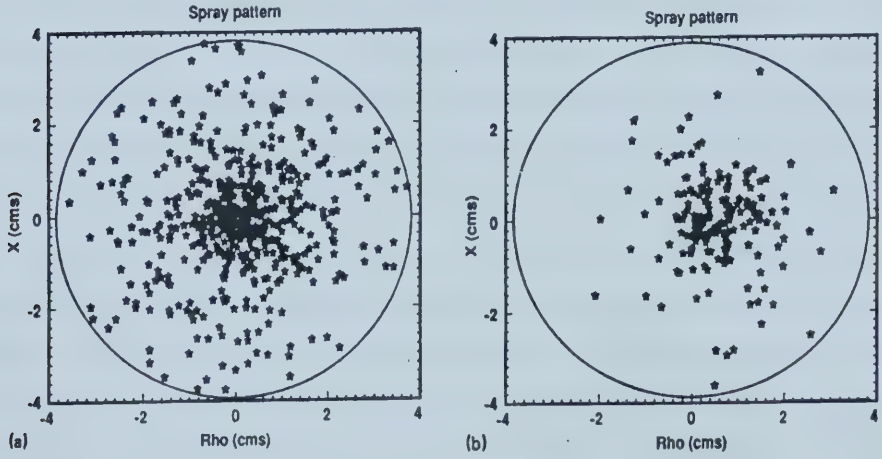

Figure 11. Corresponding particle patters at the entrance (a) and at the exit (b) of the solenoid [21].

The next level of sophistication of single charged particle paradigm takes into consideration self-generated electric fields that result from charge separation caused by curvature drifts. This is usually done by evaluating guiding centers drifts in a self-consistent particle-field model (such as [18, 25, 20, 26]). Schmidt [18] was the first to recognize the curvature driven charge separation as a major obstacle for effective plasma guiding. His analytical model was further developed by including terms like particle collisions ([25, 20, 26]) and an arbitrary plasma electric potential distribution [27]. The latter electric potential is typically deduced from the plasma stability considerations. In

[27, 28], a guiding centre trajectory analytically calculated from such model is superimposed with Larmor gyration orbits calculated numerically. Again, a Monte-Carlo analysis could be applied to a large number of single-particle runs.

This approach is a definite improvement over the pure single-particle model. However, it still does not account for the variations of plasma density inside the solenoid and for plasma-generated magnetic fields. However, it does allow for a straightforward analysis of different ionization states dynamics, as well as for varying distributions of particles' initial velocities (Maxwellian, Maxwellian with different parallel and perpendicular temperatures, etc.).

The most comprehensive type of plasma filter analysis would be based on a simultaneous tracing of multiple particles trajectories. With the appearance of powerful, especially parallel, computers, these methods have become available. Modern 'Particle-in-Cell' (PIC) codes [29, 30, 31] can trace up to 10^9 or more particles simultaneously, accurately describing collective effects. This technique is one of the most powerful modeling approaches available because it represents certain kinetic details of anisotropic plasmas, of microscopic instabilities, of finite Larmor radius effects, as well as other effects better than the alternative fluid models. However, the rich details available from these particle simulations come at a formidable computational expense. Unfortunately, the author has not yet seen any references about the PIC methods used in magnetic plasma filters characterization. One of the reasons could be attributed to the large number of particles in a typical laser ablation shot ($\sim 10^{15}$) that would need to be traced, even when this number is scaled down. This still exceeds the capabilities of the most powerful computers by several orders of magnitude.

The magnetohydrodynamical approach is based on a set of fluid-like equations coupled with Maxwell's equations. By its nature, they are partial differential equations (PDEs), nonlinear in general case, constituting a time-dependent initial value problem (transient problems) or a boundary value problem (steady-state problems), and can therefore be treated numerically with a variety of methods developed for this class of mathematical problems. It is beyond the scope of this paper to give a detailed overview of numerical methods available for solving PDEs. A practical introduction could be found for example in [32]. Nevertheless, several methods, common in magnetohydrodynamical

numerical simulations, will be mentioned. The set of unknown quantities that constitute the solution (typically, these are density, velocity, magnetic field, pressure, etc.), also known as *state variables*, generally vary in space and time. The major classification of the methods is done according to the state variables *spatial discretization* algorithms and *time advancing* procedures.

The simplest technique involves *finite differencing* and *explicit* time advancing [33]. Finite difference discretization of the spatial domain is done by introducing a structured rectangular mesh and specifying the state variables on its nodes. The term 'explicit' means that the solution at time t_{n+1} is advanced by calculating the required spatial derivatives from the known solution at the previous moment t_n. The major drawback of all explicit schemes is a severe timestep limitation known as the *Courant condition*. It can be shown that in order for an explicit numerical scheme to be stable (numerical errors are not amplified), its timestep Δt has to be inversely proportional to the mesh spacing Δx and to the characteristic velocities appearing in the model. For an MHD problem, the latter factor is extremely critical. The *Alfven velocity* is characteristic for plasmas, and becomes a limiting factor. As known, Alfven waves propagate faster in low-density plasmas, meaning that low-density regions, which are usually not important for the problem, and thus the whole problem, must be calculated with a very small timestep. Thus, the entire numerical scheme becomes very inefficient. However, there are advantages that make explicit schemes popular: ease of implementation and straightforward application on parallel computer architectures.

A class of *implicit* time advance algorithms gives a significant improvement on the size of the timestep that can be employed. Calculated at the unknown time-layer t_{n+1}, the spatial derivatives couple the neighbouring points of the computational grid to form typically a large matrix that has to be inverted at every timestep in order to find the solution. The dimensionality of the matrix is equal to the dimensionality of the numerical grid. Applied to *linear* equations, implicit schemes are known to be *unconditionally stable*, independently of the timestep, *i.e.* the timestep can to be chosen based on the desired accuracy of numerical approximation, rather then on the stability of numerical scheme. However, when applied to *nonlinear* equations, the Courant condition appears even for implicit schemes. Nevertheless, it is not as severely limiting as in explicit

schemes. In two- and especially in three-dimensional simulations, the inversion of the resulting 2D or 3D matrix at each time-step becomes the most time consuming operation of the entire scheme. To overcome this drawback, a class of *Alternating Direction Implicit* (ADI) algorithms had been developed and successfully used for MHD simulations [34, 35]. The idea of the ADI technique is to approximate the multidimensional time step iteration with a sequence of one-dimensional steps. Thus, an inversion of only one-dimensional matrices is required. These algorithms, based on finite differencing can be efficiently implemented for multiprocessor parallel computer architectures [36].

Finite difference discretization is easy to implement, but is usually limited to the computational domains where boundaries are aligned with the coordinate planes. In a case of irregular boundary geometry, finite differencing can still be used, but the accuracy of the spatial numerical approximation of the boundary and, thus, of the entire scheme, decreases from the second to the first order. In addition, discretization on an irregular boundary becomes a cumbersome task. A class of *Finite Elements* (FE) methods [37] can be successfully exploited for a computational domain of a general geometry. The idea is to expand the solution in an orthogonal basis over the computational domain and then to solve the resulting system of equations for the expansion coefficients. Unlike *Spectral Methods*, where basis functions are defined over the entire computational domain (i.e. *sin* and *cos*), each FE basis function is non-zero only within its own spatial element. Commonly, triangular (in 2D) or tetrahedral (3D) spatial elements are chosen. This allows for a very flexible *meshing* of an irregularly shaped domain. However, resulting in an unstructured mesh, FE methods are typically more computationally involved than finite difference schemes.

In general, the complete MHD problem also includes a set of appropriate boundary conditions to couple the plasma behaviour to the externally applied magnetic fields. For transient (time-dependent) problems, physically justified initial conditions must be established.

Three most common classes of boundary conditions are: 1) plasma surrounded by a perfectly conducting wall, 2) plasma isolated from a perfectly conducting wall, and 3) plasma surrounded by external coils. The last condition would provide an accurate

description of the experimental magnetic filter. However, it would require solving a complicated "free boundary" problem for the plasma-vacuum interface. Since the MHD model treats a plasma as a continuous fluid across the computational domain, one way to deal with vacuum regions would be to introduce a small, but finite "background" density plasma in these regions, so that mathematically a vacuum would never occur. The problem arising here is that the Alfven wave velocities become very high in the regions of low plasma density, which would severely limit the computational time step. In principle, one can suppress these low-density waves by introducing certain smoothing terms in the MHD equations or by advancing in time only those regions where the density is above certain "critical" density [38].

The initial conditions are often chosen in a form of a linearly stable equilibrium state, which is then perturbed to initiate a nonlinear behaviour. This approach is usually utilized in tokamak plasma modeling. To set the proper initial conditions for a laser produced plasma which is far from any equilibrium state, one of the following approaches can be chosen: 1) rely on the experimental data, 2) include the ionization stage and plasma formation from the target as a part of the computational scheme, which would require a laser-plasma interaction code [39, 40, 41], or 3) set the initial conditions relying on certain physically motivated approximations. For example, in [42] the initial temperature and density were homogeneous inside a sphere, the initial fluid velocity was a linear function of the radius, and magnetic field was zero inside the sphere. Special care should be taken in order to construct an initial state consistent with the MHD equations. For example, magnetic field should have zero divergence in the entire computational domain, to satisfy Maxwell's equations.

Several attempts were made in modeling plasma guiding in magnetic filters by using the MHD approach. These have mainly been done for plasma cathodic arc jet expansion into curved magnetic fields. These works are based on a two-dimensional MHD model [43, 44]. The modeling results demonstrate an arc plasma shift towards the outer wall of the solenoid, which is used to explain poor plasma guiding. However, the plasma guiding mechanism could be essentially three-dimensional, which would set the limit of applicability of these studies. The authors did not analyse the time-dependent

dynamics, and obtained a numerical solution for an established steady-state arc regime. Noticeably, a plasma free boundary was obtained as a part of solution.

1.4 Scope of Present Work and Thesis Structure

This study attempts to explain and characterize the mechanism of plasma guiding in curved solenoids.

An introduction to the problem along with a historical overview of modeling of the guiding mechanism were provided in Chapter 1.

In Chapter 2, the problem of guiding is studied using a magnetohydrodynamical description of plasma interaction with magnetic field. The underlying single fluid magnetohydrodynamical model is developed in §2.1. Further in this chapter, this model is used to study the guiding phenomenon numerically. The corresponding three-dimensional ADI numerical method and techniques are described in detail in §2.2. The results of the modeling and their discussion are presented in §2.3. The limitations of the MHD model in addressing plasma guiding are also discussed.

In Chapter 3, an alternative model based on a charged particle perspective is developed. Cross-field resistive currents are introduced and characterized as a potential mechanism responsible for plasma guiding in curved magnetic fields.

A summary of the results and conclusions are given in Chapter 4.

2. Single-Fluid Magnetohydrodynamics

While a single-particle description provides valuable insight into plasma dynamics, it lacks substantial details of plasma collective effects. In this chapter, we will build a magnetohydrodynamical model of plasma interacting with a magnetic field. A derivation of single-fluid MHD equations will be presented in §2.1. Its validity and limitations will be demonstrated with the focus on the experimental conditions of interest. The numerical technique used to solve the model will be presented in detail in §2.2. Results of the modeling will be presented and discussed in §2.3.

2.1 Single-Fluid MHD Model

Plasma dynamics can be described in full detail by solving a plasma kinetic model, *e.g.* Fokker-Planck equations for the plasma electrons' and ions' (and neutrals, in the case of partially ionized plasma) distribution functions [45, 46]. However, in most cases this will require enormous efforts and will produce an excessively detailed solution. Quite often, certain details of the solution may not be required for a particular plasma dynamics problem. In a typical case, the dimensionality of the kinetic model can be greatly reduced by assuming a Maxwellian distribution of plasma particles velocities, which can be characterized by a single scalar quantity, temperature. Taking the first few velocity moments of the kinetic equations for electrons and ions and combining them with Maxwell equations leads to a two-fluid hydrodynamic plasma model [19]. This describes fully ionized plasmas (i.e. cross-sections of ion-neutral and electron-neutral collisions are neglected compared to charged particles collisional cross-sections).

$$\frac{\partial n_\alpha}{\partial t} + \nabla \cdot n_\alpha \mathbf{v}_\alpha = 0, \quad \alpha = i, e \tag{2.1}$$

$$n_e m_e \left(\frac{\partial \mathbf{v}_e}{\partial t} + (\mathbf{v}_e \cdot \nabla) \mathbf{v}_e \right) = -n_e e \left(\mathbf{E} + \frac{\mathbf{v}_e \times \mathbf{B}}{c} \right) - \nabla p_e - \nabla \cdot \boldsymbol{\pi}_e + \mathbf{P}_{ei} \tag{2.2}$$

$$n_i m_i \left(\frac{\partial \mathbf{v}_i}{\partial t} + (\mathbf{v}_i \cdot \nabla) \mathbf{v}_i \right) = n_i q_i \left(\mathbf{E} + \frac{\mathbf{v}_i \times \mathbf{B}}{c} \right) - \nabla p_i - \nabla \cdot \boldsymbol{\pi}_i + \mathbf{P}_{ie} \tag{2.3}$$

which are the continuity equations for ions and electrons (2.1) and momentum transfer equations (2.2), (2.3) where p_i and p_e are the ion and electron fluid pressures, π_i and π_e are the viscosity tensors (together, pressure and viscosity terms constitute the stress tensor), and $\mathbf{P}_{ei}$ and $\mathbf{P}_{ei}$ are the momentum exchange between the fluids (equal due to conservation of momentum):

$$\mathbf{P}_{ei} = -\mathbf{P}_{ie} = m_e n\left(\mathbf{v}_i - \mathbf{v}_e\right)\nu_{ei} \tag{2.4}$$

with ν_{ei} being the electron-ion collision frequency. Anisotropic viscosity tensors π_i and π_e represent like-particle collisions which give rise to stresses within electron and ion fluids individually. Since like-particle collisions do not result in much diffusion, terms $\nabla\cdot\boldsymbol{\pi}_e$ and $\nabla\cdot\boldsymbol{\pi}_i$ are typically neglected. Partial derivative $\frac{\partial\mathbf{v}}{\partial t}$ represents the change of $\mathbf{v}$ in the laboratory fixed (Eulerian) reference frame, while convective derivative $\frac{D\mathbf{v}}{Dt} \equiv \frac{\partial\mathbf{v}}{\partial t} + \left(\mathbf{v}\cdot\nabla\right)\mathbf{v}$ refers to the reference frame moving with the fluid (Lagrangian reference frame). Equivalently, convective derivative for scalar quantities is $\frac{Df}{Dt} \equiv \frac{\partial f}{\partial t} + \mathbf{v}\cdot\nabla f$.

Charge density and current densities introduced as

$$\sigma = n_i q_i - n_e e \tag{2.5}$$

$$\mathbf{j} = n_i q_i \mathbf{v}_i - n_e e \mathbf{v}_e \tag{2.6}$$

contribute to Maxwell's equations as

$$\nabla\times\mathbf{E} = -\frac{1}{c}\frac{\partial\mathbf{B}}{\partial t} \tag{2.7}$$

$$\nabla\cdot\mathbf{E} = 4\pi\sigma \tag{2.8}$$

$$\nabla\times\mathbf{B} = \frac{1}{c}\frac{\partial\mathbf{E}}{\partial t} + \frac{4\pi}{c}\mathbf{j} \tag{2.9}$$

$$\nabla\cdot\mathbf{B} = 0 \tag{2.10}$$

Each fluid requires an equation of state describing its thermal properties during compression to close the equations. In its simplest form, fluid compression can be described as isothermal $p = An$, adiabatic $p = An^{5/3}$, or even $p = 0$ which is a good

approximation for processes involving a strong magnetic field. If energy transfer is involved, an energy balance equation will be required.

The complexity of the two-fluid model can be further reduced by the following approach. By taking linear combinations of the electron and ion equations, it is possible to transform them into the equations for mass and charge flows. In other words, the model with two physical fluids, each of which has mass and charge properties, is transformed into a chargeless 'mass' fluid, and a massless 'charge' fluid. The simplification is achieved by assuming that the 'charge' fluid reaches equilibrium on a much shorter timescale than the 'mass' fluid. Thus, time derivative of the 'charge' fluid can be conveniently neglected. Also, the density of the 'charge' fluid is not allowed to be nonzero, since plasma in general should be neutral. So, essentially, the two-fluid description reduces to one-fluid ('mass') equations, while the second fluid ('charge') is assumed to be in the equilibrium state and can thus be described by an algebraic equation. This model is called *single-fluid magnetohydrodynamics*.

The 'mass' fluid is characterized by its density ρ (centre-of-mass density of ions and electrons), velocity $\mathbf{v}$, and total pressure P as

$$\rho \equiv n_i m_i + n_e m_e \tag{2.11}$$

$$\mathbf{v} \equiv \frac{n_i m_i \mathbf{v}_i + n_e m_e \mathbf{v}_e}{n_i m_i + n_e m_e} \tag{2.12}$$

$$P \equiv p_i + p_e \tag{2.13}$$

while the 'charge' fluid is characterized by electrical charge σ (2.5) and electrical current $\mathbf{j}$ (2.6). The interaction between the 'mass' and 'charge' fluids occurs through the forces the fluids exert on each other. Below we will provide a formal derivation of the single fluid MHD model to obtain the hierarchy of the terms and to formulate the criteria to neglect some of them.

Multiplying continuity equations (2.1) by m_α and adding them together gives *mass continuity equation*:

$$\frac{\partial \rho}{\partial t} + \nabla \cdot (\rho \mathbf{v}) = 0 \tag{2.14}$$

while multiplying (2.1) by q_α (corresponding particle charge) and adding both together results in a *charge continuity equation*:

$$\frac{\partial \sigma}{\partial t} + \nabla \cdot \mathbf{j} = 0 \tag{2.15}$$

Adding ion and electron momentum equations (2.2) and (2.3) gives *one-fluid momentum equation* (viscosity tensors are neglected as described earlier):

$$\rho\left(\frac{\partial \mathbf{v}}{\partial t} + (\mathbf{v}\cdot\nabla)\mathbf{v}\right) = \sigma\mathbf{E} + \frac{\mathbf{j}\times\mathbf{B}}{c} - \nabla P \tag{2.16}$$

Multiplying (2.2) by $-\frac{e}{m_e}$ and (2.3) by $\frac{q_i}{m_i}$ and adding them together gives:

$$\begin{aligned}\frac{\partial \mathbf{j}}{\partial t} + \nabla\cdot(\mathbf{vj} + \mathbf{jv} - \mathbf{vv}\sigma) = \left(\frac{n_i q_i^2}{m_i} + \frac{n_e e^2}{m_e}\right)\mathbf{E} + \left(\frac{Ze^2}{m_e} + \frac{q_i^2}{m_i}\right)\frac{\rho}{m_i + Zm_e}\frac{\mathbf{v}\times\mathbf{B}}{c} - \\ -\left(\frac{em_i}{m_e} - \frac{q_i Zm_e}{m_i}\right)\frac{1}{m_i + Zm_e}\frac{\mathbf{j}\times\mathbf{B}}{c} + \left(\frac{e}{m_e}\nabla p_e - \frac{q_i}{m_i}\nabla p_i\right) - \mathbf{P}_{ei}\left(\frac{e}{m_e} + \frac{q_i}{m_i}\right)\end{aligned} \tag{2.17}$$

where Z is the ionization state ($q_i \equiv Ze$). This equation is called the *generalized Ohm's law* for plasma. Using $m_e \ll m_i$ and recalling (2.4) it can be reduced to:

$$\frac{\partial \mathbf{j}}{\partial t} + \nabla\cdot(\mathbf{vj} + \mathbf{jv} - \mathbf{vv}\sigma) = \frac{n_e e^2}{m_e}\mathbf{E} + \frac{n_i q_i e}{m_e}\frac{\mathbf{v}\times\mathbf{B}}{c} - \frac{e}{m_e c}\mathbf{j}\times\mathbf{B} + \frac{e}{m_e}\nabla p_e - \nu_{ei}\mathbf{j} \tag{2.18}$$

These equations can be further simplified by making the following assumptions [46, pp. 92 - 95]:

- Quasineutrality of plasma (mathematically $\frac{n_i q_i - n_e e}{n_e e} \ll 1$) leads to disappearance of the charge density σ. Even though the charge density is neglected, the electric field **E** it produces is important and should not be ignored. Quasineutrality is valid on the length scales greater than Debye length $\lambda_D = \left(\frac{kT}{4\pi n e^2}\right)^{1/2}$. For experimental plasma densities of $\sim 10^{13}$ cm^{-3} and temperatures of few eV, Debye length will be on the order of few microns only, which justifies the neglect of space charge on the centimetre scale of interest.
- Frequently $\nabla\cdot(\mathbf{vj} + \mathbf{jv}) = 0$ is assumed. This assumption is rather difficult to justify but since these terms arise from $(\mathbf{v}\cdot\nabla)\mathbf{v}$ in the momentum equations, and

the latter would be a second order term around an equilibrium value, it can typically be ignored.

- Time variations of the current $\partial \mathbf{j}/\partial t$ are fast - on the order of plasma electron oscillations time scale $\omega_{pe} = \left(\frac{4\pi n e^2}{m_e} \right)^{1/2}$ and thus can be ignored if low frequency dynamics is studied, i.e. if $\frac{L^2}{c^2}\omega_{pe}^2 \gg 1$ (it is $\sim 10^3$ for the plasma parameters of interest).
- Electron pressure ∇p_e can be neglected if $\frac{L\nu_0\omega_{ce}}{kT_e/m_e} \gg 1$. This ratio is $\sim 10^3$ for the plasma parameters of interest.
- It can be shown [47, p. 180-182] that the Hall term $\frac{e}{m_e c}\mathbf{j}\times\mathbf{B}$ gives rise to Hall current perpendicular to both electric and magnetic fields:

$$\mathbf{j}_H = \sigma_H \frac{\mathbf{B}\times\mathbf{E}}{B} \tag{2.19}$$

with Hall conductivity given by

$$\sigma_H = \frac{\omega_{ce}\tau_{ei}}{1+(\omega_{ce}\tau_{ei})^2}\sigma \tag{2.20}$$

where conductivity σ and resistivity η are defined through the collision frequency:

$$\eta \equiv \sigma^{-1} = \frac{\nu_{ei} m_e}{ne^2} \tag{2.21}$$

If the collision frequency is low, so that $\omega_{ce}\tau_{ei} \gg 1$, then $\sigma_H \ll \sigma$ and the effect of Hall term can be ignored. For the plasma parameters of interest $\omega_{ce}\tau_{ei} \simeq 10^3$ (B = 1 kG, T = 5 eV), which justifies the neglect of Hall term in our case.

After these simplifications the Ohm's law reduces to

$$\eta\mathbf{j} = \mathbf{E} + \frac{1}{c}\mathbf{v}\times\mathbf{B} \tag{2.22}$$

To close the MHD system of equations we will need an energy balance equation. It can be obtained from the 1st law of thermodynamics applied for a fluid element moving with the fluid:

$$dU = Q - W \tag{2.23}$$

where dU is the change in internal energy of the fluid element, Q is the heat added to the element, and $W = PdV$ describes the work done by the element, with P being the pressure and dV the change of the element's volume. It is convenient to work with internal energy mass density (internal energy per unit mass) $\varepsilon \equiv \frac{U}{\rho V}$. By considering the resistive heating as the main source for heat generation we can rewrite (2.23) as

$$d(\rho\varepsilon V) = \eta j^2 V dt - PdV \tag{2.24}$$

Dividing by Vdt we obtain:

$$\frac{d(\rho\varepsilon)}{dt} + \rho\varepsilon\frac{1}{V}\frac{dV}{dt} + P\frac{1}{V}\frac{dV}{dt} - \eta j^2 = 0 \tag{2.25}$$

Rewriting (2.25) for the fixed reference frame and using $\frac{1}{V}\frac{dV}{dt} = \nabla\cdot\mathbf{v}$ (this can be easily shown) we obtain the energy balance equation:

$$\frac{\partial(\rho\varepsilon)}{\partial t} + \nabla\cdot(\rho\varepsilon\mathbf{v}) + P\nabla\cdot\mathbf{v} - \eta j^2 = 0 \tag{2.26}$$

Equation (2.26) defines the internal energy change induced by ohmic heating, work against pressure forces, and convection. In principle, it may contain other terms, such as thermal conductivity, viscous heating, radiation, etc. However, to be correct, the kinetic energy $\frac{\rho v^2}{2}$ has to be added when transforming from moving to fixed reference frame.

The system requires an equation of state to relate the pressure to the density and internal energy. By considering plasma as a monatomic gas we can use

$$P = (\gamma - 1)\rho\varepsilon \tag{2.27}$$

where $\gamma = c_p/c_v$ is the ratio of specific heats of the plasma (for monatomic gas chosen as $^5/_3$).

Eventually one arrives with a set of single-fluid magnetohydrodynamic equations:

$$\frac{\partial\rho}{\partial t} + \nabla\cdot(\rho\mathbf{v}) = 0 \tag{2.28}$$

$$\rho\frac{d\mathbf{v}}{dt} \equiv \rho\left(\frac{\partial\mathbf{v}}{\partial t} + (\mathbf{v}\cdot\nabla)\mathbf{v}\right) \equiv \frac{\partial(\rho\mathbf{v})}{\partial t} + \nabla\cdot(\rho\mathbf{v}\cdot\mathbf{v}) = -\nabla P + \frac{1}{c}\mathbf{j}\times\mathbf{B} \tag{2.29}$$

$$\frac{\partial \rho\varepsilon}{\partial t}+\nabla\cdot\left(\rho\varepsilon\mathbf{v}\right)+P\nabla\cdot\mathbf{v}-\eta\mathbf{j}^2=0 \tag{2.30}$$

$$\eta\mathbf{j}=\mathbf{E}+\frac{1}{c}\mathbf{v}\times\mathbf{B} \tag{2.31}$$

$$P=\left(\gamma-1\right)\rho\varepsilon \tag{2.32}$$

$$\nabla\times\mathbf{E}=-\frac{1}{c}\frac{\partial\mathbf{B}}{\partial t} \tag{2.33}$$

$$\nabla\times\mathbf{B}=\frac{4\pi}{c}\mathbf{j} \tag{2.34}$$

The number of equations can be reduced in the following way. Eliminating the current **j** from Ohm's law (2.31) by use of Ampere's law (2.34) and substituting the resulting electric field **E** into (2.33) gives the equation for magnetic field:

$$\frac{\partial\mathbf{B}}{\partial t}-\nabla\times\left(\mathbf{v}\times\mathbf{B}-\frac{c^2\eta}{4\pi}\nabla\times\mathbf{B}\right)=0$$

Substituting the current **j** from the Ampere's law (2.34) into the momentum equation (2.29) gives:

$$\frac{\partial\left(\rho\mathbf{v}\right)}{\partial t}+\nabla\cdot\left(\rho\mathbf{v}\cdot\mathbf{v}\right)+\nabla P+\frac{1}{4\pi}\mathbf{B}\times\left(\nabla\times\mathbf{B}\right)=0 \tag{2.35}$$

$$\frac{\partial\rho}{\partial t}+\nabla\left(\rho\mathbf{v}\right)=0 \tag{2.36}$$

Substituting the internal energy ε from the equation of state (2.32) and the current from the Ampere's law into the energy equation (2.30) results in

$$\frac{\partial P}{\partial t}+\nabla\left(\gamma P\mathbf{v}\right)-\left(\gamma-1\right)\left\{\mathbf{v}\nabla P+\frac{c^2\eta}{16\pi^2}\left(\nabla\times\mathbf{B}\right)\right\}=0 \tag{2.37}$$

As a result, single fluid resistive MHD equations can be expressed in the following convenient form:

$$\frac{\partial\mathbf{B}}{\partial t}-\nabla\times\left(\mathbf{v}\times\mathbf{B}-\frac{c^2\eta}{4\pi}\nabla\times\mathbf{B}\right)=0 \tag{2.38}$$

$$\frac{\partial\left(\rho\mathbf{v}\right)}{\partial t}+\nabla\cdot\left(\rho\mathbf{v}\cdot\mathbf{v}\right)+\nabla P+\frac{1}{4\pi}\mathbf{B}\times\left(\nabla\times\mathbf{B}\right)=0 \tag{2.39}$$

$$\frac{\partial \rho}{\partial t} + \nabla(\rho \mathbf{v}) = 0 \tag{2.40}$$

$$\frac{\partial P}{\partial t} + \nabla(\gamma P \mathbf{v}) - (\gamma - 1)\left\{ \mathbf{v}\nabla P + \frac{c^2 \eta}{16\pi^2}(\nabla \times \mathbf{B})^2 \right\} = 0 \tag{2.41}$$

2.2 Numerical technique: ADI

Being a set of second-order coupled partial differential equations, the above system can be solved analytically only in very limited special cases. Most physical problems with realistic geometries require numerical treatment. In the course of the current research a three-dimensional ADI-like scheme [48, 36] was utilized in order to model plasma dynamics in curved magnetic ducts. A fully curvilinear 3D FORTRAN code based on an earlier Cartesian coordinates version has been developed. The Cartesian version of the code was provided by the research group studying the Earth's magnetosphere at the University of Alberta. In the course of the development of the numerical technique, special attention was paid to the low-density vacuum-like regions and non-reflective "transparent" boundary conditions. A ∇^4 (similar to numerical diffusion) spatial filtering technique was introduced in order to eliminate short-scale numerical instabilities appearing at larger time steps.

2.2.1 Curvilinear Coordinates

Depending on the geometry and symmetry of the physical problem of interest, an appropriate system of coordinates can be chosen to solve the above MHD equations. Examples include: toroidal coordinates for tokamaks, cylindrical coordinates for z-pinches, and a dipole coordinate system for the Earth's magnetosphere. However, a numerical code developed for one coordinate system cannot be easily applied to another. To have the flexibility of selecting an arbitrary coordinate system, a numerical code was written for the equations (2.38) - (2.41) expressed in generalized orthogonal curvilinear coordinates. Curvilinear orthogonal coordinates (x_1, x_2, x_3) can be characterized by means of *metric coefficients*, or scale factors (h_1, h_2, h_3). Element of length ds in such coordinates can be found as

$$ds^2 \equiv h_1^2 dx_1^2 + h_2^2 dx_2^2 + h_3^2 dx_3^2 \tag{2.42}$$

Metric coefficient can be found from the relations between the curvilinear (x_1, x_2, x_3) and Cartesian (X, Y, Z) coordinates:

$$h_n^2 = \left(\frac{\partial X}{\partial x_n}\right)^2 + \left(\frac{\partial Y}{\partial x_n}\right)^2 + \left(\frac{\partial Z}{\partial x_n}\right)^2 \tag{2.43}$$

Thus, for Cartesian coordinates $(x_1, x_2, x_3) = (x, y, z)$ they are unities $(h_1, h_2, h_3) = (1,\ 1,\ 1)$, for cylindrical $(x_1, x_2, x_3) = (\rho, \varphi, z)$ they are $(h_1, h_2, h_3) = (1, \rho, 1)$, and for spherical coordinates $(x_1, x_2, x_3) = (r, \theta, \varphi)$ they become $(h_1, h_2, h_3) = (1, r, r\sin\theta)$.

Differential operators of *gradient*, *divergence,* and *curl* can be expressed in curvilinear coordinates through their metric coefficients [49]. For example, grad φ, *div* **v**, and curl **v** are:

$$\nabla\varphi = \sum_i h_i^{-1} \frac{\partial \varphi}{\partial x_i} \mathbf{e}_i \tag{2.44}$$

$$\nabla \cdot \mathbf{v} = \sum_i \sqrt{g}^{-1} \frac{\partial}{\partial x_i}\left(\sqrt{g}\frac{v_i}{h_i}\right),\ g = (h_1 h_2 h_3)^2 \tag{2.45}$$

$$\nabla \times \mathbf{v} = \sum_i \frac{h_i \hat{\mathbf{e}}_i}{\sqrt{g}} \sum_{l,m} \varepsilon_{ilm} \frac{\partial h_m v_m}{\partial x_l} \tag{2.46}$$

where ε_{ijk} is the Levi-Civita permutation symbol. This allows the MHD equations to be expressed in generalized curvilinear coordinates specified through (h_1, h_2, h_3). However, the algebra becomes cumbersome. A symbolic algebraic package, Maple® V.5 [50] in our case, can greatly simplify this task. The MHD equations expressed in generalized curvilinear coordinates can be found in the Appendix.

2.2.2 Time Discretization

The MHD equations (2.38) - (2.41) written in orthogonal curvilinear coordinates can be expressed as:

$$\frac{\partial \mathbf{T}(\mathbf{u})}{\partial t} + \mathbf{F}(\mathbf{u}) + \mathbf{G}(\mathbf{u}) + \mathbf{H}(\mathbf{u}) = 0 \tag{2.47}$$

where **F**, **G** and **H** represent spatial differential terms with leading derivatives $\partial/\partial x_1$, $\partial/\partial x_2$, $\partial/\partial x_3$ respectively, **T** = {**B**, ρ**v**, ρ, P} are the quantities advanced in time, and **u** =

$\{\mathbf{B}, \mathbf{v}, \rho, P\}$ is the state vector. **F**, **G** and **H** terms in component form can be found in the Appendix.

Advancing the state vector from timestep n to $n+1$ is done as a three-step sequence by introducing two fictitious intermediate time layers "*" and "**" so that $\mathbf{u}^n \rightarrow \mathbf{u}^* \rightarrow \mathbf{u}^{**} \rightarrow \mathbf{u}^{n+1}$. Each step is then essentially a one-dimensional boundary value problem (Figure 12):

$$\frac{\mathbf{T}(\mathbf{u}^*)-\mathbf{T}(\mathbf{u}^n)}{\Delta t}+\frac{\mathbf{F}(\mathbf{u}^*)+\mathbf{F}(\mathbf{u}^n)}{2}+\mathbf{G}(\mathbf{u}^n)+\mathbf{H}(\mathbf{u}^n)=0 \tag{2.48}$$

$$\frac{\mathbf{T}(\mathbf{u}^{**})-\mathbf{T}(\mathbf{u}^*)}{\Delta t}+\frac{\mathbf{G}(\mathbf{u}^{**})-\mathbf{G}(\mathbf{u}^n)}{2}=0 \tag{2.49}$$

$$\frac{\mathbf{T}(\mathbf{u}^{n+1})-\mathbf{T}(\mathbf{u}^n)}{\Delta t}+\frac{\mathbf{H}(\mathbf{u}^{n+1})-\mathbf{H}(\mathbf{u}^n)}{2}=0 \tag{2.50}$$

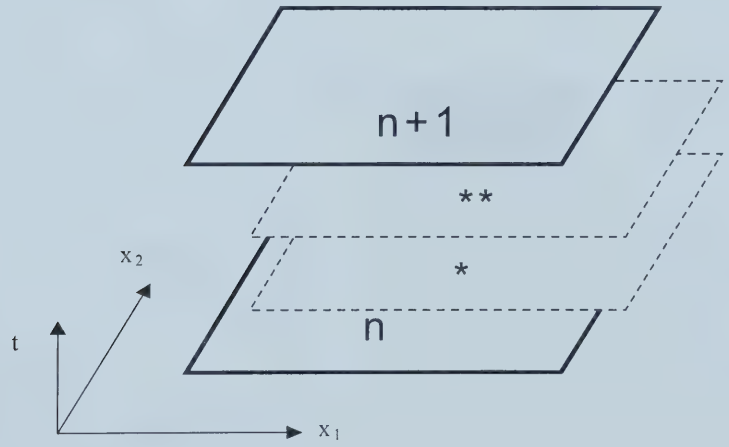

Figure 12. Advance from time n to $n + 1$ is done by introducing two fictitious layers "*" and "**". Direction x_3 is not shown for clarity.

This scheme is known as a Douglas-Gunn three-dimensional extension to a standard (two-dimensional) ADI scheme [51]. Equation (2.48) solves for $\mathbf{u}^*$ with $\mathbf{u}^n$ known, (2.49) solves for $\mathbf{u}^{**}$ ($\mathbf{u}^*$ and $\mathbf{u}^n$ are known), and (2.50) for $\mathbf{u}^{n+1}$. Each of the three sub-steps deals only with corresponding one-dimensional space derivatives at the unknown time-layer, *i.e.* $\partial/\partial x_1$ in (2.48), $\partial/\partial x_2$ in (2.49) and $\partial/\partial x_3$ in (2.50). This forms the essence of an ADI technique - the idea is to replace three-dimensional dynamics occurring over the timestep Δt with three one-dimensional sub-steps.

2.2.3 Spatial Discretization

Spatial discretization is done in the form of *cell-centred* finite differences. A structured rectangular mesh (*i.e.* with gridlines aligned with curvilinear coordinate axis) with nonuniform (in general) spacing is introduced in the computational domain. Variables {**B**, **v**, ρ, P} representing values averaged over three-dimensional *cells* are stored at the mesh *nodes* (Figure 13). Cell walls (interfaces) are placed midway between the nodes. Physically, state variables {**B**, **v**, ρ, P} experience changes because of the action of *fluxes* and *forces* applied to the cells, which are evaluated at the cells' interfaces.

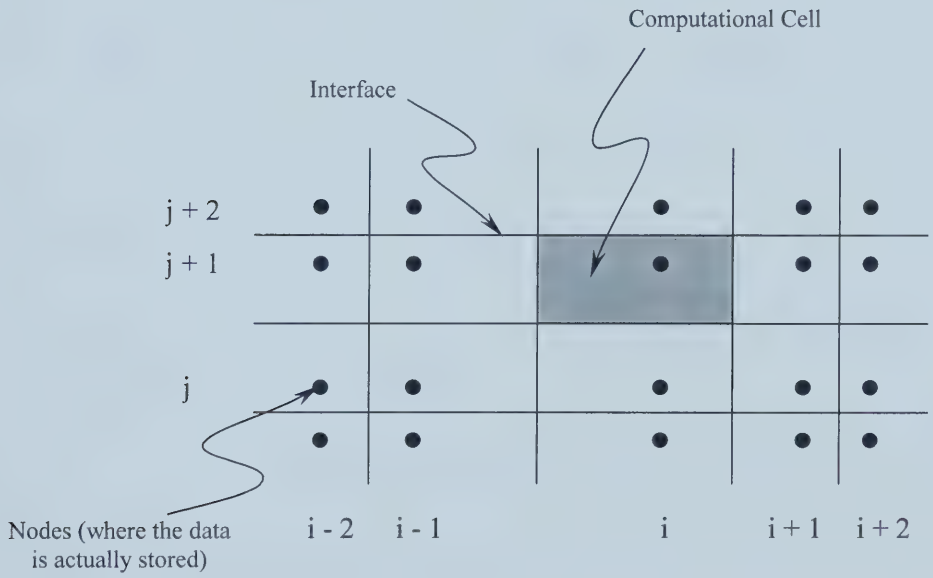

Figure 13. Computational cells and interfaces in ADI scheme.

To see how the spatial derivatives are calculated on the mesh let us introduce the following notation (Figure 14):

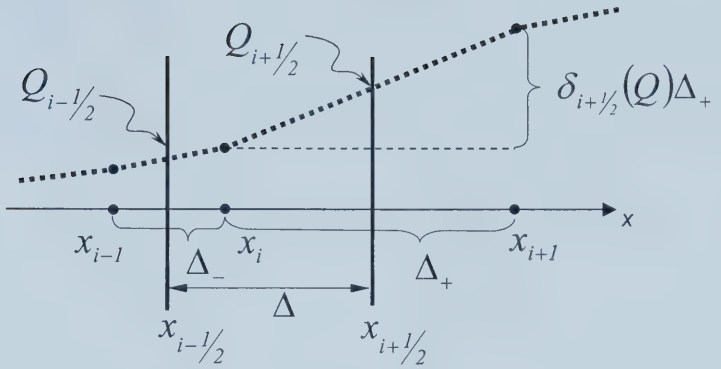

Figure 14. Cell-centred spatial discretization.

- distance between nodes $\Delta_- \equiv x_i - x_{i-1}$, $\Delta_+ \equiv x_{i+1} - x_i$
- interface position $x_{i+1/2} \equiv \frac{1}{2}(x_i + x_{i+1})$, $x_{i-1/2} \equiv \frac{1}{2}(x_i + x_{i-1})$
- distance between interfaces $\Delta_i \equiv \frac{1}{2}(\Delta_+ + \Delta_-) = x_{i+1/2} - x_{i-1/2}$
- value of a variable Q at the interface $Q_{i+1/2} \equiv \frac{1}{2}(Q_{i+1} + Q_i)$, $Q_{i-1/2} \equiv \frac{1}{2}(Q_{i-1} + Q_i)$
- change of Q across the interface

$$\delta_{i+1/2}(Q) \equiv \frac{1}{\Delta_+}(Q_{i+1} - Q_i),\ \delta_{i-1/2}(Q) \equiv \frac{1}{\Delta_-}(Q_i - Q_{i-1})$$

MHD equations expressed in component form (see the Appendix) contain spatial derivatives of two types: *fluxes* and *forces*:

- *FLUX* terms are of a form $\frac{\partial}{\partial x_1}(\alpha Q)$, where Q is any general factor, *e.g.* $\frac{\partial}{\partial x_1}(P v_1 h_1 h_3)$, Q can also be a derivative across another direction $\frac{\partial \psi}{\partial x_2}$. Flux terms measure flows into or out of the computational cell, and thus must be evaluated at the cell boundaries as

$$\frac{\partial}{\partial x}(\alpha Q)_i \rightarrow \frac{\alpha_{i+1/2} Q_{i+1/2} - \alpha_{i-1/2} Q_{i-1/2}}{\Delta_i} \qquad (2.51)$$

which can be written as $FLUX_i = \frac{A_{i+1/2} - A_{i-1/2}}{\Delta_i}$.

- *FORCE* terms are $\alpha \frac{\partial Q}{\partial x_1}$ terms, where α is a function of (**B**, **v**, ρ, P), for example $B_1 \frac{\partial B_1}{\partial x_1}$, or $\frac{\partial P}{\partial x_1}$. Force terms represent forces applied on the edges of the computational cell, and thus defined as an average of the forces applied on each cell's face

$$\left(\alpha \frac{\partial Q}{\partial x}\right)_i \rightarrow \frac{1}{2}\left[\alpha_{i+1/2}\delta_{i+1/2}(Q) + \alpha_{i-1/2}\delta_{i-1/2}(Q)\right] \tag{2.52}$$

This can be written as $FORCE_i = S_{i-1/2} + S_{i+1/2}$.

2.2.4 Newton-Raphson linearization

Each of the ADI equations (2.48) - (2.50) is a one-dimensional boundary-value problem. However, being nonlinear they cannot be solved directly. In ADI, a Newton-Raphson iterative technique is used to solve them. Consider, for example, the first equation (2.48). An iterative procedure has to be built that solves $\mathbf{f}(\mathbf{u}^*) = 0$ which is

$$\mathbf{f}(\mathbf{u}^*) \equiv \frac{\mathbf{T}(\mathbf{u}^*) - \mathbf{T}(\mathbf{u}^n)}{\Delta t} + \frac{\mathbf{F}(\mathbf{u}^*) + \mathbf{F}(\mathbf{u}^n)}{2} + \mathbf{G}(\mathbf{u}^n) + \mathbf{H}(\mathbf{u}^n) = 0 \tag{2.53}$$

The idea of Newton-Raphson linearization and iterations can be introduced with a one-dimensional scalar equation:

$$f(x) = 0$$

The idea is to *linearize* the equation around a *guess solution*, solve the linearized equation (which is trivial), and use the new solution for the next approximation. In other words, the solution can be found as a converging sequence ${}^m x \rightarrow {}^{m+1}x \rightarrow {}^{m+2}x \rightarrow \ldots \rightarrow x_0$ by linearizing our equation at a point ${}^m x$ as

$$f({}^m x) + \left.\frac{\partial f}{\partial x}\right|_{{}^m x} {}^m\delta x = 0 \tag{2.54}$$

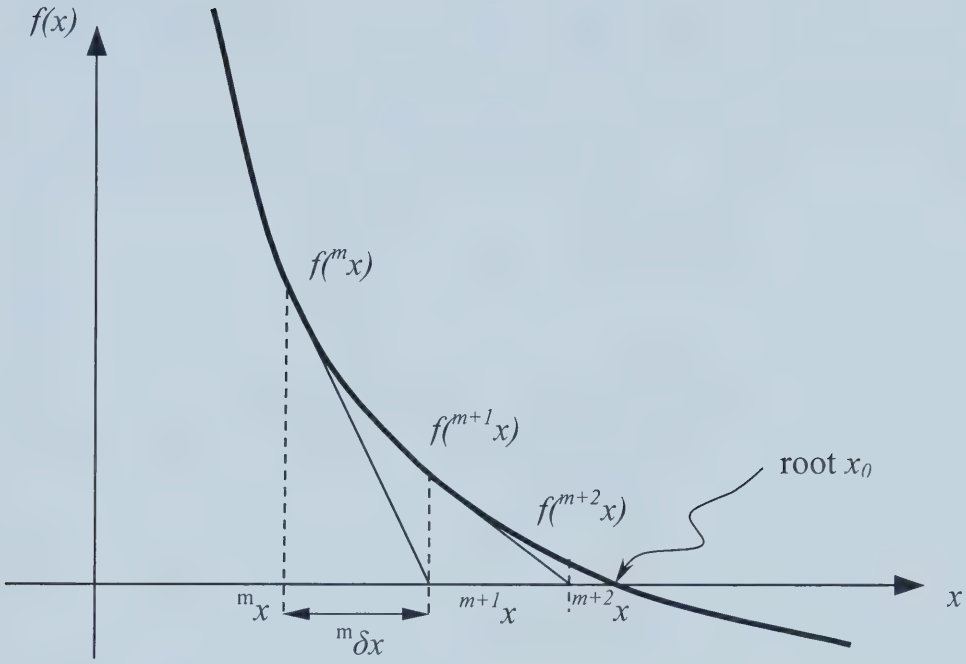

Figure 15. Newton-Raphson iterations.

solving for ${}^{m}\delta x$, updating x as

$$ {}^{m+1}x \leftarrow {}^{m}x + {}^{m}\delta x \tag{2.55} $$

and iterating this procedure until we get close enough to the solution x_0 , *i.e.* until the increment ${}^{m}\delta x$ becomes small enough (Figure 15).

This idea can be generalized for solving multidimensional equations of the form $\mathbf{f}(\mathbf{x}) = 0$, where $\mathbf{f}(\mathbf{x}) = \{f_1(\mathbf{x}), f_2(\mathbf{x}), f_3(\mathbf{x}), \ldots, f_k(\mathbf{x})\}$ is a k-dimensional vector-function defined over k-dimensional space $\mathbf{x} = \{x_1, x_2, x_3, \ldots, x_k\}$ (number of equations and number of unknowns must be equal). Multidimensional Newton-Raphson method becomes:

$$ \mathbf{f}\left({}^{m}\mathbf{x}\right) + {}^{m}\hat{\mathbf{J}} \cdot {}^{m}\delta\mathbf{x} = 0 \tag{2.56} $$

$$ {}^{m+1}\mathbf{x} \leftarrow {}^{m}\mathbf{x} + {}^{m}\delta\mathbf{x} \tag{2.57} $$

where $\hat{\mathbf{J}}$ is the Jacobian of the function $\mathbf{f}(\mathbf{x})$:

$$\hat{\mathbf{J}} \equiv \frac{\partial \mathbf{f}(\mathbf{x})}{\partial \mathbf{x}} \equiv \begin{bmatrix} \frac{\partial f_1}{\partial x_1} & \frac{\partial f_1}{\partial x_2} & . & \frac{\partial f_1}{\partial x_k} \\ \frac{\partial f_2}{\partial x_1} & . & . & . \\ . & . & . & . \\ \frac{\partial f_n}{\partial x_1} & . & . & \frac{\partial f_n}{\partial x_k} \end{bmatrix} \tag{2.58}$$

Terms in equation (2.53) can be grouped into *implicit* part that has dependence on unknown $\mathbf{u}^*$ and *explicit* part that depends only on the known $\mathbf{u}^n$:

$$\mathbf{f}(\mathbf{u}^*) \equiv \mathbf{f}^{imp}(\mathbf{u}^*) + \mathbf{f}^{exp}(\mathbf{u}^n) = 0 \tag{2.59}$$

At the *i*-th mesh node the latter equation can thus be linearized as:

$$\hat{\mathbf{J}}^i_{i-1} \cdot \delta\mathbf{u}^*_{i-1} + \hat{\mathbf{J}}^i_i \cdot \delta\mathbf{u}^*_i + \hat{\mathbf{J}}^i_{i+1} \cdot \delta\mathbf{u}^*_{i+1} = -\mathbf{f}^{imp}(\mathbf{u}^*_{i-1}, \mathbf{u}^*_i, \mathbf{u}^*_{i+1}) - \mathbf{f}^{exp}(\mathbf{u}^n) \tag{2.60}$$

where the Jacobians are:

$$\hat{\mathbf{J}}^i_{i-1} \equiv \frac{\partial \mathbf{f}^{imp}_i}{\partial \mathbf{u}^*_{i-1}} \qquad \hat{\mathbf{J}}^i_i \equiv \frac{\partial \mathbf{f}^{imp}_i}{\partial \mathbf{u}^*_i} \qquad \hat{\mathbf{J}}^i_{i+1} \equiv \frac{\partial \mathbf{f}^{imp}_i}{\partial \mathbf{u}^*_{i+1}} \tag{2.61}$$

Note that equation (2.60) is to be solved for $\delta\mathbf{u}^*_{i-1}, \delta\mathbf{u}^*_i$ and $\delta\mathbf{u}^*_{i+1}$. Jacobians (2.61) can be found by expressing $\mathbf{f}(\mathbf{u}^*)$ as a sum of *fluxes*, *forces* and *only time-dependent* quantities:

$$\mathbf{f}^{imp}_i \rightarrow \mathbf{FLUX}_i + \mathbf{FORCE}_i + \mathbf{T}_i \rightarrow \frac{\mathbf{A}_{i+1/2}}{\Delta_i} - \frac{\mathbf{A}_{i-1/2}}{\Delta_i} + \mathbf{S}_{i-1/2} + \mathbf{S}_{i+1/2} + \mathbf{T}_i \tag{2.62}$$

By differentiating the latter terms with respect to $\mathbf{u}^*_{i-1}, \mathbf{u}^*_i$ and $\mathbf{u}^*_{i+1}$, the Jacobians (2.61) are found as:

$$\begin{aligned} \hat{\mathbf{J}}^i_{i-1} &\equiv \frac{\partial \mathbf{f}^{imp}_i}{\partial \mathbf{u}^*_{i-1}} = \frac{\partial}{\partial \mathbf{u}^*_{i-1}} \left(\mathbf{S}_{i-1/2} - \frac{\mathbf{A}_{i-1/2}}{\Delta_i} \right) \\ \hat{\mathbf{J}}^i_i &\equiv \frac{\partial \mathbf{f}^{imp}_i}{\partial \mathbf{u}^*_i} = \frac{\partial}{\partial \mathbf{u}^*_i} \left(\frac{\mathbf{A}_{i+1/2}}{\Delta_i} - \frac{\mathbf{A}_{i-1/2}}{\Delta_i} + \mathbf{S}_{i-1/2} + \mathbf{S}_{i+1/2} + \mathbf{T}_i \right) \\ \hat{\mathbf{J}}^i_{i+1} &\equiv \frac{\partial \mathbf{f}^{imp}_i}{\partial \mathbf{u}^*_{i+1}} = \frac{\partial}{\partial \mathbf{u}^*_{i+1}} \left(\mathbf{S}_{i+1/2} + \frac{\mathbf{A}_{i+1/2}}{\Delta_i} \right) \end{aligned} \tag{2.63}$$

By introducing new terms as

$$\hat{\mathbf{S}}_i^+ \equiv \frac{\partial \mathbf{S}_{i+1/2}}{\partial \mathbf{u}_{i+1}^*},\ \hat{\mathbf{S}}_i \equiv \frac{\partial \mathbf{S}_{i+1/2}}{\partial \mathbf{u}_i^*},\ \hat{\mathbf{A}}_i^+ \equiv \frac{\partial \mathbf{A}_{i+1/2}}{\partial \mathbf{u}_{i+1}^*},\ \hat{\mathbf{A}}_i \equiv \frac{\partial \mathbf{A}_{i+1/2}}{\partial \mathbf{u}_i^*},\ \hat{\mathbf{T}}_i \equiv \frac{\partial \mathbf{T}_i}{\partial \mathbf{u}_i^*} \tag{2.64}$$

we can write the Newton-Raphson linearization (2.60) as

$$\tilde{\mathbf{A}}_i \cdot \delta \mathbf{u}_{i-1}^* + \tilde{\mathbf{B}}_i \cdot \delta \mathbf{u}_i^* + \tilde{\mathbf{C}}_i \cdot \delta \mathbf{u}_{i+1}^* = \tilde{\mathbf{D}}_i \tag{2.65}$$

where

$$\begin{aligned}
\tilde{\mathbf{A}}_i &\equiv \hat{\mathbf{J}}_{i-1}^i \equiv \hat{\mathbf{S}}_{i-1} - \frac{\hat{\mathbf{A}}_{i-1}}{\Delta_i} \\
\tilde{\mathbf{B}}_i &\equiv \hat{\mathbf{J}}_i^i \equiv \frac{\hat{\mathbf{A}}_i}{\Delta_i} - \frac{\hat{\mathbf{A}}_{i-1}^+}{\Delta_i} + \hat{\mathbf{S}}_i + \hat{\mathbf{S}}_{i-1}^+ + \hat{\mathbf{T}}_i \\
\tilde{\mathbf{C}}_i &\equiv \hat{\mathbf{J}}_{i+1}^i \equiv \hat{\mathbf{S}}_i^+ + \frac{\hat{\mathbf{A}}_i^+}{\Delta_i} \\
\tilde{\mathbf{D}}_i &\equiv -\mathbf{f}^{imp}\left(\mathbf{u}_{i-1}^*, \mathbf{u}_i^*, \mathbf{u}_{i+1}^*\right) - \mathbf{f}^{exp}\left(\mathbf{u}^n\right)
\end{aligned} \tag{2.66}$$

Equations (2.65) form a block-tridiagonal linear system of equations, i.e. only the main and the two adjacent diagonals of its matrix are nonzero (tildes are omitted for simplicity):

$$\begin{pmatrix}
\mathbf{B}_1 & \mathbf{C}_1 & & & & & \\
\mathbf{A}_2 & \mathbf{B}_2 & \mathbf{C}_2 & & & \mathbf{0} & \\
 & \mathbf{A}_3 & \mathbf{B}_3 & \mathbf{C}_3 & & & \\
 & & \mathbf{A}_4 & \mathbf{B}_4 & \mathbf{C}_4 & & \\
 & & & \cdot & \cdot & \cdot & \\
 & \mathbf{0} & & & \mathbf{A}_{N-1} & \mathbf{B}_{N-1} & \mathbf{C}_{N-1} \\
 & & & & & \mathbf{A}_N & \mathbf{B}_N
\end{pmatrix} \cdot \begin{pmatrix}
\delta \mathbf{u}_1^* \\ \delta \mathbf{u}_2^* \\ \delta \mathbf{u}_3^* \\ \delta \mathbf{u}_4^* \\ \cdot \\ \delta \mathbf{u}_{N-1}^* \\ \delta \mathbf{u}_N^*
\end{pmatrix} = \begin{pmatrix}
\mathbf{D}_1 \\ \mathbf{D}_2 \\ \mathbf{D}_3 \\ \mathbf{D}_4 \\ \cdot \\ \mathbf{D}_{N-1} \\ \mathbf{D}_N
\end{pmatrix} \tag{2.67}$$

Note that the first and the last equations in (2.67) (corresponding to the first and N-th mesh nodes) are dictated by the boundary conditions.

This type of system of equations can be very efficiently solved with a *recursion* algorithm based on LU matrix decomposition [32]. Equations (2.65) represent Newton-Raphson iterations the way they are being used in ADI.

Evidently, an ability to compute 8×8 Jacobians (2.64) is required. In order to do this, an algebraic processor Maple® was used to symbolically differentiate $\mathbf{S}_{i+1/2}$ and $\mathbf{A}_{i+1/2}$ and to generate the Jacobians (2.64) directly in a form of FORTRAN code.

Within each one-dimensional stage of the ADI scheme (2.48) - (2.50), the Newton-Raphson iterations can be performed independently on each row. This allows the ADI scheme to be implemented on parallel computer architectures. For that, the rows of the computational domain have to be fully uncoupled. By its nature, the discretization routine described above (separation into F, G, and H components) has this property. However, the forms of F, G, and H are well defined for all but the mixed and product derivatives. Several approaches can be taken [34], each one having its own advantages and disadvantages. We chose to treat them explicitly as:

$$\left(\frac{\partial F}{\partial x_1}\frac{\partial G}{\partial x_2}\right)^* = \frac{1}{2}\left(\frac{\partial F^n}{\partial x_1}\frac{\partial G^*}{\partial x_2} + \frac{\partial F^*}{\partial x_1}\frac{\partial G^n}{\partial x_2}\right) \tag{2.68}$$

Further details on mixed and product derivatives treatment can be found in [34].

2.2.5 Boundary Conditions

To avoid a complicated description of plasma interaction and loss at the walls of the magnetic duct, we apply "transparent" or nonreflective boundary conditions allowing plasma to freely escape through the walls. These were implemented in the form known as Enquist-Majda boundary conditions [52] that treat plasma disturbances as outgoing waves at the boundaries.

We require the state vector $\mathbf{u} = \{\mathbf{B}, \mathbf{v}, \rho, P\}$ to satisfy the advection equation corresponding to the left-travelling wave at the left boundary, and right-travelling wave at the right boundary:

$$\frac{\partial \mathbf{u}(x,t)}{\partial t} - c\frac{\partial \mathbf{u}(x,t)}{\partial x} = 0 \text{ (left-going)} \tag{2.69}$$

$$\frac{\partial \mathbf{u}(x,t)}{\partial t} + c\frac{\partial \mathbf{u}(x,t)}{\partial x} = 0 \text{ (right-going)} \tag{2.70}$$

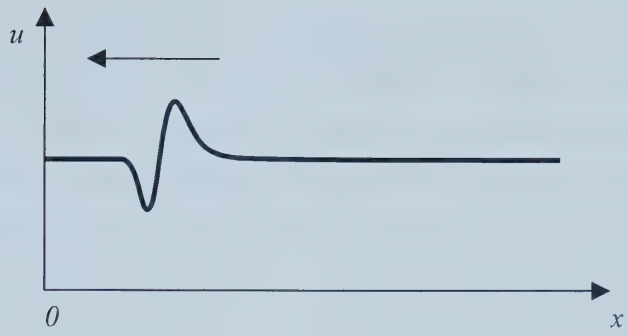

Figure 16. Outgoing disturbance at the left boundary.

Let us see how this type of boundary conditions can be incorporated into the Newton-Raphson iterative scheme (2.65). Discretization of the travelling wave equation (2.69) can be done as follows (left boundary, starting spatial index is 1):

$$\mathbf{u}_1^* - \mathbf{u}_1^n = \frac{1}{2} c \frac{\Delta t}{\Delta x} \left(\mathbf{u}_2^* - \mathbf{u}_1^* + \mathbf{u}_2^n - \mathbf{u}_1^n \right) \tag{2.71}$$

where the subscript denotes the spatial index of the node, and the superscript stands for the time layer. Note that $\partial \mathbf{u} / \partial x$ term is time-averaged between the known time-layer n and the unknown layer * that brings an additional stability (time-centred Crank-Nicholson scheme). Let us build an iterative procedure by writing down an equation for the differential $\delta \mathbf{u}^*$ (by replacing $\mathbf{u}^*$ with $\mathbf{u}^* + \delta \mathbf{u}^*$):

$$\mathbf{u}_1^* + \delta \mathbf{u}_1^* - \mathbf{u}_1^n = \beta \left(\mathbf{u}_2^* + \delta \mathbf{u}_2^* - \mathbf{u}_1^* - \delta \mathbf{u}_1^* + \mathbf{u}_2^n - \mathbf{u}_1^n \right) \tag{2.72}$$

where $\beta = \dfrac{c \Delta t}{2 \Delta x}$. This can be written as

$$(1+\beta) \delta \mathbf{u}_1^* - \beta \delta \mathbf{u}_2^* = -(1+\beta) \mathbf{u}_1^* + (1-\beta) \mathbf{u}_1^n + \beta \left(\mathbf{u}_2^* + \mathbf{u}_2^n \right) \tag{2.73}$$

which can be immediately recognized as (2.65) with

$$\begin{aligned} \widetilde{\mathbf{A}}_1 &= 0 \\ \widetilde{\mathbf{B}}_1 &= 1 + \beta \\ \widetilde{\mathbf{C}}_1 &= -\beta \\ \widetilde{\mathbf{D}}_1 &= -(1+\beta) \mathbf{u}_1^* + (1-\beta) \mathbf{u}_1^n + \beta \left(\mathbf{u}_2^* + \mathbf{u}_2^n \right) \end{aligned} \tag{2.74}$$

Boundary conditions on the right boundary are treated similarly.

This type of artificial boundary conditions works very well and does not generate any back-reflected waves in the case when disturbances propagate perpendicularly to the boundary. For an oblique incidence of disturbances onto the boundary, a special treatment exists but it requires a considerably more complicated implementation [52].

One of the main drawbacks of this type of boundary conditions is that the velocity of disturbance propagation has to be known *a priori*, i.e. one has to make an assumption about the type of the wave phenomena involved and the velocities associated with them. In our case, a typical disturbance has a hydromagnetic nature, *i.e.* it propagates with Alfven velocity along the magnetic field and with magnetosonic velocities across the field, which makes its calculation a straightforward task.

2.2.6 Low density plasma background

Physically, a plasma plume expands into vacuum, which can be modeled either by including the plasma-vacuum boundary in the model or by introducing a very low-density plasma background. Although the first option is feasible, its implementation would be rather complicated, so a vanishingly low-density plasma background approach was taken.

As mentioned earlier, low-density plasma regions introduce certain numerical challenges by forcing small timesteps and thus long runtimes. A typical hydromagnetic disturbance propagates with speeds inversely dependent on plasma density. These low-frequency electromagnetic ion wave phenomena are called *Alfven waves* (along the magnetic field lines) and cross-field *magnetosonic waves*. At low plasma densities, both propagate at $v_a = B/\sqrt{4\pi\rho}$ (Alfven velocity) resulting in a very restrictive Courant timestep condition.

In order to weaken this limitation we propose the following approach. It can be shown that attenuating the Lorentz force with a density-dependent damping factor $\xi(\rho)$ in the momentum equation (2.39)

$$\frac{\partial(\rho\mathbf{v})}{\partial t} + \nabla(\rho\mathbf{v}\cdot\mathbf{v}) + \nabla P + \frac{\xi(\rho)}{4\pi}\mathbf{B}\times(\nabla\times\mathbf{B}) = 0 \qquad (2.75)$$

will effectively limit the Alfven velocity as

$$v_a = B\sqrt{\frac{\xi(\rho)}{4\pi\rho}} \tag{2.76}$$

In order to preserve the meaningful physics within the plasma plume (high density region) but at the same time preserving Alfven velocity from "exploding" in low-density 'vacuum region' it is reasonable to choose $\xi(\rho)$ so that

$$\begin{aligned} &\xi(\rho) = 1, \qquad \rho \geq \rho_{crit} \text{ (plasma plume)} \\ &\frac{\xi(\rho)}{4\pi\rho} = const., \qquad \rho \leq \rho_{crit} \text{ ("vacuum" region)} \end{aligned} \tag{2.77}$$

where ρ_{crit} is a critical density below which we are no longer interested in accurate representation of wave velocities. This would ensure that the momentum equation is unaltered inside the plasma plume, and that Alfven velocity is limited to a constant value independent on the plasma density in the "vacuum" regions.

In addition to (2.77), it is desirable for the damping function $\xi(\rho)$ to be smooth in order not to introduce numerical instabilities during differentiation. As a convenient choice for the damping function, $\xi(\rho) = \tanh(\rho/\rho_{crit})$ was used, where ρ_{crit} is a parameter, throughout the current study. In this case, the attenuated Alfven velocity becomes:

$$v_{att} = B\sqrt{\frac{\tanh\left(\rho/\rho_{crit}\right)}{4\pi\rho}} \tag{2.78}$$

and at low densities ($\rho \ll \rho_{crit}$) approaches

$$\lim_{\rho\to 0} v_{att} = \frac{B}{\sqrt{4\pi\rho_{crit}}} \equiv v_a\big|_{\rho=\rho_{crit}} \tag{2.79}$$

thus, the attenuated Alfven velocity in "vacuum" regions is guaranteed not to exceed the value corresponding to non-attenuated Alfven velocity at ρ_{crit}. Attenuated Alfven velocity (2.78) can be also written as

$$v_{att} = \frac{B}{\sqrt{4\pi\rho_0}} \frac{\sqrt{\tanh\left(\frac{\rho/\rho_0}{\rho_{crit}/\rho_0}\right)}}{\sqrt{\rho/\rho_0}} \tag{2.80}$$

where the normalization parameter ρ_0 could be the peak density, for example, and $v_0 \equiv \frac{B}{\sqrt{4\pi\rho_0}}$ becomes the Alfven velocity at that density. Thus, in normalized quantities (normalized density $\rho' \equiv \rho/\rho_0$) the attenuated Alfven velocity becomes (Figure 17):

$$v' \equiv \frac{v_{att}}{v_0} = \sqrt{\frac{\tanh\left(\frac{\rho'}{\rho'_{crit}}\right)}{\rho'}} \tag{2.81}$$

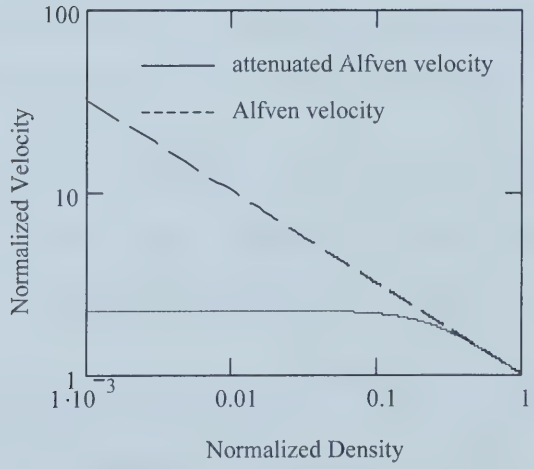

Figure 17. Normalized Alfven velocity and attenuated Alfven velocity *vs* normalized plasma density. Normalized attenuation parameter $\rho'_{crit} = 0.2$.

2.2.7 Numerical diffusion

The advection term $\left(\partial/\partial t + \mathbf{v}\cdot\nabla\right)$ in the continuity equation is known to be numerically unstable – it allows growth of short scale spatial perturbations that can be viewed as if there were diffusion with a negative diffusion coefficient (so called

antidiffusion) [53]. To compensate for this effect, a small purely artificial diffusive term $D\nabla^2\boldsymbol{u}$ is added to the MHD equations of continuity, momentum and energy. These terms are differenced explicitly as FLUX terms. The constant D (normalized diffusion coefficient) is typically very small ($\sim 10^{-4}$) and is chosen in such a way as not to affect the physics significantly but to suppress the growing instabilities. It is important to note that the equation for magnetic field is not being altered with the numerical diffusion. This is done in order to preserve the requirement of zero divergence of magnetic field $\nabla \cdot \mathbf{B} = 0$.

Experience shows that numerical instabilities growing along the B-field direction cannot always be suppressed effectively with $D\nabla^2\boldsymbol{u}$ diffusion terms. Increasing the value of the diffusion coefficient is not a good option because it would wash out the large-scale spatial features of the solution. We have demonstrated that a forth-order $-D\partial^4\mathbf{u}/\partial x^4$ diffusion-like term can be superior over $D\nabla^2\boldsymbol{u}$ in removing short-scale instabilities without destroying the large-scale solution features and can lead to greater numerical stability and increased time-steps. Spatial differencing

$$\left(\frac{\partial^4 u}{\partial x^4}\right)_i = \frac{1}{\Delta x^4}\left(u_{i-2} - 4u_{i-1} + 6u_i - 4u_{i+1} + u_{i+2}\right) \tag{2.82}$$

performed implicitly would require a five-diagonal solution matrix (2.67) that would unnecessary complicate the numerical method, thus an explicit differencing of this term has been chosen.

The advantage of using $-D\partial^4\mathbf{u}/\partial x^4$ over $D\nabla^2\boldsymbol{u}$ can be explained by investigating the *growth rate* of a spatial perturbation as a function of its spatial scale. By considering a harmonic mode of a perturbation as

$$u\left(j\cdot\Delta x, n\cdot\Delta t\right) \equiv u_j^n = \xi^n \exp\left(ik\pi j\Delta x\right) \tag{2.83}$$

where k is the eigenvalue of the perturbation mode and $\xi(k)$ - its corresponding growth rate, one can show that diffusion term $D\nabla^2\boldsymbol{u}$ would result in

$$\xi_{grad2}\left(k\right) = 1 - 4\alpha \sin^2\frac{k\pi\Delta x}{2}, \quad \alpha \equiv D\frac{\Delta t}{\Delta x^2} \tag{2.84}$$

(same for both implicit and explicit differencing provided $\alpha \ll 1$), while explicit $-D\partial^4\mathbf{u}/\partial x^4$ yields

$$\xi_{grad4}(k) = 1 - \beta\left(16\sin^2\frac{k\pi\Delta x}{2} - 4\sin^2 k\pi\Delta x\right), \quad \beta \equiv D\frac{\Delta t}{\Delta x^4} \tag{2.85}$$

Both ξ_{grad2} and ξ_{grad4} are essentially low-pass filters and provide attenuation at high k-s (corresponding to short-scale modes, typically represented by numerical instabilities). While both ξ_{grad2} and ξ_{grad4} have a value of unity at $k = 0$ (corresponding to an infinitely long spatial mode, or constant level), ξ_{grad4} has a much steeper characteristics (Figure 18), preserving the long-scale spatial features of the solution (smaller k's) and efficiently removing short-scale instabilities (larger k's).

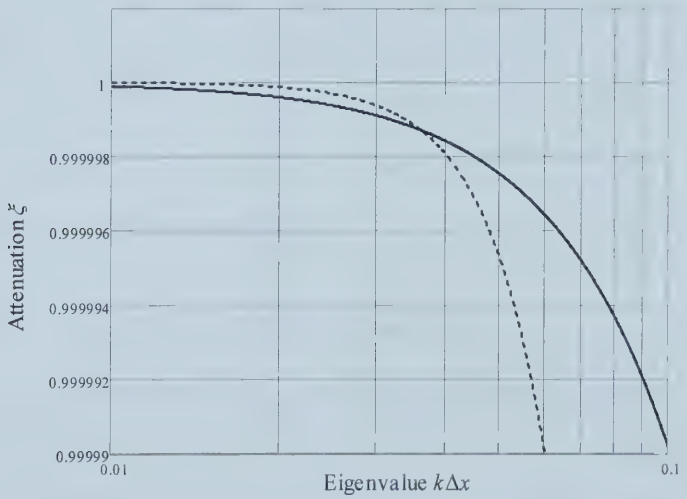

Figure 18. Growth rate ξ (attenuation) for $grad^2$ (solid line) and $grad^4$ (dashed line) spatial filters ($\alpha = 10^{-4}$, $\beta = 8\cdot10^{-3}$). Note that $grad^4$ efficiently removes short-scale spatial components (higher k) while keeping the long scale features of the solution (low k). In contrast, $grad^2$ is less superior in suppressing high-k numerical instabilities and leads to wash out of features.

Although the difference between ξ_{grad2} and ξ_{grad4} at small k-s may seem subtle, it becomes more apparent if we consider the amplification of instabilities after thousands of timesteps, by looking at ξ^N (Figure 19).

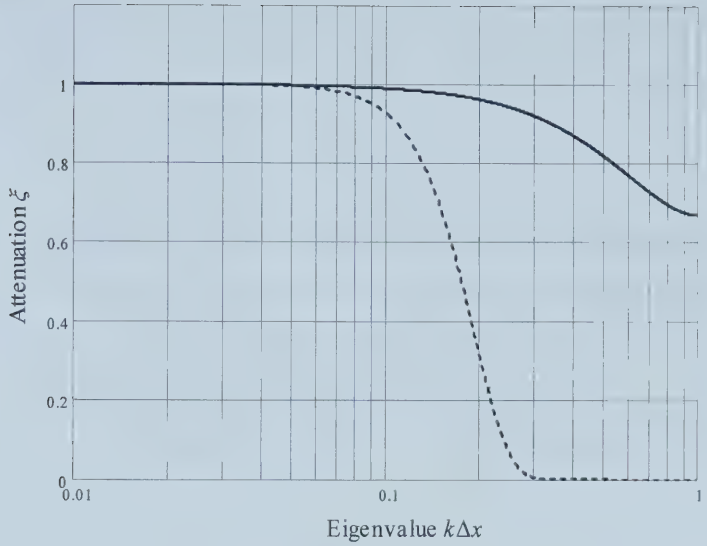

Figure 19. *Grad*^{2} and *grad*^{4} accumulated amplification after 1000 timesteps. Shown are $\xi^{1000}_{grad\,2}$ ($\alpha = 10^{-4}$, solid line) and $\xi^{1000}_{grad\,4}$ ($\beta = 8 \cdot 10^{-3}$, dashed line).

2.3 Results and Discussion

2.3.1 Initial Conditions and Run Parameters

In the actual experiments on plasma guiding, the plasma is created by irradiating a target with a high intensity (10^9 – 10^{10} W/cm^2) laser beam. Modeling of the initial creation, expansion and capture of the plasma by the solenoidal field is a very complex problem and is beyond the scope of the present investigation. For this study of guiding in a curved magnetic field, we take as a starting point the instant of time when the plasma has already been captured by the guiding field and can be described as a plasma cloud in flight at the entrance of the solenoid.

As an approximation to the solenoidal geometry, a segment of a torus with a square cross-section was chosen (Figure 20). A solenoidal magnetic field, except for the end regions of the solenoid, can be approximated by the magnetic field produced by a current flowing along the axis of symmetry of the torus (z-axis). This can be shown from

the requirements $\nabla \cdot \mathbf{B} = 0$ and $\nabla \times \mathbf{B} = 0$ inside the solenoid, and by utilizing the toroidal symmetry of the field. Therefore, magnetic field can be conveniently specified as:

$$B_r = B_z = 0$$
$$B_\varphi = B_0 \frac{R_0}{r} \tag{2.86}$$

where B_0 is the magnitude of the field inside the torus (at the centre of its cross-section). As mentioned, this approach does not properly describe the magnetic field at the ends of the solenoid. However, we are studying an idealized case, and our primary goal is to investigate the effect of the field curvature on plasma guiding.

Cylindrical coordinates (r, φ, z) have corresponding metric coefficients $(h_1, h_2, h_3) = (1, r, 1)$.

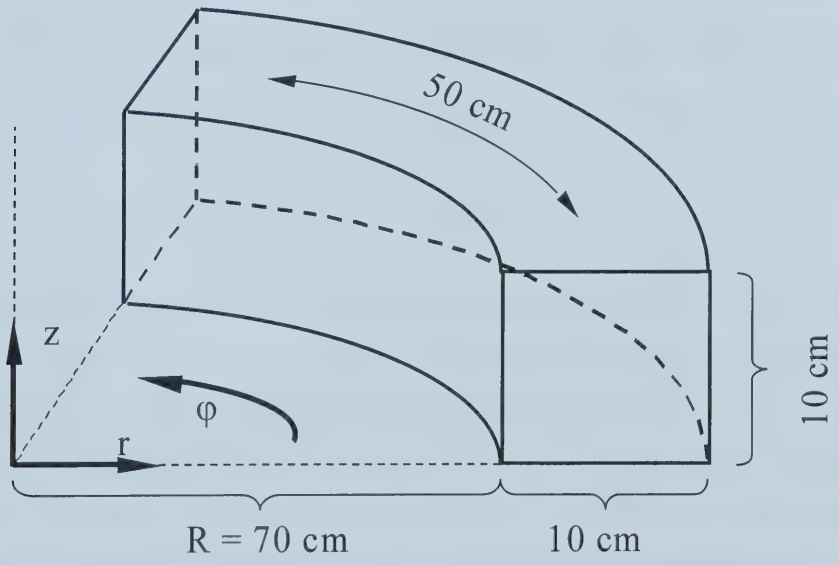

Figure 20. Cylindrical coordinates are used to model curvilinear solenoid.

At the initial instance of time the plasma cloud ("plasmoid") is specified in a form of a singly charged Carbon plasma ellipsoid with a Gaussian density profile reaching peak density of $n = 1.3 \cdot 10^{12}$ cm^{-3} (corresponding to mass density $\rho = 2.6 \cdot 10^{-11}$g/cm^3) superimposed over a uniform low-density (0.1% of the Gaussian peak) background, representing the vacuum surrounding the plasma cloud. The attenuation parameter ρ_{crit} is chosen at 20% level of the peak density. The corresponding attenuated Alfven velocity at

the "vacuum background" becomes $1.24 \cdot 10^8$ cm/sec, with its unattenuated value of $1.8 \cdot 10^9$ cm/sec.

Initially, the plasma cloud is immersed in an unperturbed (2.86) magnetic field with $B_0 = 1$ kG. It would be more reasonable to use an equilibrium initial magnetic field (i.e. with a proper magnetic well balancing plasma thermal expansion). However, this would require an additional solver for the plasma initial equilibrium state. It turned out that the magnetic field well, required for balancing the plasma thermal expansion, forms very quickly after the first few iterations, eliminating the need for the pressure balance at the beginning of the run.

The initial plasma velocity $v_0 = 7 \cdot 10^6$ cm/sec is aligned along the magnetic field (*i.e.* $v_r = v_z = 0$). The initial velocity v_φ is set with an increase in the r-direction, so that the angular velocity v_φ / r remains constant along the radius, and no shear flow or friction between the adjacent fluid layers are introduced in the radial direction:

$$v_r = v_z = 0$$
$$v_\varphi = v_0 \frac{r}{R_0} \tag{2.87}$$

The initial temperature is chosen to be uniform and equal to T = 5 eV. The plasma electrical conductivity is set equal to Spitzer conductivity at 5 eV, *i.e.* $\sigma_{Sp} = 4.6 \cdot 10^{13}$ sec^{-1} and is chosen to be uniform and constant during the simulation.

Solenoid dimensions were chosen as 7 cm x 7 cm in the cross-section and 50 cm in length. The radius of curvature of the solenoid is 75 cm. With uniform spacing of $\Delta r = 0.1$ cm, $\Delta\varphi = 6.37 \cdot 10^{-3}$ rad (~ 0.5 cm), $\Delta z = 0.1$ cm, this produces a $71 \times 101 \times 71$ point mesh.

A constant timestep of 10^{-9} sec corresponds to a Courant number $\Delta t / \Delta x \, v_a$ of 18 for the unattenuated Alfven velocity, or 1.2 for the attenuated velocities.

Calculations were performed on the University of Alberta Aurora/Borealis SGI Origin 2000 complex. It consists of 64 nodes with each node containing: CPU MIPS R12000 300MHz, FPU MIPS R12010 300MHz. Main memory size of the SGI Origin 2000: 16 Gbytes, cache size: 8Mbytes.

Total physical simulation time of 3.5 μs is achieved in 3500 timesteps. Each timestep takes ~ 4.2 sec of machine runtime. Values of the state vector {**B**, **v**, ρ, P} on the mesh nodes were saved to a file every 100 timesteps.

2.3.2 Numerical Results

As mentioned in the previous section, the expansion of plasma inside the curved magnetic solenoid was calculated for 3.5 μs. After that, the code execution becomes unstable.

Qualitatively, the dynamics of the plasmoid can be described as propagation along the solenoid with constant velocity corresponding to the initial velocity (~ $7 \cdot 10^6$ cm/sec) combined with a slower drift in the radial direction (Figure 21). No drift in the vertical z-direction was observed.

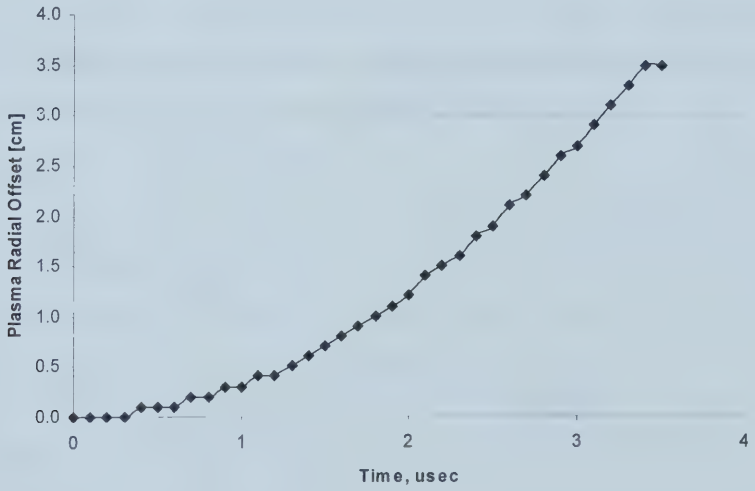

Figure 21. Plasma offset in the radial direction (from the minor axis of the solenoid).

Density half maximum contours at 0^{th}, 10^{th}, 20^{th}, and 30^{th} outputs corresponding to 0, 1, 2, and 3 μs respectively are shown on Figure 22. One can conclude that the plasmoid essentially propagates along a straight line tangential to the magnetic field at the starting location of the plasmoid.

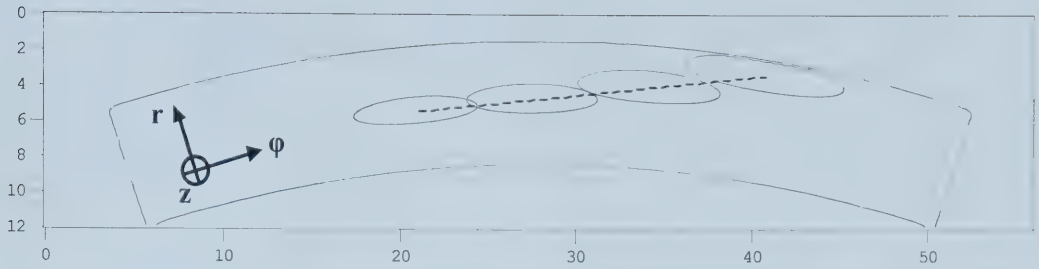

Figure 22. Propagation of plasma cloud in a curved solenoid. Half maximum density contours are shown at 0, 1, 2, and 3 μsec after the start of the simulation. Geometrical dimensions are in cm.

Because of the diffusion of the plasma across and along the magnetic field, the plasmoid expands (Figure 22), and since the total plasma mass must remain constant, its peak density decreases (Figure 23). Figure 24 illustrates conservation of the total plasma mass (density integrated over the computational volume), which can serve as an indirect check for the code consistency. Note that at around 3 μsec after the plasma launch the total plasma mass starts to decrease rapidly. This corresponds to the moment when plasma hits the solenoid wall and leaves the computational domain.

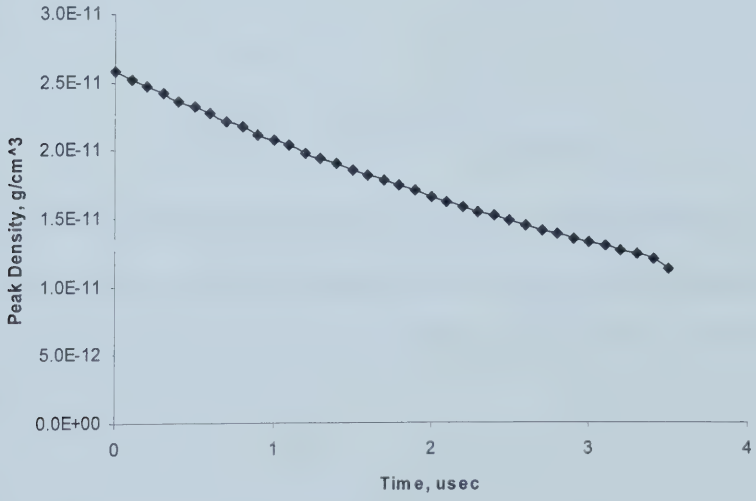

Figure 23. Plasma peak density evolution.

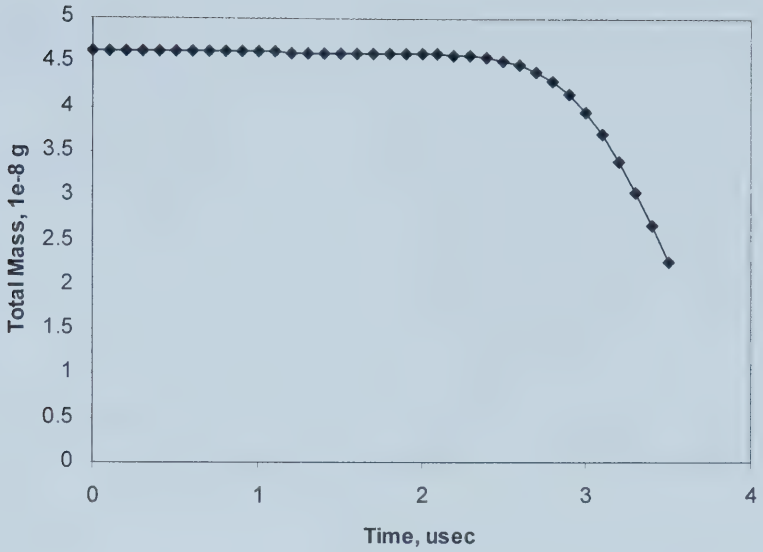

Figure 24. Total plasma mass evolution.

It is also interesting to see how accurately the $\nabla \cdot \mathbf{B} = 0$ condition is preserved during the simulation. This would give another check for the overall consistency of the numerical method. The evolution of the magnetic field divergence (or rather its absolute value) averaged over the computational grid is shown on Figure 25. To be meaningful it is normalized to the characteristic gradient of the magnetic field magnitude as

$$\left\langle \left| \text{div } \mathbf{B} \right| \right\rangle \quad (normalized) = \frac{\left\langle \left| \text{div } \mathbf{B} \right| \right\rangle}{\left\langle \left| \text{grad } B \right| \right\rangle} \tag{2.88}$$

where $<\ldots>$ operator stands for the average over the computational grid, and $|\ldots|$ denotes the magnitude of a vector. Evidently, the divergence (2.88) of the magnetic field increases over time (because of the accumulated effect of numerical errors) but remains well under 0.5%.

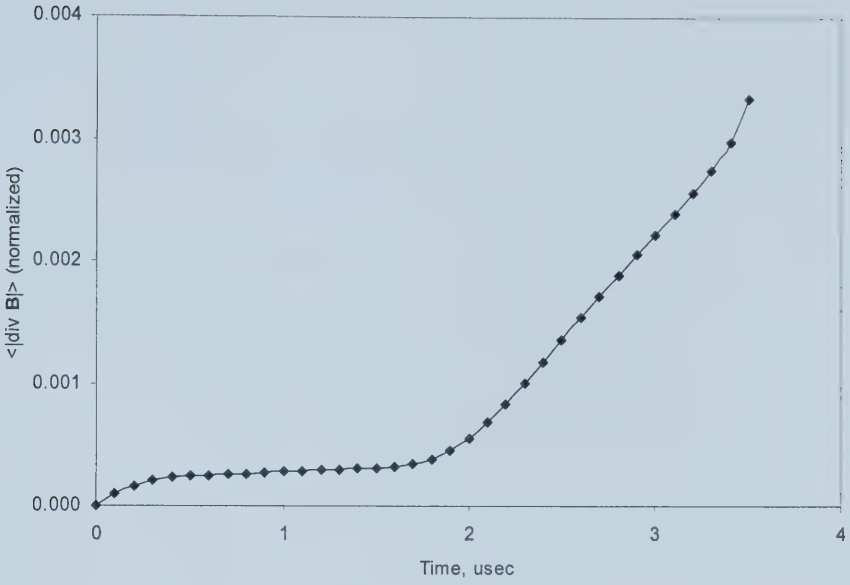

Figure 25. Evolution of the average magnetic field divergence (normalized).

The electric current density **j** can be calculated from the magnetic induction **B** through the Ampere's law (2.34):

$$\mathbf{j} = \frac{c}{4\pi} \nabla \times \mathbf{B} \tag{2.89}$$

By its nature, this current is divergence-free since the divergence of a curl is always zero $\nabla \cdot (\nabla \times \mathbf{A}) \equiv 0$. The cross-field component $\mathbf{j}_\perp$ of the current, which is almost equivalent to the diamagnetic current (1.11), is shown on Figure 26. It provides sufficient Lorentz force $\mathbf{j} \times \mathbf{B}$ in the momentum equation (2.29) to balance the plasma expansion across magnetic field caused by thermal pressure gradient ∇P. Importantly, the diamagnetic current alone is not divergence-free (Figure 27). Even though it looks nearly circularly symmetric on Figure 26 (*i.e.* as a closed non-diverging current loop), it is important to remember that this is a plot of the current *density*, and since the upward current flows in the region with higher radius of curvature, overall it will carry more charge than the downward current. In other words, there is a net upward current.

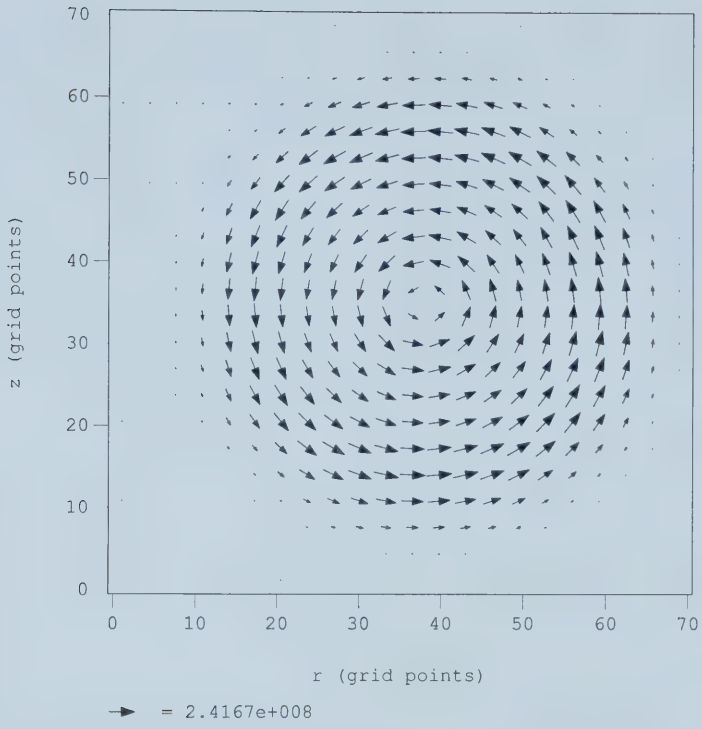

Figure 26. Cross-field current density $\mathbf{j}_\perp$ (statamp/cm^2) in the cross-section of the solenoid after 1 μsec. Position of the cross-section corresponds to the centre of the plasmoid.

According to the charge continuity equation (2.15), a diverging diamagnetic current having a net upward component would result in positive charge accumulation at the top of the plasmoid and negative charge at its bottom. Thus, the plot of the diamagnetic current divergence (in statamp/cm^3) on Figure 27 is equivalent to a rate of charge density build-up (statcoul/cm^3-sec) taken with a minus sign:

$$\frac{\partial \sigma}{\partial t} = -\nabla \cdot \mathbf{j}_\perp \tag{2.90}$$

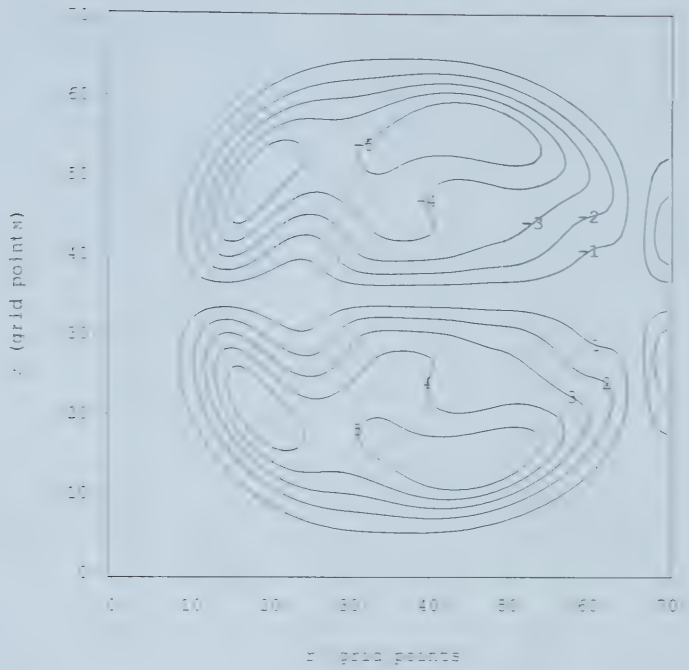

Figure 27. Divergence of the cross-field current $\mathbf{j}_\perp$ (10^6 statamp cm^3) in the cross-section of the solenoid after 1 μsec. Position of the cross-section corresponds to the centre of the plasmoid.

Of course, this charge never builds up because the total current $\mathbf{j} \equiv \mathbf{j}_\perp + \mathbf{j}_\parallel$ has zero divergence. The excessive charge is carried away by the field-aligned currents $\mathbf{j}_\parallel$, which are closed at the solenoid ends.

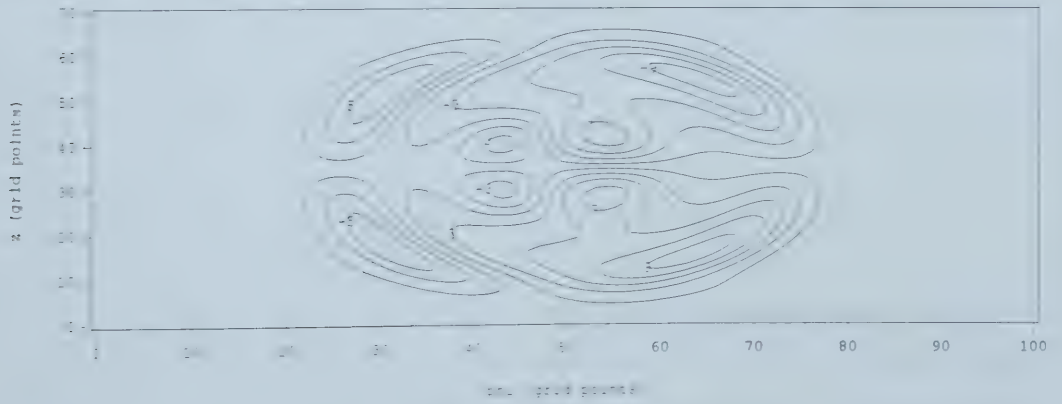

Figure 28. Divergence of the cross-field current $\mathbf{j}_\perp$ (10^6 statamp cm^3) in the cross-section of the solenoid (side view) after 1 μsec. Position of the cross-section corresponds to the centre of the plasmoid.

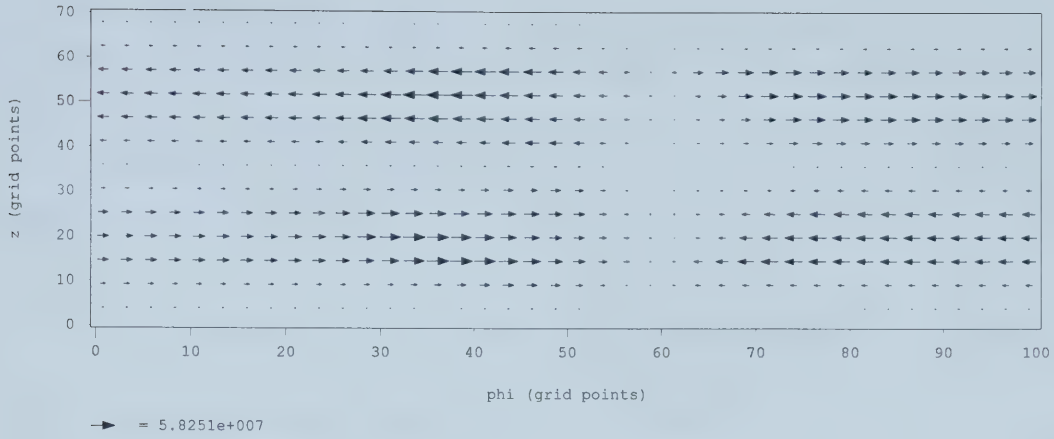

Figure 29. Field-aligned current density $j_{\|}$ (statamp/cm^2) in the cross-section of the solenoid (side view) after 1 μsec. Position of the cross-section corresponds to the centre of the plasmoid.

Figure 29 shows distribution of the field-aligned currents $\mathbf{j}_{\|}$ in the cross-section of the solenoid ($\varphi - z$ plane, side view). Divergence of the cross-field current $\mathbf{j}_{\perp}$ is also shown in the same cross-sectional view for comparison (Figure 28). Schematically, the charge circulation in the solenoid can be viewed as on Figure 30.

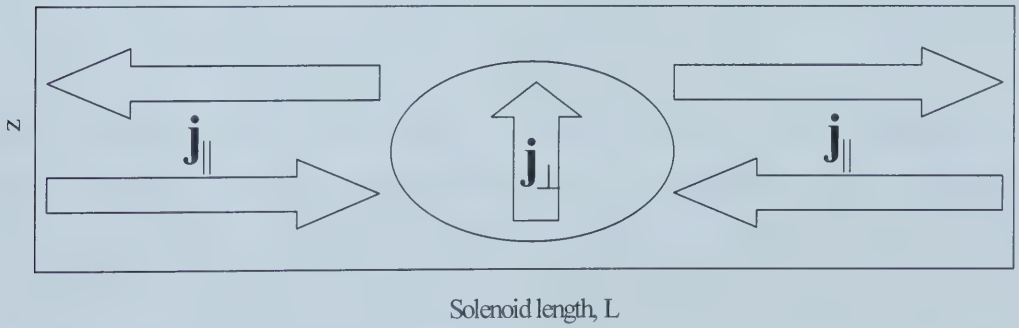

Figure 30. Schematic representation of the currents structure in the plasma. Side view.

Nevertheless, the vertical diverging component of the diamagnetic current is very important for the guiding because it can provide the Lorentz force $\mathbf{j} \times \mathbf{B}$ required to guide the plasma along the field lines. From the guiding centre perspective, this vertical current represents guiding centre drifts (1.5) caused by magnetic field curvature and gradient. While from the guiding centre perspective the curvature/gradient drifts and diamagnetic

drift have completely different nature, the former drifts become a part of the latter one in the fluid model. A good discussion on this non-straightforward issue can be found in [54, pp. 101 - 109]. It is possible to estimate the magnitude of the corresponding particle drift from the magnitude of the current divergence. If the guiding centre drift results in a separation between ions and electron of Δz, the corresponding space charge density will be

$$\sigma = e(n_i - n_e) = e\left(n\left(z - \Delta z/2\right) - n\left(z + \Delta z/2\right)\right) \simeq -e\frac{\partial n}{\partial z}\Delta z \tag{2.91}$$

and from the charge continuity equation the ions' drift velocity can be found as

$$\begin{aligned} -\nabla \cdot \mathbf{j} &= \frac{\partial \sigma}{\partial t} = -e\frac{\partial n}{\partial z}\frac{\partial \Delta z}{\partial t} = -e\frac{\partial n}{\partial z}v_z \\ \therefore v_z &= e\left(\frac{\partial n}{\partial z}\right)^{-1}\nabla \cdot \mathbf{j} \end{aligned} \tag{2.92}$$

From the MHD numerical data, the ion's drift velocity can be estimated as $1.7 \cdot 10^4$ cm/sec. This is very close to the magnetic field curvature/gradient drift velocity found from the guiding centre model:

$$\begin{aligned} \mathbf{v}_{\perp B} \equiv \mathbf{v}_R + \mathbf{v}_{\nabla B} &= \frac{cm}{q}\frac{\mathbf{R}_c \times \mathbf{B}}{R_c^2 B^2}\left(v_\parallel^2 + \frac{1}{2}v_\perp^2\right) = \\ = \frac{c}{q}\frac{1}{R_c B}\left(kT_\parallel + kT_\perp\right) &= \frac{c}{q}\frac{2kT}{R_c B} = 1.3 \cdot 10^4 \text{ cm/sec} \end{aligned} \tag{2.93}$$

where velocities $v_\parallel$ and $v_\perp$ are the average velocities in the Maxwellian distribution, i.e. particle's *thermal* velocity. In other words, the vertical component of the diamagnetic current in MHD model describes the curvature/gradient drifts caused by particle thermal velocities. However, the actual particle velocity along the field lines is a superposition of the fluid velocity and particle thermal velocity, i.e. $v_\parallel = v_0^{fluid} + v_\parallel^{thermal}$, where $v_0^{fluid} = 7 \cdot 10^6$ cm/sec and $v_\parallel^{thermal} = \sqrt{\frac{kT}{m}} = 6.3 \cdot 10^5$ cm/sec (for Carbon ions). The corresponding full curvature/gradient drift $v_{\perp B} \simeq 8 \cdot 10^5$ cm/sec significantly exceeds the one described by the diamagnetic current. For successful guiding of the plasma along the field lines, there has to be a vertical current corresponding to the full curvature/gradient drift to provide sufficient $\mathbf{j} \times \mathbf{B}$ force, as was explained in §1.2.1.

To recover the space charge we cannot simply use the charge continuity equation (2.15) since we assumed non-divergent electric current by neglecting the displacement current $-\frac{1}{4\pi}\frac{\partial \mathbf{E}}{\partial t}$ in Ampere's law (2.9), which is equivalent to setting the charge density accumulation rate to zero in the equation (2.15). However, it is possible to calculate the space charge density from Poisson's equation (2.8) using Ohm's law (2.22) to obtain the electric field:

$$\begin{aligned}\sigma &= \frac{1}{4\pi}\nabla\cdot\mathbf{E} \equiv \frac{1}{4\pi}\nabla\cdot\left(\eta\mathbf{j} - \frac{\mathbf{v}\times\mathbf{B}}{c}\right) \equiv \\ &\equiv \frac{1}{4\pi}\nabla\cdot\left(\eta\frac{c}{4\pi}\nabla\times\mathbf{B} - \frac{\mathbf{v}\times\mathbf{B}}{c}\right) \equiv -\frac{1}{4\pi c}\nabla\cdot(\mathbf{v}\times\mathbf{B})\end{aligned} \tag{2.94}$$

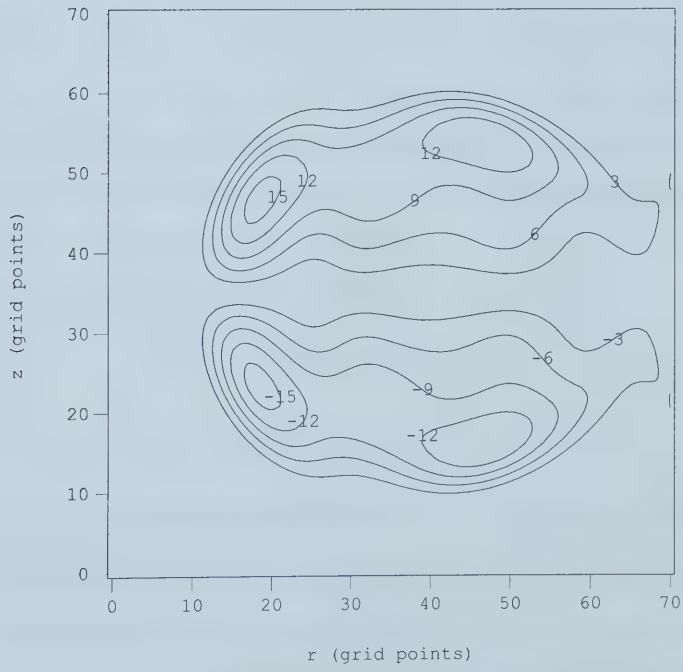

Figure 31. Charge density (10^{-6} statcoulomb/cm^3) distribution in the cross-section of the solenoid after 1 μsec. Position of the cross-section corresponds to the centre of the plasmoid.

The electric field calculated from Ohm's law as

$$\mathbf{E} = \eta\mathbf{j} - \frac{\mathbf{v}\times\mathbf{B}}{c} \tag{2.95}$$

is a superposition of a strong divergence-free uniform E_z component ($\sim 2\cdot10^{-2}$ statvolt/cm after 1 μsec) and a considerably smaller component ($\sim 2\cdot10^{-4}$ statvolt/cm after 1 μsec) produced by the space charge (2.94) (with finite divergence equal to the space charge). It is interesting to identify the mechanism of this space charge formation. It turns out, that its numerical value is close to the space charge resulting from the polarization limited curvature/gradient drift (3.8) of particles moving with thermal velocities, appearing in the guiding centre model:

$$\begin{aligned} |\sigma| &\simeq e\frac{\partial n}{\partial z}\Delta z = e\frac{\partial n}{\partial z}v_z\Delta t = e\frac{\partial n}{\partial z}\frac{v_R + v_{\nabla B}}{1+\chi}\Delta t = \\ &= e\frac{\partial n}{\partial z}\frac{\dfrac{c}{q}\dfrac{2kT}{R_c B}}{1+4\pi c^2\dfrac{Mn}{B^2}}\Delta t \simeq 1.6\cdot10^{-5}\,\frac{\text{statcoul}}{\text{cm}^3} \end{aligned} \tag{2.96}$$

Expression (3.8) for polarization limited curvature/gradient drift will be obtained in the next chapter. In other words, this space charge and the electric field it creates are associated only with the thermal component of the particles' velocity. As it will be shown below, the divergence-free uniform E_z component of the electric field is associated with the fluid flow component of the particles' velocity.

Taking a cross product of (2.95) with **B** gives

$$\begin{aligned} &\mathbf{E}\times\mathbf{B} = \frac{1}{c}\mathbf{B}\times(\mathbf{v}\times\mathbf{B}) + \eta\mathbf{j}\times\mathbf{B} \\ &\therefore v_\perp = c\frac{\mathbf{E}\times\mathbf{B}}{B^2} - c\eta\frac{\mathbf{j}\times\mathbf{B}}{B^2} \end{aligned} \tag{2.97}$$

The $\mathbf{j}\times\mathbf{B}$ term is considerably smaller than the $\mathbf{E}\times\mathbf{B}$ term (since $E\sim 2\cdot10^{-2}$ statvolt/cm and $\eta\mathbf{j}\sim 5\cdot10^{-6}$ statvolt/cm). If it is ignored, the cross-field velocity becomes just the familiar guiding centre $\mathbf{E}\times\mathbf{B}$ drift. The plasmoid deviates from the field lines because of the $\mathbf{E}\times\mathbf{B}$ drift with such a rate as to propagate in a straight trajectory. As will be shown in the next chapter, the electric field sufficient for such $\mathbf{E}\times\mathbf{B}$ drift appears from the space charge accumulated as a result of a polarization limited curvature/gradient drift, associated with the plasma *flow velocity*.

To conclude on the discussion of the numerical results of numerical modeling, it is interesting to compare the mechanism of plasma expansion into curved magnetic field

as it is described by the magnetohydrodynamical model and the guiding centre model (Table 1). The latter model will be developed in the following chapter. As can be seen from this comparison, certain details of plasma-field interaction are different in the two models. This is caused by the simplifications used in the MHD model. However, the overall dynamics (i.e. the magnitude of plasma offset, electric field, diamagnetic current, etc.) are equivalently described by both models.

From the above discussion, it becomes evident that plasma will follow the magnetic field lines only if its flow velocity is zero. In that case, the vertical current resulting from curvature/gradient drift associated with particles' thermal velocity will be sufficient to produce the Lorentz force $\mathbf{j} \times \mathbf{B}$ to guide the plasma as it expands along the field lines. It is also evident that an increase in magnetic field will not change the guiding efficiency, despite the fact that experimentally the guiding improves significantly at 3 kG magnetic field.

Magnetohydrodynamics	Guiding Centre in Self-Consistent Fields
Formation of a diamagnetic current preventing thermal expansion of plasma across the magnetic field. A vertical component of this current with finite divergence corresponds to curvature/gradient drift associated with particle *thermal* velocities. The magnitude of this drift suggests that it is not limited by the polarization effect.	Vertical current corresponds to polarization limited curvature/gradient drift associated with particle *flow* velocity.
The space charge carried by this current is removed by the currents along the magnetic field, which are closed at the ends of the solenoid.	The charge carried by the current is not removed by the field-aligned currents, but accumulates on the top and the bottom of the plasmoid creating a vertical electric field.
Residual charge density corresponds to the polarization limited curvature/gradient drift associated with particle *thermal* velocities.	As the charge and the field grow, the polarization drift limits the vertical current (which makes it polarization limited) thus limiting further growth of the field. Therefore, charge density corresponds to the polarization limited curvature/gradient drift associated with particle *flow* velocity.
The divergence-free component of the vertical electric field corresponds to polarization limited curvature/gradient drift associated with plasma *flow* velocity produces $\mathbf{E} \times \mathbf{B}$ drift sufficient to deflect plasma from field lines into a straight trajectory.	The magnitude of the resulting electric field happens to be just sufficient to push the plasmoid into a straight trajectory. Clearly, the field is the result of polarization limited curvature/gradient drift associated with plasma flow velocity

Table 1. Comparison of the mechanism of plasma expansion from MHD and guiding centre perspectives.

3. Charged particle in self-consistent fields

In this chapter, we will explore the problem of plasma guiding from the perspective of a charged particle dynamics in electromagnetic fields. We will analyse possible physical mechanisms leading to plasma losses, and will develop ways of potentially improving plasma guiding.

3.1 Plasma cross-field dielectric constant

Let us analyse the magnetic field guiding phenomena from a single charged particle perspective. Of course, particle dynamics in plasma is very different from that of a single particle (because of self-induced fields in the plasma and particles collisions), but we will try to account for the collective effects by introducing a self-consistent electric field.

For simplicity, we will again view the curved solenoid as a section of a torus. Except for the end regions of the solenoid the magnetic field inside is equivalent to that created by an electric current flowing along the major axis of the torus (z-axis). If cylindrical coordinates (r,φ,z) are used such magnetic field lines will coincide with $\hat{\varphi}$ direction and can be expressed as

$$\begin{aligned} B_r &= B_z = 0 \\ B_\varphi &\sim B_0 R/r \end{aligned} \tag{3.1}$$

In cylindrical coordinates the equation of motion (1.1) for a charged particle in electric and magnetic fields can be written as

$$\begin{aligned} \dot{r} &= v_r & \dot{v}_r &= F_r + \frac{v_\varphi^2}{r} \\ \dot{\varphi} &= \frac{v_\varphi}{r} & \dot{v}_\varphi &= F_\varphi - \frac{v_\varphi v_r}{r} \\ \dot{z} &= v_z & \dot{v}_z &= F_z \end{aligned} \tag{3.2}$$

where (F_r, F_φ, F_z) are the components of the force acting on a particle:

$$F_r = \frac{q}{m}\left[E_r + \frac{1}{c}\left(v_\varphi B_z - v_z B_\varphi\right)\right]$$
$$F_\varphi = \frac{q}{m}\left[E_\varphi + \frac{1}{c}\left(v_z B_r - v_r B_z\right)\right] \qquad (3.3)$$
$$F_z = \frac{q}{m}\left[E_z + \frac{1}{c}\left(v_r B_\varphi - v_\varphi B_r\right)\right]$$

To find the trajectory of a charged particle the above system of equations (3.2) - (3.3) was integrated numerically. Calculations were done in a Maple® environment, and a *Gear's solver* for stiff differential equations was used. Figure 32 shows a typical trajectory of a single ion (singly charged Carbon) launched with a velocity of $7 \cdot 10^6$ cm/sec along the axis of the curved solenoid (R = 75 cm) with a magnetic field of 1 kG. The trajectory is calculated for 10 μsec. One can recognize that the particle gyrates around magnetic field lines following the field curvature but also experiences a vertical curvature drift in the cross-field z-direction (Figure 33, side view). The duration of the gyration cycle is comparable to the time of flight, thus the ion completes less than two gyrations.

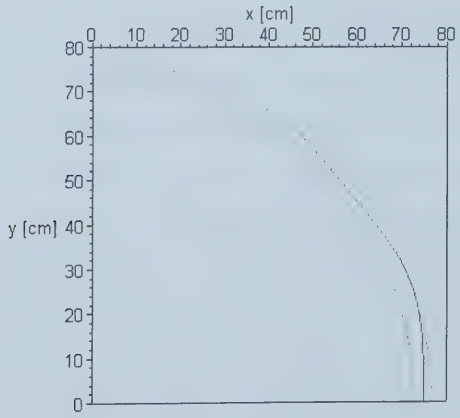

Figure 32. Trajectory of an ion (singly charged Carbon) launched in a curved (R = 75 cm) magnetic field (1 kG) with initial velocity $7 \cdot 10^6$ cm/sec. Top view.

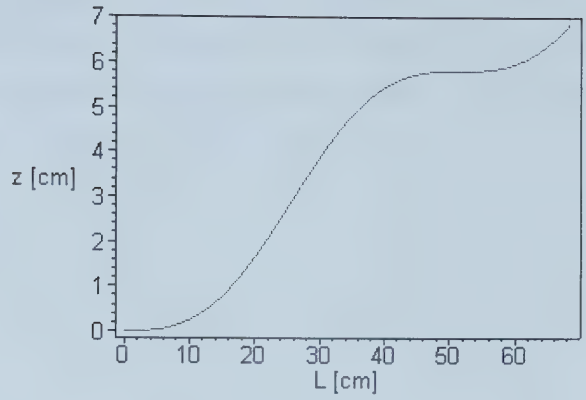

Figure 33. Vertical displacement (curvature drift) z of an ion along the length of solenoid L.

When we launch a single electron, its vertical drift, according to (1.6), happens to be, by four orders of magnitude, slower than that of an ion. The helical shape of the electron trajectory is more evident, as its gyration frequency is higher by a factor m_i/m_e. In contrast to the ions, electrons become *magnetized*, i.e. they almost precisely follow the magnetic field lines. Of course, in a plasma of any noticeable density, ions would not be able to separate significantly from electrons in z-direction because this would cause an enormous electric field impeding the charge separation. That is, charges tend to separate because of the curvature drift, this leads to a quick growth of an electric field, which in turn causes a polarization drift (1.7) opposing the initial curvature drift. Thus, vertical charge separation becomes limited by the counter directed polarization drift. To account for this effect in a single particle numerical model, we introduce an electric field dependent on the ions' vertical displacement Δz as

$$E_z = -4\pi ne\Delta z \tag{3.4}$$

with n being the plasma density. This expression follows from the Poisson equation $\nabla \cdot \mathbf{E} = 4\pi\sigma$ (where σ is a charge density) since:

$$\nabla \cdot \mathbf{E} \simeq \frac{dE_z}{dz} = 4\pi\sigma = 4\pi e\left(n_i - n_e\right) = 4\pi e\left(n\left(z-\Delta z\right) - n\left(z\right)\right) \simeq -4\pi e\frac{dn}{dz}\Delta z \tag{3.5}$$
$$\therefore E = -4\pi en\Delta z$$

Solving (3.2) - (3.3) for ion trajectory with such electric field added shows that ions now experience deflection from magnetic field lines in the radial direction, and with the

plasma density increasing in (3.4), the ion trajectories approach straight lines tangential to the magnetic field lines at the point of entry (Figure 34). The ions deflection is, of course, the familiar $\mathbf{E} \times \mathbf{B}$ drift caused by space charge electric field E_z. The electrons experience the same amount of deflection, thus the whole plasma deviates from the B-field lines. We can conclude that at densities 10^{12} - 10^{14} cm^{-3}, the plasma shows no sign of guiding in a 1 kG curved magnetic field.

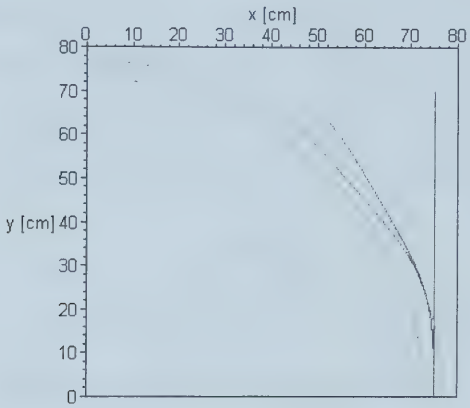

Figure 34. Carbon ion trajectories in 1kG curved magnetic field with electric field of charge separation taken into account. Electric field corresponds to plasma densities of 10^4 cm^{-3} (ion stays within solenoid), 10^6 cm^{-3} (ion deviates from magnetic lines), and 10^{13} cm^{-3} (ion travels in a straight line).

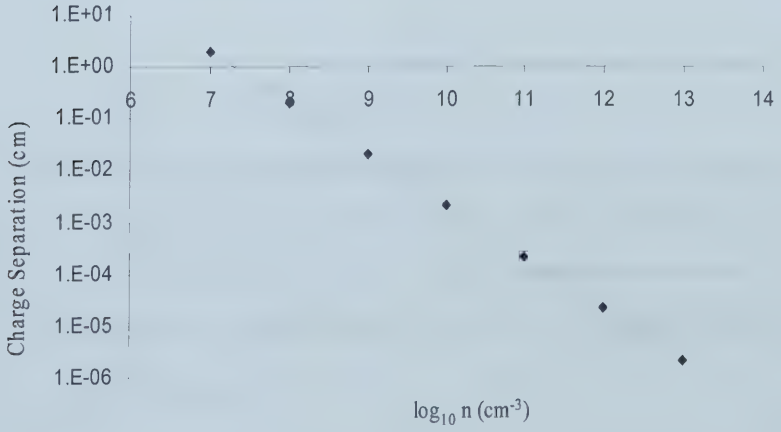

Figure 35. Charge separation in 1kG curved magnetic field (R = 75 cm) as a function of plasma density.

The vertical ion displacement (equivalent to charge separation) after 10 μsec calculated in the presence of self-consistent electric field decreases rapidly with plasma density increasing (Figure 35). This can explain why at high densities the plasma shows poor or no guiding in a curved magnetic field. The polarization drift essentially cancels out the cross-field curvature z-drift (1.5) required to guide the particles. Schmidt in his paper [18] analytically solves for a single particle drifts in curved magnetic fields by using a guiding centre approximation. Self-consistent electric field caused by charge separation is introduced in the same fashion as in (3.4). Schmidt shows that the magnetic field's ability to guide the plasma depends on the plasma cross-field *dielectric constant* κ, or rather its *dielectric susceptibility* χ (since $\kappa \equiv 1+\chi$) defined as:

$$\chi = 4\pi c^2 \frac{m_i n}{B^2} \tag{3.6}$$

He derives that curved magnetic field can only guide tenuous plasmas with $\chi \ll 1$ (single-particle like behaviour), however plasmas with $\chi \gg 1$ (typical laser ablation plasmas) will propagate in a straight line without being appreciably influenced by the magnetic field (Figure 36).

Schmidt's model is based on the following approach. As we know from §1.2.1, polarization limited charged particle drift (guiding centre drift) in the z-direction can be written as

$$v_z = \frac{mc}{erB}\left(v_{\|}^2 + \frac{v_{\perp}^2}{2}\right) + \frac{mc^2}{eB^2}\frac{\partial E_z}{\partial t} \tag{3.7}$$

Here we assume that magnetic fields generated by plasma currents are small compared to the guiding field and can thus be neglected, *i.e.* the solenoidal magnetic field is unaffected by plasma. The first term on the *r.h.s.* represents the magnetic field curvature and gradient drifts, while the second term is the polarization drift. Radial $\mathbf{E}\times\mathbf{B}$ drift is found as $v_r = -c\frac{E_z}{B}$ (if $\mathbf{B} = B\hat{\varphi}$).

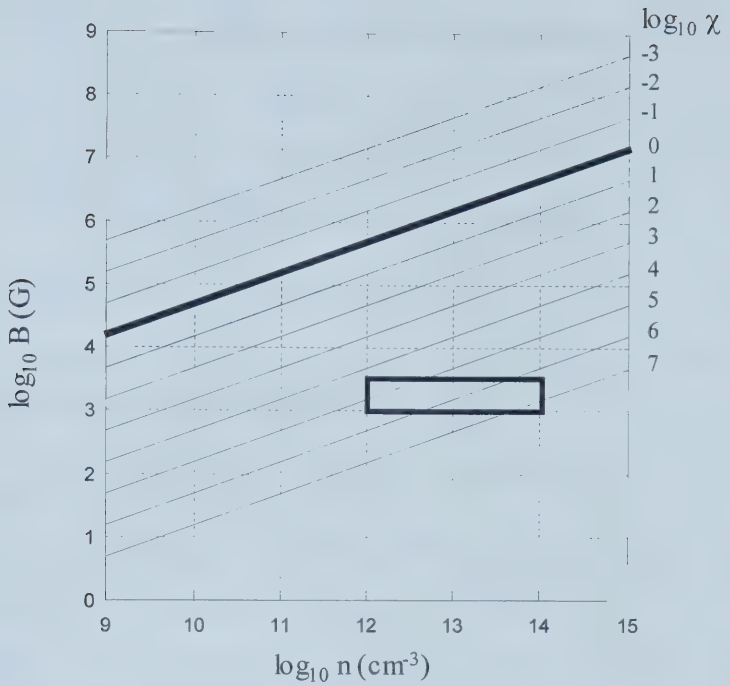

Figure 36. Dielectric susceptibility of Carbon plasma. Curved magnetic field guiding is efficient if $\chi \ll 1$ (above the thick line). Squared area represents experimental plasma parameters of interest.

Particle z-drift leads to current density in the z-direction $j_z = en\left(v_z^+ - v_z^-\right) \simeq env_z^+$, which, according to Poisson's equation, creates a growing electric field $\frac{\partial E_z}{\partial t} = -4\pi j_z = -4\pi nev_z^+$. If $\frac{\partial E_z}{\partial t}$ is substituted into equation (3.7), the latter can be solved as

$$v_z^+ = \frac{v_R + v_{\nabla B}}{1+\chi} \tag{3.8}$$

which suggests that the polarization drift reduces the curvature and gradient drifts $v_R + v_{\nabla B}$ by a factor of $1+\chi$. The electric field growth rate can be written as

$$\frac{\partial E_z}{\partial t} = -4\pi ne\frac{v_R + v_{\nabla B}}{1+\chi} \tag{3.9}$$

and the radial acceleration becomes

$$a_r \equiv \frac{\partial v_r}{\partial t} = -\frac{c}{B}\frac{\partial E_z}{\partial t} = \frac{4\pi nec}{B}\frac{v_R}{1+\chi} =$$

$$= \begin{cases} \dfrac{4\pi nec}{B}\dfrac{v_R}{\chi} = \dfrac{v_{\parallel}^2}{R}, \text{ if } \chi \gg 1 \\ \dfrac{4\pi nec}{B} v_R = \chi \dfrac{v_{\parallel}^2}{R} \ll \dfrac{v_{\parallel}^2}{R}, \text{ if } \chi \ll 1 \end{cases} \tag{3.10}$$

where we assumed $v_{\parallel} \ll v_{\perp}$. According to (3.10), when $\chi \gg 1$, particle's radial acceleration corresponds to a straight trajectory, while at $\chi \ll 1$ the radial acceleration is significantly reduced and particles follow the field lines.

3.2 Cross B-field electric current

Khizhnyak [20] points out that Shmidt's results are in a poor agreement with experimental studies that suggest that even dense plasmoids with $\chi \gg 1$ can be guided by curved magnetic fields. He introduces the idea of shorting the electrical fields arising in a curved magnetic guide, by electron currents in the straight parts of the solenoid. (In his experimental setup a magnetic guide consists of two straight sections joined by a curved section.

As we have seen in §1.2.1, an electric field applied across a magnetic field will cause particle drifts in the $\mathbf{E}\times\mathbf{B}$ direction, but it cannot lead to drifts/currents along **E** (and perpendicular to **B**), as happens in regular conductive materials. It is well known however, that collisions between particles in plasma result in random walk drift along the electric field even perpendicular to **B**. Because of that, the plasma will exhibit cross-B-field electrical conductivity which is clearly missing from the collisionless model described in §3.1. We will attempt to add the cross-B-field resistive current to Schmidt's model and derive a new plasma guiding criterion accounting for plasma conductivity.

Starting with equation (3.7) we will deviate from Schmidt's model by introducing a cross-B-field resistive current $j_z = \sigma_{\perp} E_z$ where $\sigma_{\perp}$ is the plasma perpendicular conductivity (Figure 37). This resistive current will reduce the growing electric field according to Poisson equation:

$$\frac{\partial E_z}{\partial t} = -4\pi n e v_z^+ - \sigma_{\perp} E_z \tag{3.11}$$

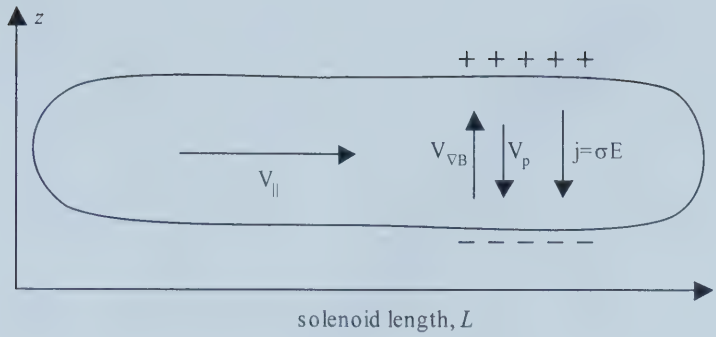

Figure 37. Shorting of curvature drifts $v_{\nabla B}$ with cross-B resistive currents j.

Taking v_z^+ from (3.11) and substituting it into (3.7) we obtain

$$\frac{\partial v_r}{\partial t} + \frac{4\pi\sigma_\perp}{1+\chi} v_r + \frac{\chi}{1+\chi}\frac{v_\parallel^2}{r_0} = 0 \tag{3.12}$$

where χ is the plasma dielectric susceptibility (3.6) and r_0 is the radius of the solenoid. We have used $v_\parallel^2 \gg v_\perp^2$ which is a valid assumption for laser ablation plasma. Equation (3.12) can be solved as

$$v_r = \frac{\chi}{4\pi\sigma_\perp}\frac{v_\parallel^2}{r_0}\left(1 - \exp\left(-\frac{4\pi\sigma_\perp}{1+\chi}t\right)\right) \tag{3.13}$$

We can integrate (3.13) over the particle time of flight to obtain the plasma radial offset from the axis of the solenoid at the exit of the solenoid (where time of flight is $t_0 \equiv L/v_\parallel$ with L being the length of the solenoid):

$$\Delta r = \frac{\chi v_\parallel^2}{4\pi\sigma_\perp r_0}\left[t_0 + \frac{1+\chi}{4\pi\sigma_\perp}\left(\exp\left(-\frac{4\pi\sigma_\perp}{1+\chi}t_0 - 1\right)\right)\right] \tag{3.14}$$

If we plot Δr as a function of its dielectric susceptibility χ and cross-B-field conductivity $\sigma_\perp$ (Figure 38), we will immediately recognize that the presence of cross-B-field conductivity allows for plasma guiding even at $\chi \gg 1$, considerably altering Schmidt's guiding criterion.

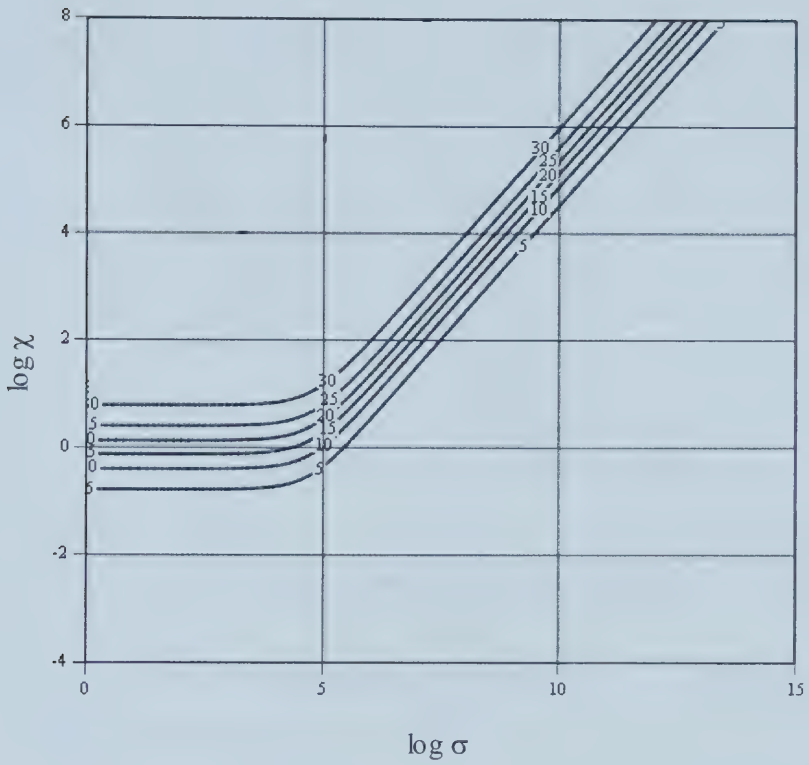

Figure 38. Dependence of plasma offset (cm) on χ and σ (sec^{-1}). Values of $L = r_0 = 70$ cm and $v_{||} = 7 \cdot 10^6$ cm/sec were used.

According to the plot on Figure 38, for plasmas corresponding to the experimental conditions with $\chi \sim 10^5$ - 10^7, and time of flight ~ 10 μsec, one would need $\sigma_\perp$ to be at least on the order of 10^{11} - 10^{13} sec^{-1} for successful guiding.

Expression (3.14) can be simplified if we consider only the plasmas with $\chi \gg 1$ (which is typical for the laser ablation plasma) and introduce $\gamma \equiv \frac{4\pi\sigma_\perp}{\chi}$:

$$\frac{\Delta r}{L} = \frac{1}{\gamma t_0}\left[1 + \frac{1}{\gamma t_0}\left(\exp(\gamma t_0) - 1\right)\right] \qquad (3.15)$$

where for simplicity we assumed $L \simeq r_0$ (typical experimental solenoid). Evidently, plasma guiding capability depends on a single parameter γt_0. As can be seen from Figure 39, for $\gamma t_0 < 1$ plasma exhibits no guiding (offset $\Delta r \simeq L/2$), approaching straight trajectory tangential to magnetic field lines.

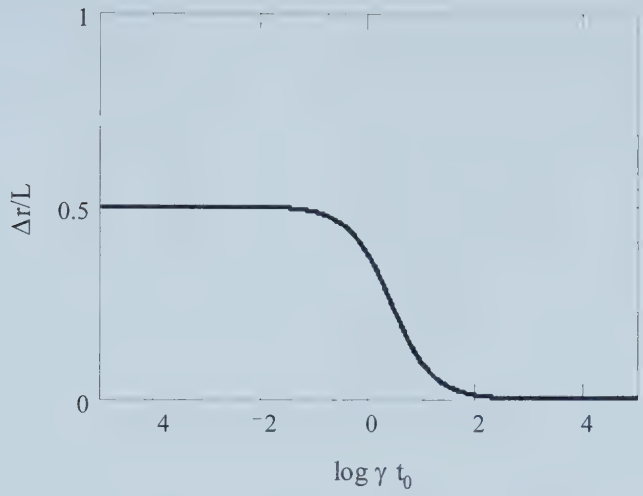

Figure 39. Dependence of plasma deviation from the solenoid axis *vs* guiding parameter γt_0.

At the same time, plasma offset approaches zero when $\gamma t_0 \gg 1$. Therefore, we can now reformulate the guiding criterion for $\chi \gg 1$ plasmas as

$$\frac{\chi}{4\pi\sigma_\perp} \ll t_0 \tag{3.16}$$

This suggests that guiding is improved if the time of flight is long (slow plasma flow or large L and r_0), when the dielectric susceptibility is low (tenuous plasma), and when the cross-field conductivity is high. Plasma cross-field conductivity appears as a result of electron and ion scattering on neutral particles and collisions between electron and ions. Cross-section of scattering on neutral particles (~ 10^{-20} m^2) is by few orders of magnitude smaller than the Coulomb collisions cross-section (~ 10^{-15} m^2 at 1 eV). Thus, Coulomb collisions will dominate over collisions with neutral in any plasma that is just a few percent ionized. At electron temperatures over 1 eV the plasma can be considered almost fully ionized.

If an electric field is applied to a plasma together with magnetic field, it will cause a current [55]:

$$\mathbf{j} = \sigma_\perp \mathbf{E} + \left(\sigma_\parallel - \sigma_\perp\right)\left(\mathbf{b}\cdot\mathbf{E}\right)\mathbf{b} + \sigma_H \mathbf{b}\times\mathbf{E} \tag{3.17}$$

where **b** is a unity vector in the direction of **B**, and the parallel ($\sigma_{\parallel}$), perpendicular Pedersen ($\sigma_{\perp}$), and Hall (σ_H) components of the conductivity tensor are given by:

$$\sigma_{\parallel} = \sigma \tag{3.18}$$

$$\sigma_{\perp} = \frac{\sigma}{1+\left(\omega_{ce}\tau_{ei}\right)^2} \tag{3.19}$$

$$\sigma_H = \frac{\sigma\left(\omega_{ce}\tau_{ei}\right)}{1+\left(\omega_{ce}\tau_{ei}\right)^2} \tag{3.20}$$

with $\sigma = \frac{ne^2}{\nu_{ei} m_e}$ being the *specific conductivity* of plasma in the absence of magnetic field, $\omega_{ce} = \frac{eB}{m_e c}$ - the ion cyclotron frequency, and the ion-electron collision time

$$\tau_{ei} = \nu_{ei}^{-1} = \left(\frac{Z^2 n \pi e^4 \ln\Lambda}{\sqrt{m_e}\left(kT\right)^{3/2}} \right)^{-1} \tag{3.21}$$

If the electric field is parallel to magnetic field, the current is $\mathbf{j} = \sigma\mathbf{E}$. If **E** is perpendicular to **B**, then there is Pedersen current in the direction of **E** given by $\sigma_{\perp}\mathbf{E}$, and Hall current perpendicular to both **E** and **B** given by $\sigma_H \mathbf{b}\times\mathbf{E}$.

Generally speaking, the conductivity tensor, or, equivalently, expression (3.17), relates electric current to electric field in the case of *infinite* plasma. When plasma is finite, boundary conditions become important. In our case, vertical electric field E_z will cause not only the Pedersen current j_z, but also Hall current in the r-direction (perpendicular to both **E** and **B**). The latter current will lead to a charge accumulation on the sides of the plasmoid, and thus to a radial electric field E_r. This field, in turn, will affect the vertical current j_z (which will be viewed as Hall current from the E_r perspective). Thus, the picture becomes quite complicated. Nevertheless, it is interesting to evaluate the effect of the cross-field conductivity by considering it in the form (3.19). Dependence of such conductivity on magnetic field and plasma density at $T = 5$ eV is shown on Figure 40.

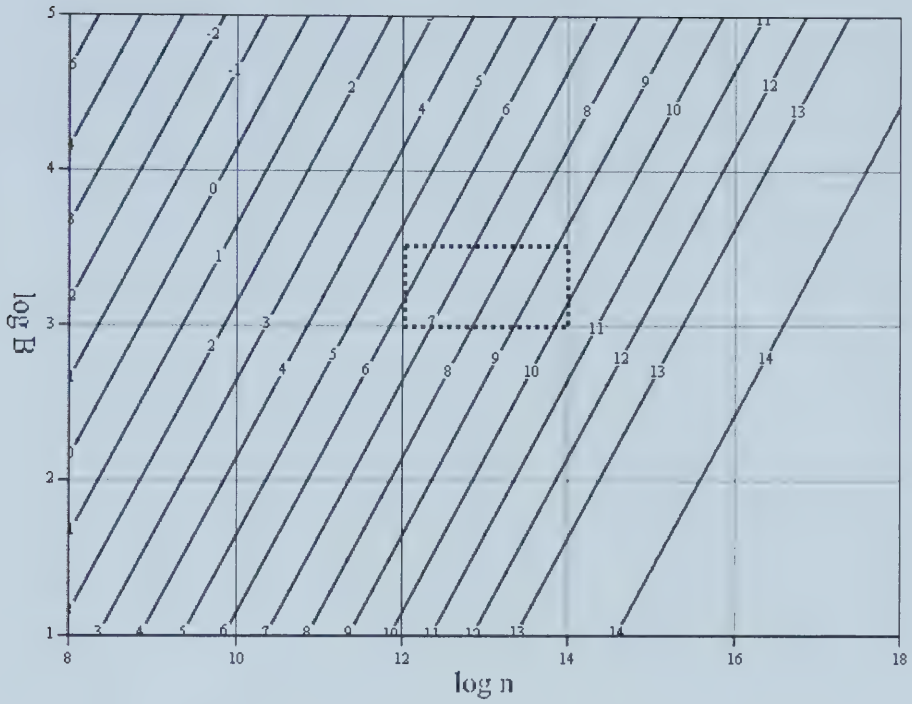

Figure 40. Log_{10} of plasma cross-field conductivity (sec^{-1}) *vs* plasma density n (in cm^{-3}) and magnetic field flux B (in Gauss). Values of $T = 5$ eV were used. Square dotted region represents experimental plasma parameters.

If the cross-field conductivity is assumed in the form (3.19), we can study the dependence of the plasma guiding parameter γt_0 on plasma density and magnetic field (Figure 41). The region of guiding ($\log(\gamma t_0) > 0$) is represented by a sharp cusp in the upper right corner of the log n - log B parametric plane. The region above the dashed line does not satisfy $\chi \gg 1$, thus making criterion (3.16) invalid there. As can be seen from Figure 41, experimental plasma parameters are outside the region of guiding. According to the plot, increase in magnetic field should not affect plasma guiding at the experimental densities. Interestingly, plasmas with higher densities would have higher chance of successful guiding. Cross-field conductivity increases at higher densities since collision frequency ν_{ei} becomes higher and electrons have more chance of drifting across the magnetic field lines, *i.e.* they become less magnetized.

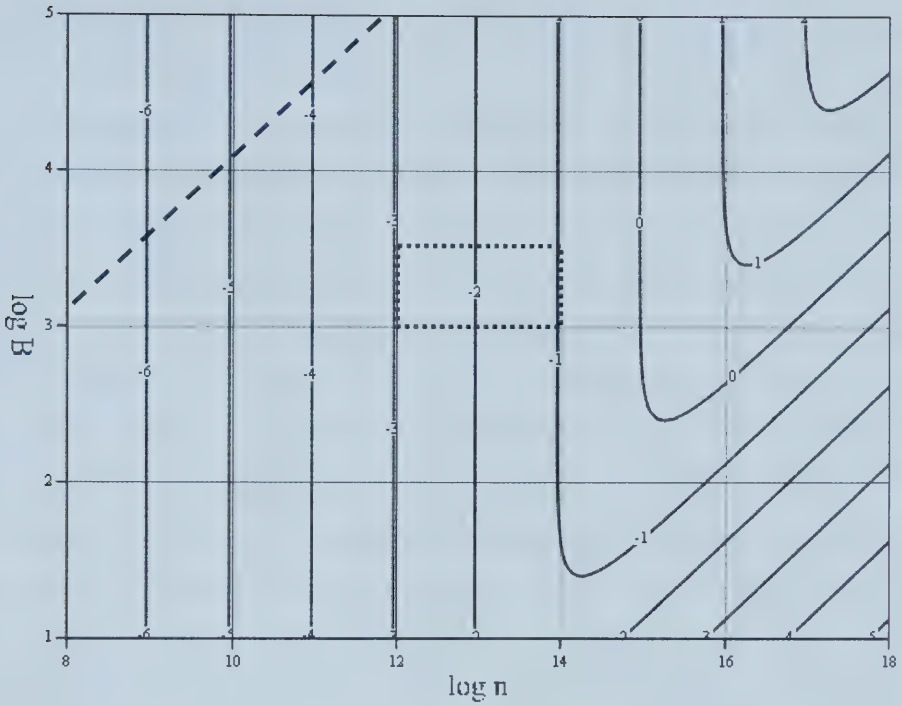

Figure 41. Log_{10} of plasma guiding parameter γt_0 *vs* plasma density n (in cm^{-3}) and magnetic field flux B (in Gauss). Values of $t_0 = 10$ μsec and $T = 5$ eV were used. Region above the dashed line corresponds to $\chi \leq 1$. Square dotted region represents experimental plasma parameters.

It is interesting to investigate the dependence of the guiding parameter γt_0 on plasma temperature. It affects the cross-field conductivity through the collision frequency ν_{ie}. As can be easily shown, cross-field conductivity (3.19), and thus the guiding parameter γt_0, is maximized at temperatures that make the electron-ion collision frequency equal to the electron cyclotron frequency $\omega_{ce} = \nu_{ei}$. At experimental plasma densities this happens at quite low temperatures, which are probably never achieved in the experiment. For example, for plasma with density 10^{13} cm^{-3} in 1 kG magnetic field, $\omega_{ce} = \nu_{ei}$ at $T = 0.062$ eV (Figure 42). From this, one can conclude that, generally, lower plasma temperatures can be favourable for guiding. However, as it follows from (3.21), during *adiabatic* expansion and cooling, i.e. when temperature and density change as $T = An^{2/3}$ (assuming that plasma can be described as a monatomic gas), the electron-ion collision time and thus the guiding parameter remain constant. This suggests that at least

within the frame of the current description, cooling of plasma during adiabatic expansion should not change the guiding efficiency.

The fact, that experimental plasma parameters are outside the guiding region (Figure 41) does not mean that the effect of cross-field conductivity cannot explain experimentally observed guiding improvement at 3 kG magnetic field. Since the plasmoid forms from a plasma plume expanding from the surface of the target, there will be, in fact, a distribution of longitudinal velocities between plasmoid particles, ranging from almost zero to ~ 10^7 cm sec. Thus, the head of the plasmoid will consist of faster particles, and its tail will be composed of slower species. Therefore, particles time of flight will vary along the plasmoid. Thus, the guiding parameter γt_0 will have values more favorable for guiding at the tail of the plasmoid. Of course, this description is oversimplified. For example, consider the fact that the charge built on the faster leading end of the plasmoid can be quickly redistributed along the field lines towards the tail end of the plasmoid. Also, even though we consider *singly* ionized plasma, in reality there is a distribution of ionization states. Cross-section of electron-ion scattering is proportional to the square of ion charge. Therefore, presence of ions with higher ionization states in the plasmoid can substantially increase cross-field conductivity and improve the guiding. In fact, even more interesting physics may occur, because ions with higher ionization states (and higher charge to mass ratio) will experience higher guiding efficiency, leading to spatial separation of differently charged ion species.

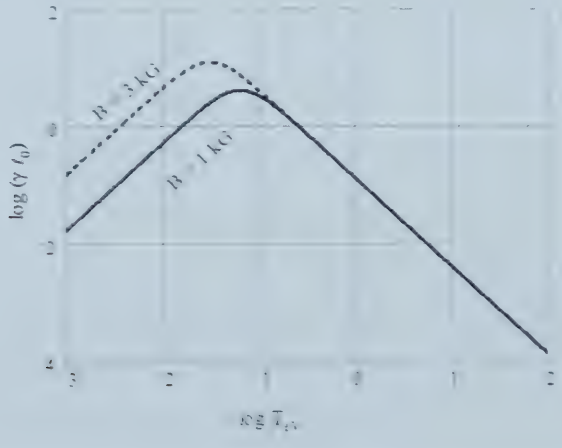

Figure 42. Dependence of guiding parameter on plasma temperature ($n = 10^{13}$ cm^{-3}, $B = 1$ kG, 3 kG).

The plasma offset (3.14) can also be plotted as a function of n and B if we assume $\sigma_\perp$ in the form of (3.19) (Figure 43). One can recognize both the Schmidt's guiding region with $\chi \ll 1$ (upper left corner), and the region of guiding where $\gamma t_0 \gg 1$ (upper right corner).

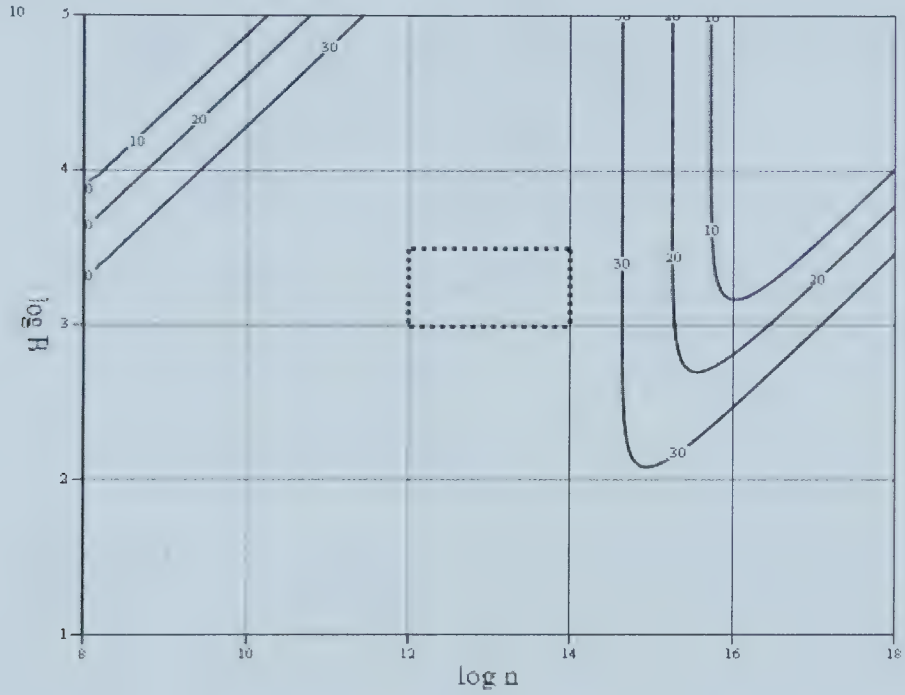

Figure 43. Plasma offset (cm) at the exit of the solenoid *vs* plasma density n (in cm^{-3}) and magnetic field flux B (in Gauss). Values of $t_0 = 10$ μsec and $T = 5$ eV were used. Square dotted region represents experimental plasma parameters.

Schematically, plasma offset (3.14) can be represented on a '$\log n - \log B$' parametric plane as shown on Figure 44. Line $C_1 - C_2 - C_4 - C_5$, satisfying $\gamma t_0 = 1$, represents the borderline between the regions of guiding ("+") and non-guiding ("-"). The region of guiding above $C_1 - C_2 - C_3$ corresponds to tenuous plasmas with $\chi \ll 1$ (single-particle like behaviour). This is the region of guiding predicted by Schmidt's model. Space charge build-up in such plasma results in very small electric field, which does not lead to any noticeable $E \times B$ plasma offset. Cross-field conductivity has no effect on plasma guiding this region.

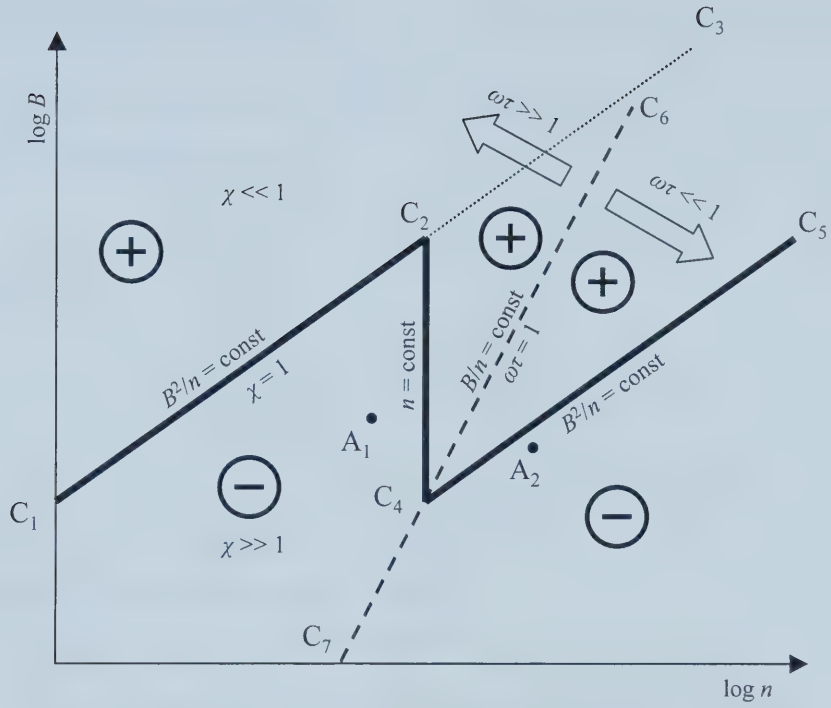

Figure 44. Schematic representation of plasma guiding region in *n*-*B* parametric plane. $C_1 - C_2 - C_4 - C_5$ satisfies $\gamma t_0 = 1$ and separates the regions of guiding ("+") and non-guiding ("-").

In contrast, guiding in regions representing dense plasmas with $\chi \gg 1$ (below $C_1 - C_2 - C_3$) is fully dependent on cross-field conductivity. On the line C_6 - C_7, electron-ion collision frequency and electron cyclotron frequency are equal, *i.e.* $\omega_{ce} = \nu_{ei}$, or $\omega_{ce}\tau_{ei} = 1$. To the left from it, where $\omega_{ce}\tau_{ei} \gg 1$, the plasma is strongly magnetized, and the cross-field conductivity becomes significantly reduced, since the mean free path is proportional to the Larmor radius and collisions are rare. Guiding capability has only a small dependence on magnetic field there (region enclosed by $C_2 - C_4 - C_6$) and improves with increasing plasma density *n*. The weak dependence on magnetic field can be explained as following. If one increases the *B*-field, the curvature currents and space charge build-up are reduced, since plasma dielectric susceptibility varies as $\chi \sim n/B^2$. At the same time, plasma cross-field conductivity decreases as $\sigma_\perp \sim n^2/B^2$ (provided $\omega_{ce}\tau_{ei} \gg 1$). Combined, both effects cancel the magnetic field dependence as

$\gamma \sim \sigma_\perp / \gamma \sim n$. The critical density (line $C_2 - C_4$) at which cross-field conductivity becomes important can be found from the requirements $\gamma t_0 = 1$ and $\omega_{ce}\tau_{ei} \gg 1$, which results in the following condition:

$$t_0 = \tau_{ei}\frac{m_i}{m_e} \equiv \tau_{ie} \tag{3.22}$$

which occurs at

$$n = \frac{m_i (kT)^{3/2}}{\sqrt{m_e}\pi e^2 \ln\Lambda} t_0^{-1} = 8\cdot 10^8 \frac{T_{eV}^{\frac{3}{2}}}{t_{0\sec}} \mathrm{cm}^{-3} = 9\cdot 10^{14}\,\mathrm{cm}^{-3} \tag{3.23}$$

for experimental parameters ($T = 5$ eV, $t_0 = 10$ μsec). Condition (3.22) suggests that the effect of cross-field conductivity becomes important when the *ion-electron* collision time becomes shorter than the particle time of flight.

Cross-field conductivity of unmagnetized plasma with $\omega_{ce}\tau_{ei} \ll 1$ (to the right from $C_6 - C_7$) is independent on n and B and is equal to Spitzer conductivity:

$$\sigma_\perp\left(\omega_{ce}\tau_{ei} \ll 1\right) = \frac{e^2}{m_e}\tau_{ei} n = \frac{(kT)^{3/2}}{\pi\sqrt{m_e}\ln\Lambda} \tag{3.24}$$

However, as one goes to regions of higher density and/or lower magnetic field (below C_4 - C_5), the effect of charge separation becomes so strong that is cannot be sufficiently compensated by the cross-field currents, and the residual electric field remains strong enough to produce substantial $E \times B$ drift.

It is interesting to calculate the difference between the magnetic field magnitude required for guiding as predicted by Schmidt's model (field along $C_1 - C_2 - C_3$) and the minimal guiding field in the presence of cross-field conductivity (field along $C_4 - C_5$). The Schmidt's guiding field is found from $\chi = 1$ condition as $B^2_{\chi=1} = 4\pi c^2 m_i n$, while the latter field satisfying $\gamma t_0 = 1$ and $\omega_{ie}\tau_{ie} \ll 1$ is found as $B^2_{\gamma t=1} = \frac{c^2 m_i m_e}{t_0 \tau_{ei} e^2}$. The ratio of the two is:

$$\frac{B_{\chi=1}}{B_{\gamma t=1}} = \sqrt{4\pi\sigma_{Sp} t_0} = \left(\frac{4(kT)^{3/2} t_0}{\sqrt{m_e}\ln\Lambda e^2}\right)^{1/2} = 10^7 \cdot T_{eV}^{\frac{3}{4}} \cdot t_{0\sec}^{\frac{1}{2}} \simeq 10^5 \tag{3.25}$$

for experimental parameters ($T = 5$ eV, $t_0 = 10\,\mu$sec). Therefore, the introduction of the cross-field conductivity alters Schmidt's guiding criterion for plasmas with density higher than (3.23) reducing the magnetic field required for guiding by a factor (3.25).

As can be seen from the above analysis, the efficiency of guiding experimental plasmas increases within the $C_3 - C_2 - C_4 - C_5$ region, and reaches its maximum when $\omega_{ce}\tau_{ei} = 1$. Thus, the experimental conditions should be optimized accordingly. However, even within the framework of the proposed model it is not easy. In particular, accurate knowledge of plasma temperature and density is required to achieve optimal experimental parameters when $\omega_{ce}\tau_{ei}$ approaches unity. For example, if experimental plasma n and B correspond to point A_1 (Figure 44), increasing the magnetic field will not improve the guiding significantly. Instead, increasing plasma density will produce the desired effect. Opposite to that, if plasma parameters correspond to point A_2, the plasma density needs to be reduced. Increasing the magnetic field would also be desirable in this case.

4. Conclusions

The phenomenon of plasma guiding in curved magnetic fields was studied in the context of magnetic filtering of laser ablation plasmas. Two approaches were taken: magnetohydrodynamical (MHD) and guiding centre drift models.

To analyse the time-dependent one-fluid resistive magnetohydrodynamical model, a 3D curvilinear transient computer code was developed based on an existing Cartesian version initially designed for the Earth's magnetosphere research. To address the specifics of laser produced plasmas, special treatment for low-density vacuum-like regions and non-reflecting boundary conditions were introduced.

To properly represent the experimental conditions of plasma expanding into vacuum in a model that requires continuous non-zero plasma density, the vacuum was modeled as a very low density plasma background ($\sim 10^{-2}$ of the plasma peak density). It is known, however, that high Alfven velocities appearing in low-density vacuum-like plasma regions severely reduce computational timestep. To resolve this limitation, we introduced an artificial attenuation of Lorentz force in the momentum equation in the low-density region, which allowed us to limit the corresponding Alfven velocities.

Transparent boundary conditions most naturally describe the experimental conditions, where plasma is allowed to escape through the coils of the magnetic solenoid. In addition, they allow to eliminate unwanted plasma disturbances reflected back from the boundaries. Both techniques have shown to be effective and robust.

Numerical results suggest that a plasma cloud with parameters corresponding to the typical experimental values (singly-charged 5 eV Carbon plasma with 10^{12} cm^{-3} density streaming with $7 \cdot 10^6$ cm/sec along a 1 kG magnetic field with radius curvature of 75 cm) shows virtually no sign of guiding. After ~3.5 μsec the plasmoid propagating in a straight trajectory hits the outer wall of the solenoid. The $\mathbf{E} \times \mathbf{B}$ drift pushing the plasma in the outward direction was identified as the dominant mechanism for poor magnetic guiding efficiency. Ions and electrons streaming along the magnetic field tend to separate causing an electric field in the direction perpendicular to the magnetic field and its radius of curvature.

To achieve a better understanding of plasma guiding mechanism, a guiding centre drift model accounting for particle collective effects through self-consistent electric field was introduced and studied both numerically (solving for particle trajectories) and analytically. Similar to the MHD model, it predicts that plasmas with densities higher than 10^6 cm^{-3} will exhibit very poor guiding in magnetic fields of 1 kG, propagating in essentially a straight trajectory. According to this model, for successful guiding, plasma dielectric susceptibility $\chi \equiv 4\pi c^2 Mn/B^2$ has to be less than unity. To achieve that in Carbon plasmas of 10^{12} - 10^{14} cm^{-3} density, the required magnetic field has to be in the $10^6 - 10^7$ gauss range. However, the experiments on laser plasma guiding suggest that guiding efficiency substantially increases when the magnetic field reaches only 3 kG of magnitude.

To address the discrepancy between the existing model and the experimental results, we introduced a cross-B-field resistive current into the guiding centre model. If the cross-field conductivity were high enough, this current would be able to close the space charge accumulation resulting from the particles' curvature/gradient drifts and thus reduce the $\mathbf{E} \times \mathbf{B}$ drift.

From the modified guiding centre drift model, we obtained a new guiding criterion $\frac{\chi}{4\pi\sigma_\perp} \ll t_0$ for dense plasmas with $\chi \gg 1$, where t_0 is the plasma time of flight. According to this criterion, experimental plasmas ($\chi \sim 10^5$ - 10^7) will experience guiding if the cross-field conductivity reaches 10^{11} - 10^{13} sec^{-1} values. For further analysis, the cross-field conductivity was considered as being caused by electron-ion elastic (Coulomb) collisions. It was shown, that the effect of the cross-field conductivity on magnetic guiding becomes significant in dense plasmas (such that ion-electron collision time is shorter than the plasma time of flight). For such plasmas, magnetic field required for guiding is by several orders of magnitude (10^5 for experimental conditions) smaller than the guiding field without the effect of cross-field conductivity.

We realize that the mechanism of plasma guiding could be significantly more complicated and other important factors could be involved. However, we have demonstrated that the effect of cross-field conductivity can be important and under certain conditions can explain the phenomenon of plasma guiding in moderate magnetic

fields. The analysis of the dependence of guiding efficiency on such parameters as plasma density, temperature and magnetic field magnitude can provide a valuable tool in optimizing the experimental conditions.

Appendix: MHD equations in component form.

An orthogonal curvilinear system of coordinates (x_1, x_2, x_3) can be specified through a set of metric coefficient (h_1, h_2, h_3). Metric coefficients are, in general, functions of the position (x_1, x_2, x_3), *i.e.* $h_1 = h_1(x_1, x_2, x_3)$, $h_2 = h_2(x_1, x_2, x_3)$, $h_3 = h_3(x_1, x_2, x_3)$. For example, for cylindrical (ρ, φ, z) coordinates they are $(h_1, h_2, h_3) = (1, \rho, 1)$, and for spherical (r, θ, φ) they become $(h_1, h_2, h_3) = (1, r, r\sin\theta)$. To expand the MHD equations (2.38) - (2.41) in component form in generalized orthogonal coordinates requires expanding spatial differential operators (*grad*, *div*, and *curl*) through (h_1, h_2, h_3) [49] with consequent algebraic manipulations. The derivations are rather cumbersome, thus a symbolic algebra software package is helpful.

$$\frac{\partial B_1}{\partial t} - \frac{1}{h_2 h_3}\frac{\partial}{\partial x_2}\left(h_3\left(v_1 B_2 - v_2 B_1\right) - \frac{\eta}{S}\frac{h_3}{h_1 h_2}\left(\frac{\partial}{\partial x_1}h_2 B_2 - \frac{\partial}{\partial x_2}h_1 B_1\right)\right) + \\ + \frac{1}{h_2 h_3}\frac{\partial}{\partial x_3}\left(h_2\left(v_3 B_1 - v_1 B_3\right) - \frac{\eta}{S}\frac{h_2}{h_1 h_3}\left(\frac{\partial}{\partial x_3}h_1 B_1 - \frac{\partial}{\partial x_1}h_3 B_3\right)\right) = 0 \qquad \text{(A.1)}$$

$$\frac{\partial B_2}{\partial t} - \frac{1}{h_1 h_3}\frac{\partial}{\partial x_3}\left(h_1\left(v_2 B_3 - v_3 B_2\right) - \frac{\eta}{S}\frac{h_1}{h_2 h_3}\left(\frac{\partial}{\partial x_2}h_3 B_3 - \frac{\partial}{\partial x_3}h_2 B_2\right)\right) + \\ + \frac{1}{h_1 h_3}\frac{\partial}{\partial x_1}\left(h_3\left(v_1 B_2 - v_2 B_1\right) - \frac{\eta}{S}\frac{h_3}{h_1 h_2}\left(\frac{\partial}{\partial x_1}h_2 B_2 - \frac{\partial}{\partial x_2}h_1 B_1\right)\right) = 0 \qquad \text{(A.2)}$$

$$\frac{\partial B_3}{\partial t} - \frac{1}{h_1 h_2}\frac{\partial}{\partial x_1}\left(h_2\left(v_3 B_1 - v_1 B_3\right) - \frac{\eta}{S}\frac{h_2}{h_1 h_3}\left(\frac{\partial}{\partial x_3}h_1 B_1 - \frac{\partial}{\partial x_1}h_3 B_3\right)\right) + \\ + \frac{1}{h_1 h_2}\frac{\partial}{\partial x_2}\left(h_1\left(v_2 B_3 - v_3 B_2\right) - \frac{\eta}{S}\frac{h_1}{h_2 h_3}\left(\frac{\partial}{\partial x_2}h_3 B_3 - \frac{\partial}{\partial x_3}h_2 B_2\right)\right) = 0 \qquad \text{(A.3)}$$

$$\frac{\partial}{\partial t}\rho v_1 + \frac{\frac{\partial}{\partial x_1}h_2h_3\rho v_1^2 + \frac{\partial}{\partial x_2}h_3h_1\rho v_1v_2 + \frac{\partial}{\partial x_3}h_1h_2\rho v_1v_3}{h_1h_2h_3} +$$
$$+\frac{\rho v_3\left(v_1\frac{\partial h_1}{\partial x_3} - v_3\frac{\partial h_3}{\partial x_1}\right)}{h_1h_3} + \frac{\rho v_2\left(v_1\frac{\partial h_1}{\partial x_2} - v_2\frac{\partial h_2}{\partial x_1}\right)}{h_1h_2} + \frac{1}{2h_1}\frac{\partial P}{\partial x_1} + \tag{A.4}$$
$$+\frac{\xi(\rho)B_2\left(\frac{\partial h_2B_2}{\partial x_1} - \frac{\partial h_1B_1}{\partial x_2}\right)}{h_1h_2} + \frac{\xi(\rho)B_3\left(\frac{\partial h_3B_3}{\partial x_1} - \frac{\partial h_1B_1}{\partial x_3}\right)}{h_1h_3} = 0$$

$$\frac{\partial}{\partial t}\rho v_2 + \frac{\frac{\partial}{\partial x_1}h_2h_3\rho v_1v_2 + \frac{\partial}{\partial x_2}h_3h_1\rho v_2^2 + \frac{\partial}{\partial x_3}h_1h_2\rho v_2v_3}{h_1h_2h_3} +$$
$$+\frac{\rho v_1\left(v_2\frac{\partial h_2}{\partial x_1} - v_1\frac{\partial h_1}{\partial x_2}\right)}{h_1h_3} + \frac{\rho v_3\left(v_2\frac{\partial h_2}{\partial x_3} - v_3\frac{\partial h_3}{\partial x_2}\right)}{h_2h_3} + \frac{1}{2h_2}\frac{\partial P}{\partial x_2} + \tag{A.5}$$
$$+\frac{\xi(\rho)B_3\left(\frac{\partial h_3B_3}{\partial x_2} - \frac{\partial h_2B_2}{\partial x_3}\right)}{h_2h_3} + \frac{\xi(\rho)B_1\left(\frac{\partial h_1B_1}{\partial x_2} - \frac{\partial h_2B_2}{\partial x_1}\right)}{h_1h_2} = 0$$

$$\frac{\partial}{\partial t}\rho v_3 + \frac{\frac{\partial}{\partial x_1}h_2h_3\rho v_1v_3 + \frac{\partial}{\partial x_2}h_3h_1\rho v_2v_3 + \frac{\partial}{\partial x_3}h_1h_2\rho v_3^2}{h_1h_2h_3} +$$
$$+\frac{\rho v_2\left(v_3\frac{\partial h_3}{\partial x_2} - v_2\frac{\partial h_2}{\partial x_3}\right)}{h_2h_3} + \frac{\rho v_1\left(v_3\frac{\partial h_3}{\partial x_1} - v_1\frac{\partial h_1}{\partial x_3}\right)}{h_2h_3} + \frac{1}{2h_3}\frac{\partial P}{\partial x_3} + \tag{A.6}$$
$$+\frac{\xi(\rho)B_1\left(\frac{\partial h_1B_1}{\partial x_3} - \frac{\partial h_3B_3}{\partial x_3}\right)}{h_1h_3} + \frac{\xi(\rho)B_2\left(\frac{\partial h_2B_2}{\partial x_3} - \frac{\partial h_3B_3}{\partial x_3}\right)}{h_2h_3} = 0$$

$$\frac{\partial\rho}{\partial t} + \frac{\frac{\partial}{\partial x_1}\rho v_1h_2h_3 + \frac{\partial}{\partial x_2}\rho v_2h_3h_1 + \frac{\partial}{\partial x_3}\rho v_3h_1h_2}{h_1h_2h_3} = 0 \tag{A.7}$$

$$\frac{\partial P}{\partial t}+\gamma\frac{\frac{\partial}{\partial x_1}Pv_1h_2h_3+\frac{\partial}{\partial x_2}Pv_2h_3h_1+\frac{\partial}{\partial x_3}Pv_3h_1h_2}{h_1h_2h_3}-(\gamma-1)\left(\frac{v_1}{h_1}\frac{\partial P}{\partial x_1}+\frac{v_2}{h_2}\frac{\partial P}{\partial x_2}+\frac{v_3}{h_3}\frac{\partial P}{\partial x_3}\right)+$$

$$+2\frac{\eta}{S}\left(\left(\frac{\frac{\partial h_3B_3}{\partial x_2}-\frac{\partial h_2B_2}{\partial x_3}}{h_2h_3}\right)^2+\left(\frac{\frac{\partial h_1B_1}{\partial x_3}-\frac{\partial h_3B_3}{\partial x_1}}{h_1h_3}\right)^2+\left(\frac{\frac{\partial h_2B_2}{\partial x_1}-\frac{\partial h_1B_1}{\partial x_2}}{h_1h_2}\right)^2\right)=0 \qquad \text{(A.8)}$$

Numerical diffusion terms with diffusion coefficient D added to these equations (except those for the B-field) have the following components:

$$\frac{\partial}{\partial t}\rho v_1\ldots-\frac{\frac{\partial}{\partial x_1}\left(D\frac{h_2h_3}{h_1}\frac{\partial\rho v_1}{\partial x_1}\right)+\frac{\partial}{\partial x_2}\left(D\frac{h_3h_1}{h_2}\frac{\partial\rho v_1}{\partial x_2}\right)+\frac{\partial}{\partial x_3}\left(D\frac{h_1h_2}{h_3}\frac{\partial\rho v_1}{\partial x_3}\right)}{h_1h_2h_3}=0 \qquad \text{(A.9)}$$

$$\frac{\partial}{\partial t}\rho v_2\ldots-\frac{\frac{\partial}{\partial x_1}\left(D\frac{h_2h_3}{h_1}\frac{\partial\rho v_2}{\partial x_1}\right)+\frac{\partial}{\partial x_2}\left(D\frac{h_3h_1}{h_2}\frac{\partial\rho v_2}{\partial x_2}\right)+\frac{\partial}{\partial x_3}\left(D\frac{h_1h_2}{h_3}\frac{\partial\rho v_2}{\partial x_3}\right)}{h_1h_2h_3}=0 \qquad \text{(A.10)}$$

$$\frac{\partial}{\partial t}\rho v_3\ldots-\frac{\frac{\partial}{\partial x_1}\left(D\frac{h_2h_3}{h_1}\frac{\partial\rho v_3}{\partial x_1}\right)+\frac{\partial}{\partial x_2}\left(D\frac{h_3h_1}{h_2}\frac{\partial\rho v_3}{\partial x_2}\right)+\frac{\partial}{\partial x_3}\left(D\frac{h_1h_2}{h_3}\frac{\partial\rho v_3}{\partial x_3}\right)}{h_1h_2h_3}=0 \qquad \text{(A.11)}$$

$$\frac{\partial}{\partial t}\rho\ldots-\frac{\frac{\partial}{\partial x_1}\left(D\frac{h_2h_3}{h_1}\frac{\partial\rho}{\partial x_1}\right)+\frac{\partial}{\partial x_2}\left(D\frac{h_3h_1}{h_2}\frac{\partial\rho}{\partial x_2}\right)+\frac{\partial}{\partial x_3}\left(D\frac{h_1h_2}{h_3}\frac{\partial\rho}{\partial x_3}\right)}{h_1h_2h_3}=0 \qquad \text{(A.12)}$$

$$\frac{\partial}{\partial t}P\ldots-\frac{\frac{\partial}{\partial x_1}\left(D\frac{h_2h_3}{h_1}\frac{\partial P}{\partial x_1}\right)+\frac{\partial}{\partial x_2}\left(D\frac{h_3h_1}{h_2}\frac{\partial P}{\partial x_2}\right)+\frac{\partial}{\partial x_3}\left(D\frac{h_1h_2}{h_3}\frac{\partial P}{\partial x_3}\right)}{h_1h_2h_3}=0 \qquad \text{(A.13)}$$

The above equations can be rearranged in such a way as to collect the terms with leading derivatives $\partial/\partial x_1$, $\partial/\partial x_2$ and $\partial/\partial x_3$ into terms **F**, **G** and **H** respectively:

$$F_1 = 0 \tag{A.14}$$

$$F_2 = \frac{1}{h_1 h_3}\frac{\partial}{\partial x_1}\left(h_3\left(v_1 B_2 - v_2 B_1\right) - \frac{\eta}{S}\frac{h_3}{h_1 h_2}\left(\frac{\partial h_2 B_2}{\partial x_1} - \frac{\partial h_1 B_1}{\partial x_2}\right)\right) \tag{A.15}$$

$$F_3 = \frac{1}{h_1 h_2}\frac{\partial}{\partial x_1}\left(h_2\left(v_1 B_3 - v_3 B_1\right) - \frac{\eta}{S}\frac{h_2}{h_1 h_3}\left(\frac{\partial h_3 B_3}{\partial x_1} - \frac{\partial h_1 B_1}{\partial x_3}\right)\right) \tag{A.16}$$

$$F_4 = \frac{\frac{\partial h_2 h_3 \rho v_1^2}{\partial x_1}}{h_1 h_2 h_3} - \frac{\rho v_3^2 \frac{\partial h_3}{\partial x_1}}{h_1 h_3} - \frac{\rho v_2^2 \frac{\partial h_2}{\partial x_1}}{h_1 h_2} + \frac{\frac{\partial P}{\partial x_1}}{2h_1} + \frac{\xi(\rho) B_2 \frac{\partial h_2 B_2}{\partial x_1}}{h_1 h_2} + \\ + \frac{\xi(\rho) B_3 \frac{\partial h_3 B_3}{\partial x_1}}{h_1 h_3} - 2\frac{\frac{\partial}{\partial x_1}\left(D \frac{h_2 h_3}{h_1}\frac{\partial \rho v_1}{\partial x_1}\right)}{h_1 h_2 h_3} \tag{A.17}$$

$$F_5 = \frac{\frac{\partial h_2 h_3 \rho v_1 v_2}{\partial x_1}}{h_1 h_2 h_3} + \frac{\rho v_1 v_2 \frac{\partial h_2}{\partial x_1}}{h_1 h_2} - \frac{\xi(\rho) B_1 \frac{\partial h_2 B_2}{\partial x_1}}{h_1 h_2} - 2\frac{\frac{\partial}{\partial x_1}\left(D \frac{h_2 h_3}{h_1}\frac{\partial \rho v_2}{\partial x_1}\right)}{h_1 h_2 h_3} \tag{A.18}$$

$$F_6 = \frac{\frac{\partial h_2 h_3 \rho v_1 v_3}{\partial x_1}}{h_1 h_2 h_3} + \frac{\rho v_1 v_3 \frac{\partial h_3}{\partial x_1}}{h_1 h_2} - \frac{\xi(\rho) B_1 \frac{\partial h_3 B_3}{\partial x_1}}{h_1 h_2} - 2\frac{\frac{\partial}{\partial x_1}\left(D \frac{h_2 h_3}{h_1}\frac{\partial \rho v_3}{\partial x_1}\right)}{h_1 h_2 h_3} \tag{A.19}$$

$$F_7 = \frac{\frac{\partial h_2 h_3 \rho v_1}{\partial x_1}}{h_1 h_2 h_3} - 2\frac{\frac{\partial}{\partial x_1}\left(D \frac{h_2 h_3}{h_1}\frac{\partial \rho}{\partial x_1}\right)}{h_1 h_2 h_3} \tag{A.20}$$

$$F_8 = \frac{\gamma \frac{\partial h_2 h_3 P v_1}{\partial x_1}}{h_1 h_2 h_3} -$$

$$-(\gamma - 1)\left[\frac{v_1 \frac{\partial P}{\partial x_1}}{h_1} + \frac{2\eta}{S}\left(\frac{\left(\frac{\partial h_3 B_3}{\partial x_1}\right)^2}{h_1^2 h_3^2} + \frac{\left(\frac{\partial h_2 B_2}{\partial x_1}\right)^2}{h_1^2 h_2^2} - \frac{\frac{\partial h_1 B_1}{\partial x_3}\frac{\partial h_3 B_3}{\partial x_1}}{h_1^2 h_3^2} - \frac{\frac{\partial h_1 B_1}{\partial x_2}\frac{\partial h_2 B_2}{\partial x_1}}{h_1^2 h_2^2} \right) \right] - \qquad \text{(A.21)}$$

$$-2\frac{\frac{\partial}{\partial x_1}\left(D \frac{h_2 h_3}{h_1}\frac{\partial P}{\partial x_1} \right)}{h_1 h_2 h_3}$$

Components $G_1 \ldots G_8$ can be obtained by interchanging all '1' subscripts in $F_1 \ldots F_8$ with all '2' subscripts. Similarly, to get $H_1 \ldots H_8$ one would have to interchange subscripts '1' and '3' of $F_1 \ldots F_8$.

Bibliography

1. *Pulsed laser deposition of diamond-like carbon wear protective coatings: A review.* A. A Voevodin; M. S. Donley, J. S. Zabinski, *Surface and Coatings Technology*, vol. 92(1-2), Jun. 1997, pp. 42-49
2. *Evaluation of diamond-like carbon-coated orthopaedic implants*, D. P. Dowling, P. V. Kola, K. Donnelly, T. C. Kelly, K. Brumitt, L. Lloyd, R. Eloy, M. Therin and N. Weill, *Diamond and Related Materials*, vol. 6, 1997, pp. 390-393.
3. *Commercial applications of ion beam deposited diamond-like carbon (DLC) coatings.* F. M. Kimock, B. J. Knapp, *Surface and Coatings Technology*, vol. 56(3), 1993, pp. 273-279
4. *Laser-induced plasmas for primary ion deposition of epitaxial Ge and Si films*, D. Lubben, S. A. Barnett, K. Suzuki, S. Gorbatkin, and J. E. Greene, *Journal of Vacuum Science & Technology B: Microelectronics and Nanometer Structures,* vol. 3, July 1985, pp. 968-974.
5. *Handbook of Chemical Vapor Deposition (CVD)*. H. O. Pierson, 1993.
6. *Sputtering of Dielectrics by High-Frequency Fields*. G. S. Anderson, W. N. Mayer, and G. K. Wehner, *Journal of Applied Physics*, vol. 33 (10), 1962, p. 2991.
7. *Magnetron Plasma Deposition Processes*, S. M. Rossnagel, *Thin Solid Films*, vol. 171, 1989, p. 125.
8. *Thin film bonding using ion beam techniques - a review,* J. Baglin, *IBM Journal of Research and Development*, vol. 38(4), July 1994, pp. 413-422
9. *Deposition of Diamond-Like and Other Special Coatings by Pulsed Laser Ablation and Their Post-synthesis Processing*. S. B. Ogale, A. P. Malshe and S. M. Kanetkar, *Materials & Manufacturing Processes*, vol. 8 (1), 1993, pp. 19-58.
10. *On the origin of spatial nonuniformities in the composition of pulsed-laser-deposited films*, K. L. Saenger, *Journal of Applied Physics*, vol. 70, 1991, p. 5629.

11. *Experimental study of charge state distribution from KrF and ruby laser-produced plasmas*, Y. Y. Tsui, R. Fedosejevs, and A. A. Offenberger, *Physics of fluids. B, Plasma physics*, vol. 5, 1993, p. 3357.
12. *Guiding and Confinement of a Laser Produced Plasma by a Curved Magnetic Field.* Y. Y. Tsui, D. Vick and R. Fedosejevs, *Applied Physics Letters*, vol.70(15), April 14, 1997, pp. 1953-55,
13. *Debris reduction for copper and diamond-like carbon thin films produced by magnetically guided pulsed laser deposition*, Y. Y. Tsui, H. Minami, D. Vick, and R. Fedosejevs, *Journal of Vacuum Science & Technology A: Vacuum, Surfaces, and Films*, Vol. 20, No. 3, May 2002, pp. 744–747.
14. *Characterization of Diamond-like Films Produced by Pulsed Laser Deposition.* Hideki Minami, *M. Sc. Thesis*, University of Alberta, 1999.
15. *Electric discharge enhancement of laser produced plasma for thin film deposition. D. G. Redman*, J. Mouillaux, S. Zhe, Y. Y. Tsui and R. Fedosejevs, *26th IEEE International Conference on Plasma Science*, June 21-24, 1999, Monterey, California.
16. *Investigation of Magnetic Guiding of Laser Plasmas for Thin Film Deposition.* D. G. Redman, S. Roupassov, Y. Y. Tsui, R. Rankin, C. E. Capjack, R. Fedosejevs, *27th IEEE International Conference on Plasma Science*, June 4-7, New Orleans, Louisiana.
17. *Introduction to plasma physics*, F. F. Chen, Plenum, New York, 1974.
18. *Plasma Motion Across Magnetic Fields*, G. Schmidt, *The Physics of Fluid*, vol. 3, 1960, pp. 961 - 965.
19. *Transport processes in a plasma*, S. I. Braginskii, in *Reviews of Plasma Physics*, edited by M. A. Leontovich, Consultants Bureau, New York, vol.1, 1965.
20. *Motion of a plasmoid in the magnetic field of a toroidal solenoid*, N. A. Khizhnyak, *Soviet Physics - Technical Physics*, vol. 10, no. 5, November 1965, pp. 655-661.

21. *Modeling plasma flow in straight and curved solenoids*, D. B. Boercker, D. M. Sanders, J. Storer, S. Falabella, *Journal of Applied Physics,* vol. 69 (1), January 1991, pp. 115-120.
22. *Simulation of ion transport through curved-solenoid macroparticle filters*, C. A. Davis, I. J. Donnelly, *Journal of Applied Physics,* vol. 72 (5), September 1992, pp. 1740-1747.
23. *The effect of magnetic field configuration on plasma beam profiles in curved magnetic filters*, M. M. M. Bilek, *Journal of Applied Physics*, vol. 85 (9), 1 May 1999, pp. 6385-6391.
24. *ORBXYZ: a 3D Single Particle Orbit Code for Following Charged Particle Trajectories in Equilibrium Magnetic Field,* D. V. Anderson, R. H. Cohen, J. R. Ferguson, B. M. Johnston, C. B. Sharp, P. A. Willmann, *Lawrence Livermore Laboratory Report UCRL-53151*, June 30, 1981.
25. *Motion of a plasmoid in a curvilinear magnetic field*, V. S. Voitsenya, A. G. Gorbanyuk, I. N. Onishchenko, B. G. Safronov, N. A. Khizhnyak, V. V. Shkoda, *Soviet Physics - Technical Physics*, vol. 12, no. 2, August 1967, pp. 185-192.
26. *Plasma Motion in a Filtered Cathodic Vacuum Arc*, V. S. Veerasamy, G. A. J. Amaratunga, W. I. Milne, *IEEE Transactions on Plasma Science*, vol. 21, no. 3, 1992, pp. 322-328.
27. *Simulation of Plasma Flow in Toroidal Solenoid Filters*, X. Shi, Y. Q. Tu, H. S. Tan, B. K. Tay, W. I. Milne, *IEEE Transactions on Plasma Science*, vol. 24, no. 6, December 1996, pp. 1309-1318.
28. *Plasma flow simulation in an off-plane bend magnetic filter*, B. K. Tay, G. F. You, S. P. Lau, X. Shi, *Surface and Coatings Technology*, vol. 133-134, 2000, pp. 593-597.
29. *Plasma Physics via Computer Simulation*, C.K. Birdsall and A.B. Langdon, McGraw-Hill, New York, 1981.
30. *Particle-in-Cell Charged-Particle Simulations, Plus Monte Carlo Collisions with Neutral Atoms, PIC-MCC.* C.K. Birdsall, *IEEE Transactions on Plasma Science*, vol. 19(2), April 1991.

31. *Object-Oriented Parallel Computation for Plasma Simulation*. Charles D. Norton, Boleslaw K. Szymanski, Viktor K. Decyk, *CACM* 38 (10) (1995), pp. 311-318.
32. *Numerical Recipies: the Art of Scientific Computing*, W. H. Press, S. A. Teukolsky, W. T. Vetterling, B. P. Flannery (Cambridge University Press), 2nd ed., 1997.
33. *Interchange instabilities in a compressible plasma*, P. L. Pritchet, C. C. Wu, and J. M. Dawson, *Physics of fluids*, vol. 21, 1978, p.1543.
34. *The Alternating-Direction Implicit Numerical Solution of the Time-Dependent, Three-dimensional, Single Fluid, Resistive Magnetohydrodynamic Equations*. C.H. Finan III, *Ph.D. Thesis*, University of California, Davis, 1979
35. *Solution of the Time-Dependent, Three-dimensional Resistive Magnetohydrodynamic Equations*. C. H. Finan III and J. Killeen, *Computer Physics Communications*, vol. 24, 1981, pp. 441-463.
36. *Alternating Direction Implicit Methods on Distributed and Shared Memory Parallel Computers*. R. Rankin and I. Voronkov, in *High Performance Computing Systems and Applications*, Kluwer Academic Press, 1998, pp. 59 - 69.
37. *Finite Element Methods in Linear Ideal Magnetohydrodynamics*, R. Gruber, J. Rappaz, Springer-Verlag, 1985.
38. *A Boundary Conditions for Computational Magnetohydrodynamics*. I. R. Lindemuth, *Journal of Computational Physics*, vol. 25, 1977, pp. 104-17.
39. *Expansion of Laser-Produced Plumes Near the Plasma Ignition Threshold*. L. Balazs, R. Gijbels, A. Vertes, *Analytical Chemistry*, vol. 63, 1991, pp. 314-20.
40. *Modeling the Thermal-to-Plasma Transitions for Cu Photoablation*. A. Vertes, R. W. Dreyfus, D. E. Platt, *IBM Journal of Research and Development*, v.38(1), 1994, pp.3-10.
41. *Hydrodynamic Modeling of Laser Plasma Ionization Processes*, A. Vertes, P. Juhatz, M. de Wolf and R.Gijbels, *International Journal of Mass Spectrometry and Ion Processes*, vol. 94, 1989, pp. 63-85.

42. *Laser-Produced Plasma expansion in a uniform magnetic field*, U. S. Begimkulov, B. A. Bryunetkin, V. M. Dyakin, G. A. Koldashov, S. N. Priyatkin, A.Y. Repin, E. L. Stupitsky and A. Y. Faenov, *Laser and Particle Beams*, vol. 10(4), 1992, pp.723-35.

43. *Free-boundary vacuum arc plasma jet expansion in a curved magnetic field*, M. Keidar, I. I. Beilis, A. Anders, I. G. Brown, *IEEE Transactions on Plasma Science*, vol. 27, no. 2, April 1999, pp. 613-619.

44. *Multiply charged ion transport in free boundary vacuum arc plasma jet*, M. Keidar, I. I. Beilis, I. G. Brown, *Journal of Applied Physics,* vol. 84 (11), 1 December 1998, pp. 5956-5960.

45. *Plasma Kinetic Theory*, D. C. Montgomery and D. A. Tidman, McGraw-Hill, 1964.

46. *Principles of Plasma Physics*, N. A. Krall and A. W. Trivelpiece, McGraw-Hill, 1973.

47. *Plasma physics: an introduction to the theory of astrophysical, geophysical, and laboratory plasmas*, Peter A. Sturrock, Cambridge University Press, 1994.

48. *Solution of the Time-dependent, Three-dimensional Magnetohydrodynamic Equations*, C. H. Finan and J. Killeen, *Computer Physics Communications*, vol. 24, 1981, pp. 441 - 463.

49. *Methods of Theoretical Physics*, P. M. Morse and H. Feshbach, vol. 1, p. 26, McGraw-Hill, New York, 1953.

50. Maple® V5, Waterloo Maple Inc.

51. *A General Formulation of Alternating Direction Methods. Part 1. Parabolic and Hyperbolic Problems*, J. J. Douglas and J. E. Gunn, *Numerische Mathematik*, vol. 6, 1964, pp. 428-453.

52. W. C. Chew, in *Waves and fields in inhomogeneous media*, reprint, New York: Van Nostrand Reinhold, 1990, pp. 246 - 249.

53. J. Brackbill, in *Methods in Computational Physics*, vol. 16, J. Killeen (Ed.), Academic Press, New York, 1976.

54. *Introduction to Plasma Physics*, R. J. Goldston, P. H. Rutherford, Institute of Physics Publishing, Bristol and Philadelphia, 1995.

55. *Plasma Physics*, P. A. Sturrok, Cambridge University Press, 1994.

University of Alberta Library
0 1620 1773 8046
B45818